NTNU
Norwegian University of
Science and Technology

Estimating Overburden Dilation Factors Using Geomechanical Modeling, Time-Lapse Seismic and Bathymetry Data

A Case Study from The Ekofisk Field

Arnstein Kvilhaug

Abstract

As reservoir compaction is causing variations in both layer thickness and seismic velocities, it is of interest to distinguish between these two effects. The dilation factor $\mathcal{R}$ can be used to link the geophysical observables and the physical properties of the rock. The $\mathcal{R}$-factor is defined as the ratio of relative change in velocity to relative change in strain. There are still unanswered questions related to the variation of the $\mathcal{R}$-factor.

We suggest inverting for a set of reservoir parameters to obtain the relative thickness change above the reservoir, using geomechanical modeling constrained by seafloor subsidence, measured from repeated bathymetry measurements. The resulting $\mathcal{R}$-factor values will be calculated through a rock physics relation using the modeled relative thickness change and the corresponding relative time shifts provided by 4D seismic. The global inversion process has been implemented using real data from the Ekofisk Field, located in the Southern North Sea, acquired in 2011 and 2014.

The resulting $\mathcal{R}$ values will depend on the accuracy of the model parameters in which the inversion process define. It is hard to determine the underlying "real" model parameter since the geomechanical model will not reflect the complexity of the Ekofisk reservoir. The calculated $\mathcal{R}$ values will, therefore, be associated with errors. Negative overburden time shifts were recorded, representing speedup in the monitor case. Even though the study was implemented on a 2D seismic line with increasing positive time shifts with depth, it seems like the constrained displacements together with the relative time shifts do not reflect the stress paths estimated from the geomechanical model. The method still provides knowledge of the processes involved. The calculated $\mathcal{R}$ will depend on the stress path from the geomechanical model and the interaction with time shifts from seismic data, and may differ both laterally and with depth, depending on the interaction. The study illustrates the importance of collecting data where time-lapse changes are most prominent and how the calculated $\mathcal{R}$ becomes unstable for position larger than the underlying reservoir radius. The instabilities are dependent on depth, and the effect occurs at a larger position for shallow- compared to deeper layers due to stress arching. The scientific approach used in this study can potentially be utilized with more accurate geomechanical models, which account for heterogeneities and non-elastic effects in the reservoir and overburden, in order to calculate the $\mathcal{R}$-factor values more precise.

Sammendrag

Ettersom kompaksjon av et reservoar forårsaker variasjoner i både lagtykkelse og seismiske hastigheter, er det av interesse å skille mellom de to effektene. Dilasjons faktoren $\mathcal{R}$ kan brukes til å knytte de geofysiske målingene og de fysiske egenskapene til bergarten. Faktoren $\mathcal{R}$ er definert som forholdet mellom relativ endring i hastighet og relativ endring i deformasjon. Det er fortsatt spørsmål knyttet til variasjonen av $\mathcal{R}$-faktoren.

Vi foreslår å invertere for et sett med reservoar parametre for å bestemme de relative tykkelsesendringene over reservoaret ved hjelp av geomekanisk modellering, begrenset av havbunnsforskyvningen, målt fra gjentatte batymetri målinger. De resulterende $\mathcal{R}$-faktor verdiene beregnes ved hjelp av en bergartsfysisk relasjon, og tar inn de modellerte relative tykkelsesendringen og de assosierte relative tidsskiftene, målt fra 4D seismikk. Den globale inversjonsprosessen er implementert på ekte data fra Ekofisk feltet, som ligger i sørlige del av Nordsjøen, innsamlet i 2011 og 2014.

De modellerte $\mathcal{R}$ verdiene vil avhenge av nøyaktigheten av modellparameterne som inversjonsprosessen definerer. Det er vanskelig å bestemme de underliggende "ekte" modellparameterne, siden den geomekaniske modellen ikke reflekterer kompleksiteten til Ekofisk reservoaret. De beregnede $\mathcal{R}$ verdiene vil derfor være assosiert med feil. Negative tidsskift i lagene over reservoaret ble målt, som representerer fartsøkning i monitoreringsundersøkelsen. Selv om studien ble implementert på en 2D seismisk linje med økende positive tidsskift med dybde, virker det som at den begrensende havbunnsforskyvningen sammen med de relative tidsskiftene ikke reflekterer spenningsstiene estimert fra den geomekaniske modellen. Metoden gir fortsatt forståelse av prosessene involvert. Den beregnede $\mathcal{R}$, vil avhenge av spenningsstien fra den geomekaniske modellen og samspillet med tidsskiftene fra seismiske data, og kan variere både lateralt og med dyb, avhengig av interaksjonen. Studien illustrerer betydningen av å samle data der endringene er mest fremtredende og hvordan den beregnede $\mathcal{R}$-faktoren blir ustabil for posisjon større enn den underliggende reservoarradiusen. Ustabiliteten er avhengig av dybde, og effekten skjer ved større posisjon for grunne- sammenlignet med dypere lag som følge av buet spenninger. Metoden som brukes i denne studien kan potensielt bli brukt sammen med mer nøyaktige geomekaniske modeller, som tar hensyn til heterogeniteter og ikke-elastiske effekter i reservoaret og i lagene over, for å beregne $\mathcal{R}$ verdiene mer presis.

Preface

The following thesis is written as the final part of my Master's Degree in Petroleum Geosciences, specializing in Petroleum Geophysics, at the Norwegian University of Science and Technology (NTNU), submitted 11. June 2017. The thesis was written at the Department of Geoscience and Petroleum at NTNU, Trondheim under supervision of Professor Martin Landrø using data provided by ConocoPhillips.

Trondheim, 2017-06-11

Arnstein Kvilhaug

Acknowledgment

I would like to thank Professor Martin Landrø for providing the idea behind the thesis and for supervising me throughout the process. I would also like to thank Associate Professor Kenneth Duffaut and Professor Rune Martin Holt for showing an interest and answering my questions related to the thesis. Gratitude should also be given to Per Gunnar Folstad for making it possible for me to use real data provided by ConocoPhillips in my thesis, and furthermore Sirikarn Narongsirikul for answering all my questions related to the datasets. Acknowledgment should also be given to the Ekofisk Licensees; Total E&P Norge AS, ConocoPhillips Skandinavia AS, Eni Norge AS, Statoil Petroleum AS and Petoro AS for allowing me us the data.

Special thanks to my fellow students at the Department of Geoscience and Petroleum for making these five years at NTNU fly by and to my beloved family for their continuous support.

A.K

x

Contents

List of Figures

LIST OF FIGURES

List of Tables

Chapter 1

Introduction

About 60 % of the introduction is taken and revised from the Specialization project (Kvilhaug, 2016).

When petroleum reservoirs are produced, the pore pressure within the reservoir rock is reduced causing the grain contact to increase. Depending on the geomechanical properties of the reservoir rock, the increasing grain contact may eventually cause the reservoir rock to compact. The resulting permeability change will influence the production performance of the field.

This pressure depletion will not only alter the stress and strain field of the reservoir rock but will have repercussion for the overburden and the underburden. Seafloor subsidence has been observed as a product of production-related compaction. The magnitude of seafloor subsidence is usually smaller than the reservoir compaction, inferring that the overburden is stretched.

Several fields in the North Sea show examples of this production-related compaction (Doornhof et al., 2006). In the Southern part of the North Sea, fields are producing from chalk reservoirs. Chalk is a rock with a weak framework, in fields like Valhall and Ekofisk, we see severe effects of compaction and subsidence related to production. Since Ekofisk first started producing in 1971, the water bottom has subsided almost 10 m (NPD, 2017). In 1987 a jack-up operation was completed bringing the lower platform decks out of reach for the highest storm waves, which had been getting closer and closer since the subsidence was first observed in 1984. In 1987 waterflooding was initiated to increase the pore pressure and reduce the compaction of the reservoir. The reservoir

pressure increased, but the compaction continued. Laboratory measurements on chalk have later shown that high-porosity, oil-filled chalk continues to compact when flushed with seawater due to chemical effects (water weakening) (Hermansen et al., 2000).

Repeated seismic surveys can give valuable information regarding saturation changes but also the production-related changes in stress and strain fields (Bjorlykke, 2010). Time-lapse seismic (4D seismic) is a standard reservoir monitoring tool and is very beneficial for field management in well planning to locate untapped reserves. Production-related compaction may cause reactivation of faults in or around the reservoir and furthermore minor seismic tremors. Such minor seismic events have also been detected during water injection at Ekofisk (Ottemöller et al., 2005), and the use of time-lapse seismic can give a better understanding of the connection. Furthermore, monitoring the overburden can provide valuable information to counteract health, safety, and environmental (HSE) situations. The alternation of the stress and strain fields in the overburden may lead to damage on casings of existing wells. The effect is most prominent if shear stresses are introduced as a byproduct of the compaction (Røste et al., 2006), which can result in major accidents with high environmental and economic impact, in the worst case similar to BP's deepwater oil spill in 2010 (Smith et al., 2011).

Time-lapse monitoring is for these reasons of vital importance both for the reservoir and for the overburden. The challenge is to determine what is caused by thickness changes and what is caused by velocity changes when analyzing the quantitative time-lapse seismic data. From Eq. 1.1 we know that zero offset two-way traveltime ($\mathtt{TWT}$) depends on layer thickness Z, and seismic P-wave velocity V_p within the layer.

$$\mathtt{TWT} = \frac{2Z}{V_p} \tag{1.1}$$

From Eq. 1.1 it is apparent that a change in TWT, 4D time shift, will capture the combined effect of the change in layer thickness Z and velocity V_p. Work done by Landrø and Stammeijer (2004) and Hatchell and Bourne (2005) have expressed relative zero-offset time shifts in terms of relative thickness changes and relative velocity changes in Eq. 1.2. Derivation is shown in Appendix D.

$$\frac{\Delta T}{T} = \frac{\Delta Z}{Z} - \frac{\Delta V_p}{V_p} \tag{1.2}$$

2

The seismic time shifts measured for a particular event, will have traveled down and up through all the layers above the interface, and will for that reason be more of an average change. This method can be improved by rather looking at the time strains $\frac{\Delta T}{T}$, essentially dividing the subsurface into smaller packages and analyze the relative time shifts within these layers/packages. The time strains are interval properties and can be interpreted more directly than time shifts, but the differentiation tends to boost noise and hence the time strains are noisier than the time shifts (Rickett et al., 2007).

Compaction of a rock layer results in negative $\frac{\Delta Z}{Z}$ term but an increase in velocity, positive $\frac{\Delta V_p}{V_p}$. While stretching a rock layer cause a decrease in velocity, negative $\frac{\Delta V_p}{V_p}$ and positive $\frac{\Delta Z}{Z}$. The expression from Eq. 1.2 is derived assuming $|\frac{\Delta Z}{Z}| << 1$ and $|\frac{\Delta V_p}{V_p}| << 1$. The magnitude or the effect of the two terms has been studied and proven not to be equal. Time-lapse seismic data from many locations around the world indicate that a simple linear model relating relative seismic velocity and vertical normal strain is suitable in all cases (Hatchell and Bourne, 2005). Observations from the same study also suggested that the velocity-strain dependence is larger when a rock is stretched compared to a compacting rock. When for instance a sandstone is stretched, fractures are induced, which has a severe influence on the velocities. Particularly for fractures induced normal to the direction of wave propagation (Hatchell and Bourne, 2005), showing a much larger effect on velocities compared to the linear trend calculated from regression analysis done on velocity versus porosity (Guilbot and Smith, 2002). A first-order approximation has been presented by both Røste et al. (2006) and Hatchell and Bourne (2005) relating relative velocity change and relative thickness change within a layer by a factor $\mathcal{R}$, see Eq. 1.3.

$$\frac{\Delta V_p}{V_p} = \mathcal{R} \cdot \left(-\frac{\Delta Z}{Z} \right) \qquad \text{or} \qquad \frac{\Delta V_p}{V_p} = \mathcal{R} \cdot \epsilon_{zz} \qquad (1.3)$$

This empirical rock physics relation links the geophysical observables and the physical properties of the rocks. The 4D seismic measurements can be related to the strain fields. From Eq. 1.3, compaction is associated with a positive strain, ϵ_{zz}, while the strain is negative for elongation, keeping $\mathcal{R} > 0$, using sign conversion as defined in Fjær et al. (2008). The factor $\mathcal{R}$ will depend on the rock properties of the layer and highly on the stress states. The rock properties will in a way be incorporated in the resulting strain the rock experiences during the particular stress field. Holt et al. (2016) rewrote Eq. 1.3 to better illustrate the stress path sensitivity of the $\mathcal{R}$-factor, see Eq.1.4.

Where $\Delta\sigma_z$ is the vertical stress change, and the first parenthesis is known as the stress sensitivity $(\frac{\Delta V_p}{V_p\Delta\sigma_z})$.

$$\mathcal{R} = \left(\frac{\Delta V_p}{V_p\Delta\sigma_z}\right)\left(\frac{\Delta\sigma_z}{\epsilon_{zz}}\right) \tag{1.4}$$

Bathija et al. (2009) found, from core measurements, that absolute values of $\mathcal{R}$ increase for sandstones and decrease for shales with decreasing confining pressure. Keeping the values of $\mathcal{R}$ constant from the surface, where we have unconfined stress state, to the reservoir where we have higher confined stress state, should be avoided.

The comparison of $\mathcal{R}$-factor values derived from core samples and 4D seismic, can be difficult for many reasons. It is hard to mask the geomechanical stress state in the laboratory to the in situ stress state in the subsurface. The $\mathcal{R}$-factor values derived from 4D seismic use the cumulative geophysical changes and therefore take the combined effect of the overburden and reservoir rock. The overburden is volumetric dominant, so the resulting $\mathcal{R}$-factor value for the usually shaly overburden will decrease the resulting $\mathcal{R}$-factor values. While for laboratory measurements the core sample is more restricted and will, therefore, give higher $\mathcal{R}$-factor values (Bathija et al., 2009).

Another factor that plays an important part is the geomechanical differences between the "in situ" conditions and the stress state during laboratory measurements. The unloading process the core plug has to go through when taken from a deep well, may have a significant influence on the elastic moduli of the rock. When the rock is under "in situ" conditions, cementation processes might occur at the grain contacts, but as the load disappears, the core will be exposed to tensile stress and these grain contacts will be deformed/weaken. These unloading conditions will also cause cracks, which diminish the elastic stiffness of the rock together with the acoustic velocities. When trying to mask the stress state during laboratory measurements, the cracks will close again, but this unloading-loading condition is causing core damaging effects. The resulting velocities and thus $\mathcal{R}$-factor value may not be representing the "in situ" behavior, but rather be related to core damaging effects (Fjær et al., 2008).

This core damaging effect was demonstrated by Nes et al. (2000), through a test on a synthetic cemented sandstone under stress. Figure 1.1 illustrate the difference between initiation of decreasing stress from "in situ" conditions, top curve, to reloading condition during laboratory measurements following the bottom curve. An increase in effective stress during "in situ" conditions could represent the depletion of a reservoir, see Figure 1.1. Dispersion effects and geometry upscaling effects are also mentioned as a potential cause of the discrepancy between field and core measurements (Kenter et al., 2004).
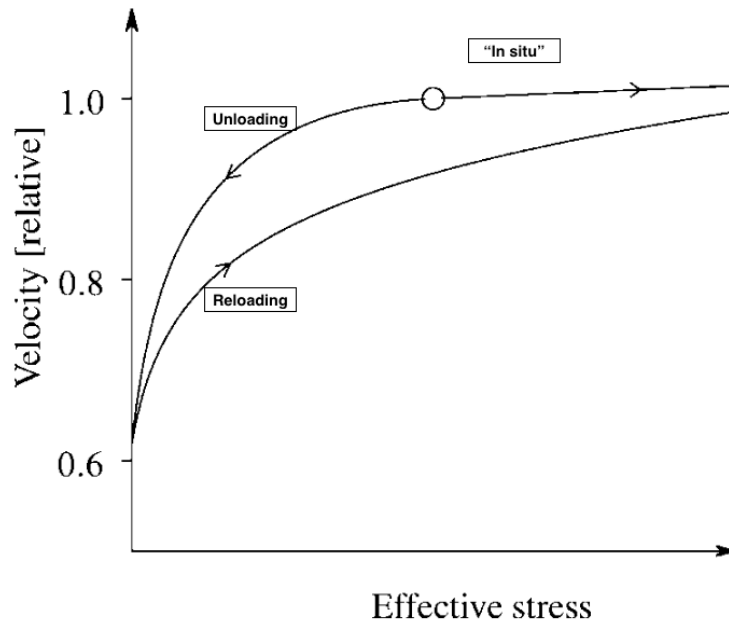
Figure 1.1: Upper curve representing the "in situ" stress path, compared to bottom curve representing the stress path during reloading after coring (Illustration modified from Fjær et al. (2008))

There are still unanswered questions related to the variation of the $\mathcal{R}$-factor. Knowing the $\mathcal{R}$-factor values will make it possible to quantify the effect of relative velocity change and relative thickness change on the resulting relative time shifts using Eq. 1.3 and 1.2. In the specialization project (Kvilhaug, 2016) the focus was to create a method to obtain values for the $\mathcal{R}$-factor in the overburden above a depleting reservoir. The objective was to utilize a geomechanical model together with 4D seismic and time-lapse bathymetry data to obtain the $\mathcal{R}$-values on synthetic data.

Inversion principals were used on Geertsma's geomechanical model (Geertsma, 1973) to calculate the model parameters that give the measured subsidence, provided from bathymetry data. By calculating $\frac{\Delta Z}{Z}$ from a geomechanical model and measuring $\frac{\Delta T}{T}$ from 4D seismic. We can through a global inversion process with a least-square error stopping criteria, calculate the dilation factor $\mathcal{R}$ for the overburden by combining Eq. 1.3 and 1.2. The error analysis performed on synthetic data in the specialization project (Kvilhaug, 2016), showed improvement in the definition of the minimum of the error function when utilizing data with position exceeding the lateral extent of the underlying reservoir.

The objective of the master's thesis is to obtain the $\mathcal{R}$-factor values in the overburden using real data. The following project will present the data preparation and assumptions needed in order to run the algorithm from the specialization project and the final results from the process. The time-lapse data is from the Ekofisk Field in the North Sea acquired in 2011 and 2014 and is provided by ConocoPhillips.

The geomechanical model used in this project has its limitations. It assumes a uniformly depleted disk-shaped reservoir situated within a linear-elastic, homogeneous and isotropic half space. The seismic data used alongside this model, reflects the Ekofisk Field with all its complexity regarding faults, lithological changes, anisotropy, different depletion/injection patterns, etc. The interaction between these two datasets will hence be associated with errors.

The following chapter, Ch. 2, will begin with an introduction to the Ekofisk Field. Followed by the theory applied in the global inversion process; the theory behind the geomechanical model by Geertsma (1973), on time-lapse seismic data and inversion theory. Ch. 3 will focus on the formulation of the inversion algorithm and presents the particular approach used in this project with two forward operators and the model parameters used. In Ch. 4 the input data from the Ekofisk Field will be introduced, and the data preparation needed prior to the inversion process. The results of the inversion process will be presented in Ch. 5 together with an analysis of the error function, followed by a discussion of the results in Ch. 6 and a summary and conclusion in Ch. 7.

Chapter 2

Theory

About 50 % of Section 2.1, about 60 % of Section 2.2 and 90 % of Section 2.4 are taken and revised from the Specialization project (Kvilhaug, 2016).

2.1 Ekofisk Field

In autumn of 1969, a discovery well was drilled by Phillips Petroleum Company and turned out to be the first and to this date largest discovery on the Norwegian continental shelf. Core samples collected from the wildcat well 2/4-2 between 3051 m and 3280 m turned out to be filled with oil. The two oil filled units were the Ekofisk- and Tor formation of Paleocene and late Cretaceous age. The field was named Ekofisk and is located in block 2/4 in the southern North Sea, see Figure 2.1. The Ekofisk field is a huge chalk structure draped over a salt pillow, with approximately 6.7 billion stock tank barrels of original oil in place (STBO) (Folstad, 2010). The reservoir rock is a highly fractured chalk with high porosity, majority ranging between 30-45 % (Nagel, 1998). The permeability is low, but natural fractures provide crucial secondary porosity and permeability in the chalk. The Ekofisk- and Tor formation are the two producing chalk units, located in the upper part of the 800 m thick chalk group, and the pay zone is approximate 300 m thick (Chilingarian, 1995). The elliptical anticlinal structure, confining the hydrocarbons within the reservoir is 5.4 km wide (E-W) and 11.2 km long (N-S) (Ottemöller et al., 2005).
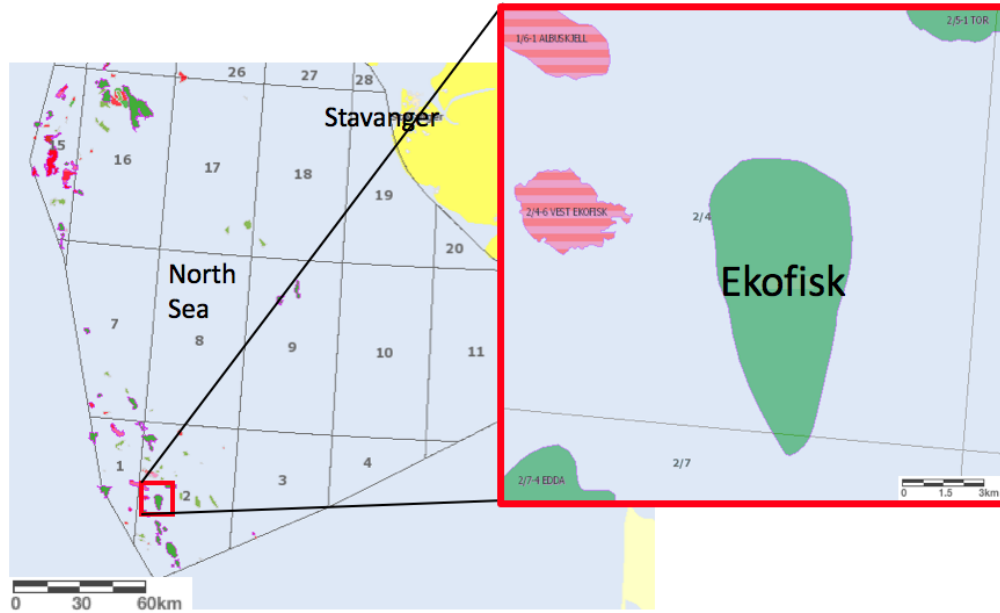
Figure 2.1: Location map of the North Sea, with Ekofisk Field within red box, adapted form NPD (2017)

By looking at the chalk reservoir rock under a microscope, see Figure 2.2b, it may be observed how the rock consist of particles primarily originating from algae skeletons known as coccosphere, see Figure 2.2a. Due to burial and diagenesis, few of these coccospheres are intact but rather broken into smaller pieces named coccolith and platelet. The primary mineral in the Ekofisk chalk is calcite, but silica and clay minerals are also present.
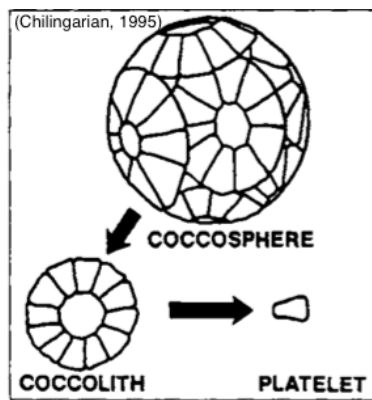
(a) Illustrative representation of the coccosphere, coccolith, and platelet which the Ekofisk chalk consist of

(b) SEM image of a rocksample of the Ekofisk chalk

Figure 2.2: Ekofisk chalk composition

The overburden consists mostly of clay-rich shales, and the lithological changes are relatively small (Nagel, 1998). The overburden consists of the Nordland Group (Middle Miocene to Recent), Hordaland Group (Eocene-Early Miocene), and Rogaland Group (Paleocene - Early Eocene), moving downwards in the stratigraphic succession (NPD, 2017). A polygonal fault pattern characterizes most of the Hordaland Group, with vertical fault extent that can reach up to 1 km (Ottemöller et al., 2005). Above the Rogaland Group, gas has slowly migrated up and possibly distributed along laterally discontinuous thin layers. The concentration of gas is present above the crest of the anticlinal structure (Nagel, 1998). An overpressured zone has also been reported about 900 m down for the crestal wells (CoP, 2010). Both of these effects are causing an impact on the P-wave velocities, making imaging challenging directly above the crest of the Ekofisk structure. This area is often referred to as the Seismically Obscured Area, hereafter referred to as SOA.

The reservoir is located between 2900-3300 m below the seafloor, with a water depth of 70-75 m. The fields initial recovery rate was at 17 % during production from ordinary pressure depletion. Then vast water and gas injection planes have increased the recovery factor, and it is now estimated to be over 50 % (NPD, 2017). As mentioned in the Ch. 1, the extensive compaction of the reservoir unit and the resulting subsidence at the seabed slowed down after water injection started. Due to the water weakening effect of the chalk reservoir and the under-compacted weak shale and mudrocks of the overburden, the reservoir compaction was almost instantaneously being transferred as seabed subsidence. The fact that the subsidence to compaction rate is not equal to one, implies that the overburden is being stretched. Arching effects may be part of the explanation why the seabed subsidence show less displacement than the reservoir compaction.

Since 1984 when the subsidence problem was recognized, there has been various attempts to monitor the effect. A compaction monitor well was drilled in 1986, measuring the change in distance between the markers of radioactive material implanted in the formation. The subsidence is further monitored using GPS and bathymetric data. Time-lapse seismic measurements can be used to detect the changes in seismic traveltime for different seismic reflectors in order to give additional information about the geomechanical changes. Casing deformation data has also given an insight of the movement in the overburden as well as in the reservoir (Nagel, 1998).
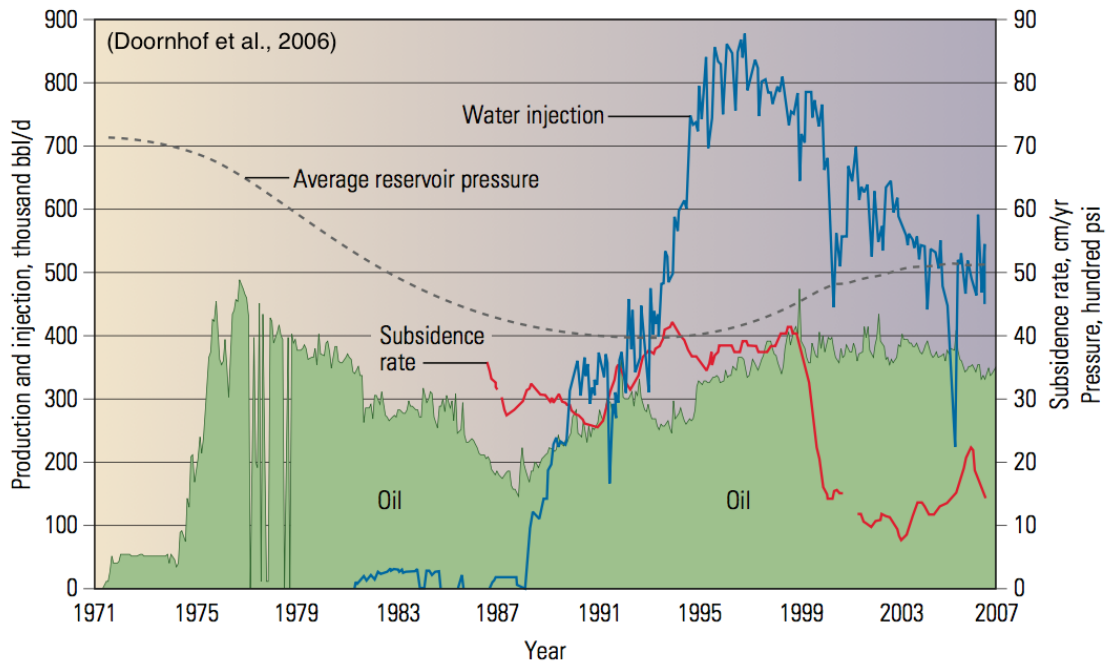
Figure 2.3: Ekofisk field production history until 2007. Average reservoir pressure (dashed gray) increased after the continuous increase in water injection rate (blue). Subsidence rate (red) decreased after 1999

The compaction rate went from 0.4 m/yr to around 0.1 m/yr after repressurization of the reservoir using water injection (Ottemöller et al., 2005). From Figure 2.3 we see that after average reservoir pressure (dashed gray line) had started increasing around 1994-1995, the subsidence rate (red line) did not decrease until 1998. Creep of the overburden can cause the reaction between compaction and subsidence to be delayed, but not by a number of years as seen here (Doornhof et al., 2006). Laboratory measurements and field measurements from for instance the compaction well has supported that water weakening of chalk can explain this delay (Sylte et al., 1999). The chemical reaction between the calcite and water will weaken the reservoir rock, so when the reservoir is swept with water, the reservoir will be weakened to a certain limit before the process slows down and hence also the rate of subsidence. The continuing reservoir compaction today is associated with the balance between the ongoing repressurization of the reservoir and the water weakening of chalk (Doornhof et al., 2006). Tests have shown that increasing water saturation will weaken the strength of the chalk reservoir until fully water weakened state is reached at approximately water saturation of 25 % (Hermansen et al., 2000).

2.2   Geomechanical Modeling

Geomechanics studies the Earths response when exposed to stress and strain fields. When producing from a reservoir the resulting decrease in pressure is essentially a reduction in the pressure from the fluids which was keeping the pores open. The drop in pore pressure results in an increase in effective stress from the overburden $\Delta\sigma'_V$. If we assume the reservoir rock consists of an isotropic, homogeneous rock and the theory of poroelasticity apply, Eq. 2.1 can be used to show how the effective stress increase as we reduce the pore pressure (negative Δp_f), which can result in reservoir compaction. The stress/weight of the overburden σ_V is the same, $\Delta\sigma_V = 0$, so the effective stress increase is caused by the pore pressure reduction. The magnitude of reservoir compaction depends on this decrease in pore pressure, the compressibility of the reservoir rock and the fluid compressibility (Bathija et al., 2009). The resulting alteration of the stress regime, as a result of the reservoir compaction, will increase the possibility of fault reactivation in the stretched overburden. The opposed operation of water injection will cause the pore pressure to increase and, hence, the effective stress to decrease. The effective stress along existing fault planes will be reduced, and the reservoir is more likely to experience fracture growth and fault reactivation. Any alteration of the stress regimes will increase the possibility of fracture growth and fault reactivation inside and outside the reservoir (Segall and Fitzgerald, 1998).

$$\Delta\sigma'_V = \Delta\sigma_V - \alpha\Delta p_f \tag{2.1}$$

The α parameter is the Biot coefficient defined by Eq. 2.2, for chalk $\alpha \approx 1$.

$$\alpha = 1 - \frac{K_{fr}}{K_s} \tag{2.2}$$

The factor K is an elastic modulus, named Bulk modulus, see Eq. 2.3. K is the ratio of hydrostatic stress $\sigma_p = \sigma_z = \sigma_x = \sigma_y$ relative to volumetric strain $\epsilon_{vol} = \epsilon_x + \epsilon_y + \epsilon_z$. Where x,y and z subscripts are referring to the 3 principal directions.

$$K = \frac{\sigma_p}{\epsilon_{vol}} \tag{2.3}$$

The subscripts "fr" and "s" in Eq. 2.2 are referring to the framework bulk modulus of the rock and the bulk modulus for the individual rock grain/minerals. K_s will always be much larger than the framework bulk modulus K_{fr}. The framework or skeleton of the rock is referring to the degree of sorting, cementation, and porosity of the rock. An increase in porosity results in a sharp decrease in K_{fr}. Eq. 2.4 is known as the Biot-Gassmann equation and shows how the resulting Bulk modulus depends on the other mentioned factors as well as the fluid bulk modulus K_f. This equation is often used to demonstrate the effect of fluid substitution on seismic properties, as the Bulk modulus appears in the simplest equation for plane wave compressional velocity, see Eq. 2.5.

$$K = K_{fr} + \frac{K_f}{\phi} \frac{(1 - \frac{K_{fr}}{K_s})^2}{1 + \frac{K_f}{\phi K_s}(1 - \phi - \frac{K_{fr}}{K_s})} \tag{2.4}$$

$$V_p = \sqrt{\frac{K + \frac{4}{3}G}{\rho}} \tag{2.5}$$

The Young's modulus, E, is another elastic modulus quantifying how resistant the medium is to uniaxial compaction, see Eq. 2.6. In this equation, the subscript i is one of the three principal directions, σ_{ii} is the uniaxial stress, and ϵ_{ii} the resulting deformation/strain in the same direction.

$$E = \frac{\sigma_{ii}}{\epsilon_{ii}} \tag{2.6}$$

When a medium is compressed, it results in a reduction in height and a resulting increase in width. If the medium is isotropic and homogeneous, the deformation in the two horizontal directions ϵ_{xx} and ϵ_{yy} will be the same. The ratio between the two defines the Poisson's ratio given by Eq. 2.7.

$$\nu = -\frac{\epsilon_{xx}}{\epsilon_{zz}} = -\frac{\epsilon_{yy}}{\epsilon_{zz}} \tag{2.7}$$

Changes in the effective stresses within a reservoir can be used to calculate the resulting deformation by using Hooke's law Eq. 2.8-2.10. The lower-case h and H now stands for the two horizontal directions, while V stands for the vertical direction.

$$E_{fr}\epsilon_h = \Delta\sigma'_h - \nu_{fr}(\Delta\sigma'_H + \Delta\sigma'_V) \tag{2.8}$$

$$E_{fr}\epsilon_H = \Delta\sigma'_H - \nu_{fr}(\Delta\sigma'_h + \Delta\sigma'_V) \tag{2.9}$$

$$E_{fr}\epsilon_V = \Delta\sigma'_V - \nu_{fr}(\Delta\sigma'_H + \Delta\sigma'_h) \tag{2.10}$$

The effective stresses, $\Delta\sigma'$, defined in Eq. 2.8-2.10, are on the same form as in Eq. 2.1, but here for each of the principal directions V, H and h.

It is a common simplification to assume that the reservoir is a lot wider than it is thick, and that the reservoir compaction is only vertically, known as uniaxial compaction. The two assumptions is given by Eq. 2.11 and 2.12. Where h in Eq. 2.12 is referring to the height of the reservoir.

$$\epsilon_h = \epsilon_H = 0 \tag{2.11}$$

$$\frac{\Delta h}{h} = -\epsilon_V \tag{2.12}$$

Inserting the assumption in Eq. 2.11, 2.8 and 2.9, we get an equal expression for $\Delta\sigma'_h$ and $\Delta\sigma'_H$. By using this expression together with Eq. 2.12 in Hook's law for vertical deformation Eq. 2.10, and assuming constant vertical stress during depletion of the reservoir, $\Delta\sigma_V = 0$, we get the compaction formula given by Eq. 2.13.

$$\frac{\Delta h}{h} = \frac{1}{E_{fr}}\frac{(1+\nu_{fr})(1-2\nu_{fr})}{1-\nu_{fr}}\alpha\Delta p_f \tag{2.13}$$

The $\frac{1}{E_{fr}}\frac{(1+\nu_{fr})(1-2\nu_{fr})}{1-\nu_{fr}}$ term may be defined as the uniaxial compressibility or the compaction coefficient C_m. Eq. 2.14 shows how it is related to other elastic moduli (Fjær et al., 2008).

$$C_m = \frac{1}{E_{fr}}\frac{(1+\nu_{fr})(1-2\nu_{fr})}{1-\nu_{fr}} = \frac{1}{3K_{fr}}\frac{1+\nu_{fr}}{1-\nu_{fr}} = \frac{1}{H_{fr}} = \frac{1}{\lambda_{fr}+2G_{fr}} \tag{2.14}$$

The theory from geomechanics can be used to estimate the resulting stress and strain fields of the overburden due to production-related changes. One of these geomechanical models is the one derived by Geertsma (1973). Geertsma used the theory of poroelasticity to calculate the displacement interactions between a compacting reservoir and its elastic surroundings resulting in subsidence. His model builds upon two assumptions (Geertsma, 1973).

- Linear stress/strain relations

- Uniform deformation, the elastic properties of the reservoir and the overburden is the same

Geertsma (1973) geomechanical model is based upon the stress-strain relation for the elastic case given by Eq. 2.15.

$$\sigma_{ij} = 2G\left[\epsilon_{ij} + \frac{\nu}{1 - 2\nu}\epsilon_{vol}\delta_{ij}\right] - (1 - \beta)p_f\delta_{ij} \tag{2.15}$$

where

$$\sigma_{ij} = \text{Bulk stress component}$$

$$G = \text{Shear modulus/Rigidity modlulus}$$

$$\epsilon_{ij} = \text{Strain component}$$

$$\nu = \text{Poisson's ratio}$$

$$\epsilon_{vol} = \text{Volumetric strain}$$

$$\delta_{ij} = \text{Kronecker delta}$$

$$\beta = \text{Ratio between the rock matrix compressibility and the rock bulk compressibility}$$

$$p_f = \text{Pore pressure}$$

The model derived by Geertsma (1973) using poroelasticity is mathematically similar to the theory of thermoelasticity. The concept of "nuclei of strain" is applied, where the pore pressure reduction of Δp_f within a small finite volume of arbitrary shape may produce the displacement components outside the reservoir. The equation for radial displacement at a distance r outside a depleting sphere of radius R_0 is given by Eq. 2.16, where the term u_0 denotes the radial displacement at the surface

of the depleting sphere.

$$u(r) = u_0 \frac{R_0^2}{r^2} \tag{2.16}$$

The displacement $\nabla \cdot \vec{u}$ is related to the volumetric strain ϵ_{vol} given by Eq. 2.17. Where V now is referring to the volume of the sphere.

$$\epsilon_{vol} = \nabla \cdot \vec{u} = -\frac{\Delta V}{V} \tag{2.17}$$

The volumetric change ΔV of the depleted sphere is given by Eq. 2.18

$$\Delta V = \nabla V \vec{u} = -4\pi r^2 \cdot (u_0 \frac{R_0^2}{r^2})$$
$$\Delta V = -4\pi R_0^2 u_0 \tag{2.18}$$

The volumetric strain is also given by Eq. 2.19 as a direct result of stress aching for a reservoir with same elastic properties as the overburden. Eq. 2.19 can also be shown by using the arching coefficients γ.

$$\epsilon_{vol} = -\alpha C_m \Delta p_f \tag{2.19}$$

By combining Eq. 2.19 and Eq. 2.17, we can get an expression for the displacement at the surface of the depleting sphere u_0 given by Eq. 2.20.

$$u_0 = -\frac{C_m V \alpha \Delta p_f}{4\pi R_0^2} \tag{2.20}$$

We then get the expression for the displacement at a distance r outside a depleting sphere within an infinite space given by Eq. 2.21.

$$u(r) = -\frac{C_m}{4\pi} V \alpha \Delta p_f \frac{1}{r^2} \tag{2.21}$$

Eq. 2.21 does not account for the seabed but is rather applicable to an infinite space. By using a known thermoelectric solution (Mindlin and Cheng, 1950a,b), we can account for the surface, where we know the effective vertical stress have to be zero. The resulting displacement field outside a depleting sphere within a semi-infinite space derived by Geertsma (1973) is given by Eq. 2.22.

$$\vec{u} = \frac{C_m}{4\pi} \left(\frac{\vec{R_1}}{R_1^3} + (3 - 4\nu)\frac{\vec{R_2}}{R_2^3} - \frac{6z(z + D)\vec{R_2}}{R_2^5} + \frac{2\hat{z}}{R_2^3}[(3 - 4\nu)(z + D) - z]V\alpha\Delta p_f \right) \quad (2.22)$$

where

$$R_1^2 = r^2 + (z - D)^2$$
$$R_2^2 = r^2 + (z + D)^2$$
$$\hat{z} = \text{unit vector in z-direction}$$
$$\nu = \text{Poisson's ratio}$$
$$C_m = \text{Compaction coefficient}$$
$$V = \text{Initial volume of depleting sphere}$$
$$\alpha = \text{Biot/Poroelasticity coefficient}$$
$$\Delta p_f = \text{Change in reservoir pore pressure}$$
$$D = \text{Depth from surface to center of depleting sphere}$$
$$z = \text{Vertical position from the surface}$$
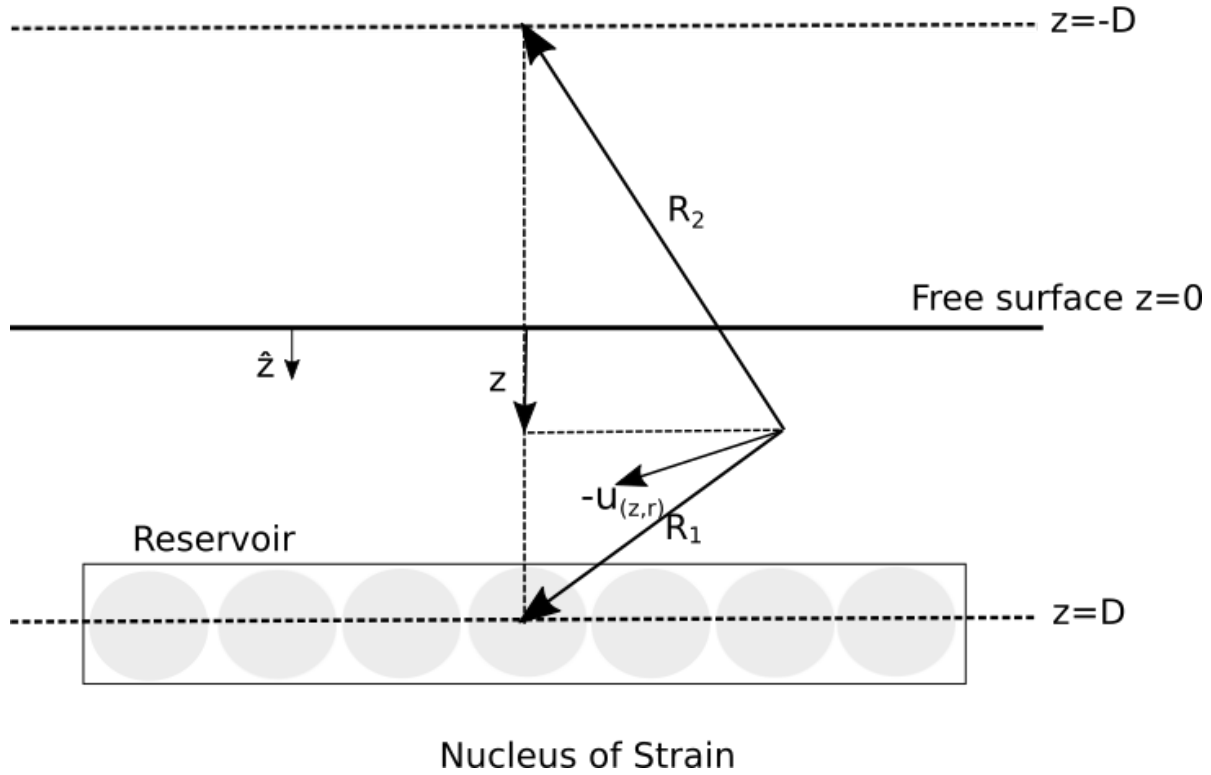
Nucleus of Strain

Figure 2.4: Sketch of Geertsma's nucleus of strain model. $u_{(z,r)}$ indicate the direction of particle movement. Note that positive z-direction is downwards. (Illustration adapted from Fjær et al. (2008))

By relying on the superposition of many nuclei/spheres, we can calculate the resulting total subsidence. In theory, we can with numerical methods estimate the subsidence for any arbitrarily shaped reservoir. The calculation builds on elastic deformation and no contrast between the reservoir and the surroundings. So the model will not be applicable for precise calculations, but if we choose a disk-shaped reservoir, we can get an analytical solution and a general understanding of the subsidence problem. The problem is shown in Figure 2.4, the resulting vertical- and radial displacement are given by Eq. 2.23 and 2.24. The analytical solution is given by solving Hankel integrals involving Bessel functions. Parts of the solution presented by Luke (1962) is printed in Appendix C.1. These solutions are also dependent on the solution of complete and incomplete elliptical integrals, also posted in Appendix C.1. For the disk-shaped case, the I_i parameters are commonly called the Geertsma integrals. For $r = 0$ we need to use the equation posted in Appendix C.1.

$$u_z = \frac{C_m \alpha R h \Delta p_f}{2} \left[\frac{z-D}{|z-D|} I_3(|z-D|) - (3-4\nu) I_3(z+D) - 2z I_4(z+D) \right] \quad (2.23)$$

$$u_r = \frac{C_m \alpha R h \Delta p_f}{2} \left[I_1(|z-D|) + (3-4\nu) I_1(z+D) - 2z I_2(z+D) \right] \quad (2.24)$$

Figure 2.5 and 2.6 show how the displacement is propagated up through the overburden for a disk-shaped reservoir (white rectangle) seen as a vertical section through the center of the disk-shaped reservoir. The parameters used to create the image was taken from the synthetic study performed in the specialization project (Kvilhaug, 2016), Table C.1 with these values can be found in Appendix C.1.
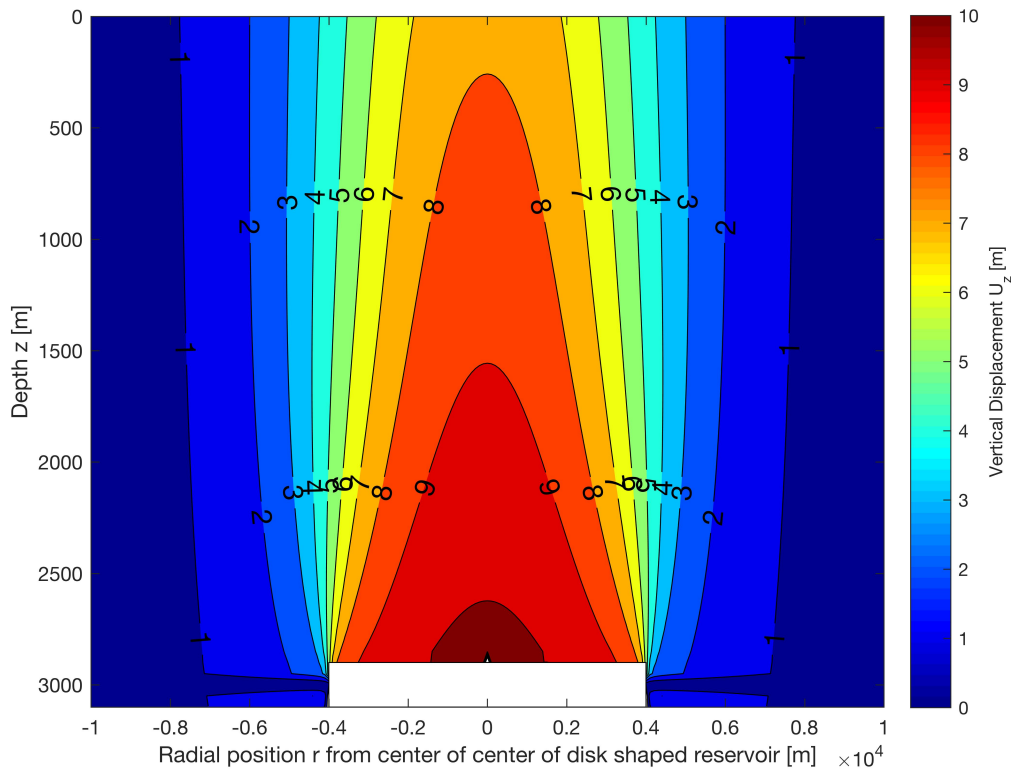
Figure 2.5: Vertical displacement u_z, vertical section of disk-shaped reservoir illustrated as a white rectangle
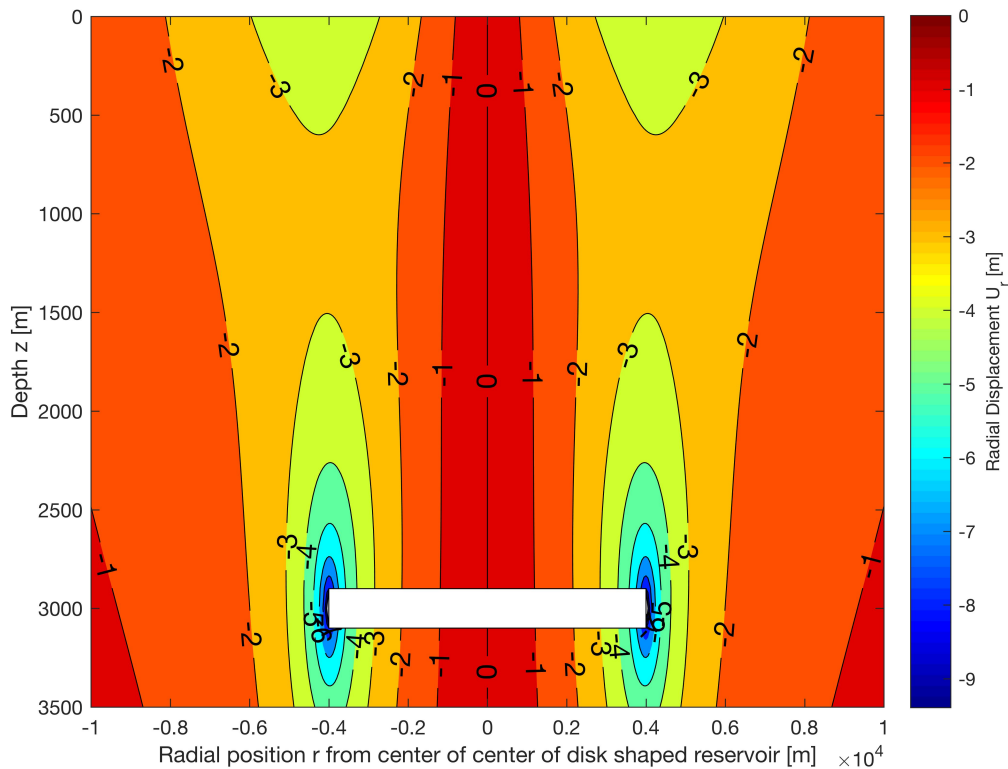
Figure 2.6: Radial displacement u_r, vertical section of disk-shaped reservoir illustrated as a white rectangle

Figure 2.7 show the vector field/displacement field of the radial and vertical displacement as a response to a depleting reservoir (dashed lines) with parameters taken from Table C.1. We see increasing radial component on the edge of the reservoir as a response to arching, implying increasing shear stress.
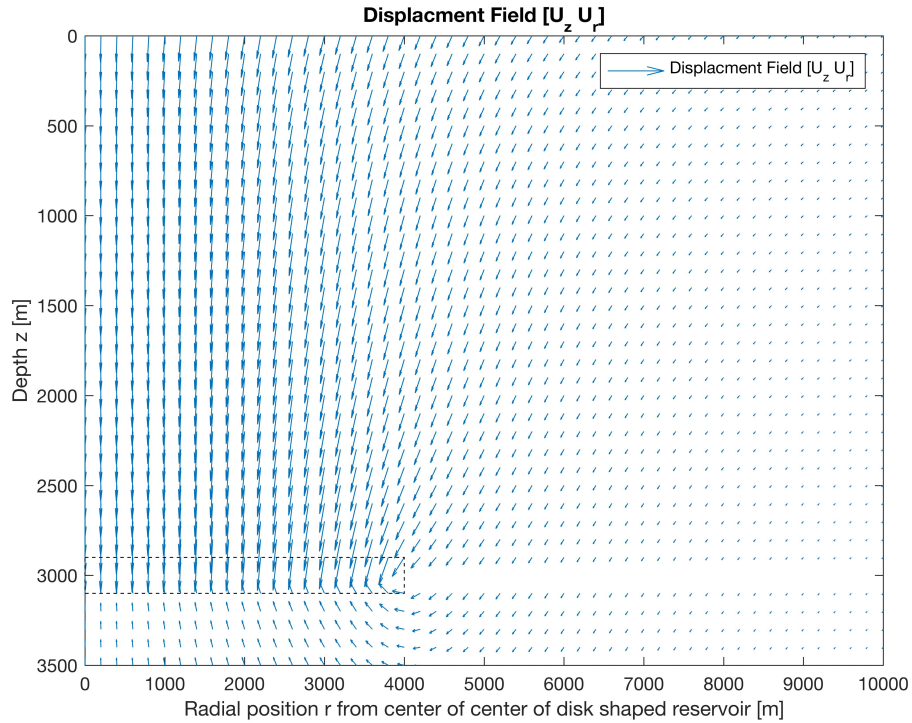
Figure 2.7: Displacement field for radial and vertical displacement

From these previous plots, it is clear that the geomechanical model presented by (Geertsma, 1973) shows alterations in the stress state for the rocks surrounding the depleting reservoir. We see from Figure 2.5 that the vertical displacement of the surface is smaller than right above the reservoir, even though the elastic properties of the reservoir and the surrounding rocks are the same in Geertsma's model. The aching coefficients γ is causing the change in the stress fields, see Eq. 2.25. The aching effect in Geertsma's geomechanical model is dependent on the ratio between the thickness and the lateral extent of the depleting zone (the aspect ratio). The vertical arching coefficient or stress path coefficient γ_V will increase for decreasing aspect ratio ($e = \frac{h}{2R}$). The effect of arching is expressed by a $\gamma_V > 0$. The arching effect can be explained by the redirection of the stresses on to the shoulders of the reservoir. The vertical stress relief σ_V within and above the reservoir result in increasing σ_V on the edge of the reservoir, together with increasing horizontal stress σ_h within

the reservoirs outer edge and decreasing σ_h outside the reservoir.

$$\gamma_V = \frac{\Delta\sigma_V}{\Delta p_f}$$

$$\gamma_H = \gamma_h = \frac{\Delta\sigma_h}{\Delta p_f} \tag{2.25}$$

Figure 2.8 shows the arching effect for a reservoir at 2000 m depth with increasing radius R of 2000, 4000 and 6000 m. The figure shows how the vertical displacement above the center of a disk-shaped reservoir increases for increasing lateral extent of the reservoir, hence, less arching or shielding of vertical stress expressed by positive γ_V for decreasing aspect ratio. The dotted rectangle in Figure 2.8 illustrate only the location and vertical extent of the reservoir, seen as a vertical section, not the lateral extent. The other parameters needed to produce the illustration are taken from Table C.1
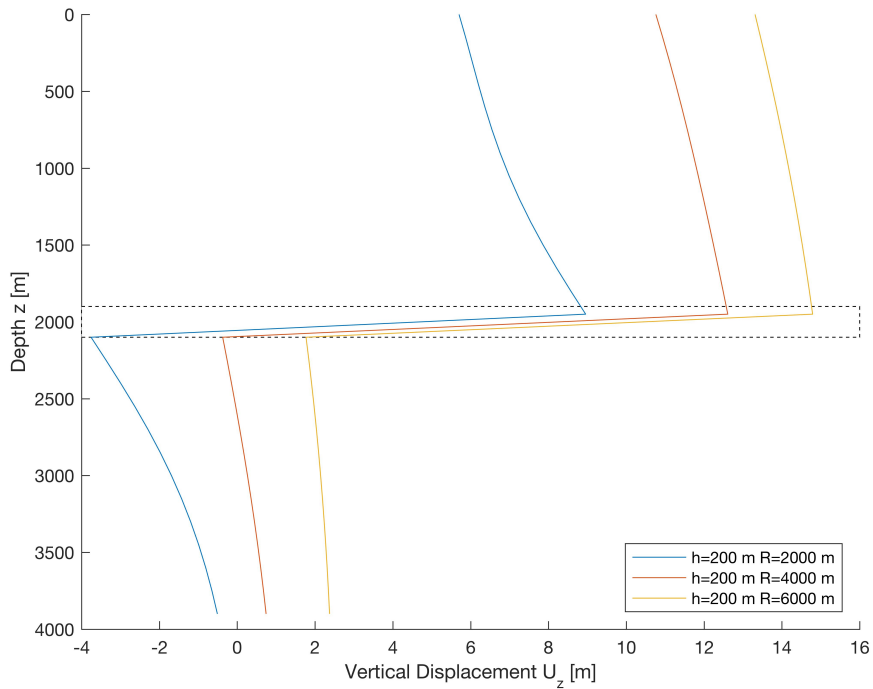
Figure 2.8: The arching effect shown for three reservoirs with different aspect ratios

Due to the assumption of no contrast in elastic properties, it can be shown that $\gamma_V + 2\gamma_h \approx 0$ (Fjær et al., 2008). Constant mean stress represents the surroundings of the pressure altered reservoir. The volumetric strain $\epsilon_{\text{vol}} \approx 0$ and pure shear loading represents the overburden. The amount of speed

up or slow down in the overburden is, as mentioned in Ch. 1, dependent on the stress sensitivity and stress path κ, Eq. 2.26.

$$\kappa = \frac{\gamma_h}{\gamma_V} \tag{2.26}$$

2.3 4D Seismic and Reservoir Monitoring

Acquired seismic data can give valuable information about the subsurface. It can create an image that we can interpret, and identify potential oil and gas reservoirs. When a prospect is identified, the ultimate goal of all oil companies is to produce as much as possible from these resources. That is where 4D seismic or time-lapse seismic may play a significant role.

Time-lapse seismic data essentially means acquiring at least two sets of seismic surveys over the same area, one base survey before production, and one monitor survey after producing for a while. The comparison between the two can give valuable information regarding reservoir performance and future well planning.

If the identified petroleum reservoir is interpreted as relatively homogeneous, the business advantages with 4D seismic will not be as significant as if we were dealing with fields with more complex reservoirs. Since the main strength of 4D seismic is the ability to identify trapped hydrocarbon pockets, which been unswept using the existing producing wells.

These untapped hydrocarbon pockets may be possible to detect and target due to the changes the reservoir experiences when depleted. The most important factors are stated below (Bjorlykke, 2010).

- Change in fluid saturation

- Change in pore pressure

- Change in layer thickness

- Change in temperature

Rock physics can provide the link between critical reservoir parameters and seismic parameters. Such reservoir parameters can be fluid saturation and pore pressure. The simple Gassmann equation, Eq. 2.4, presented in Section 2.2, shows how the saturated Bulk modulus, K, is affected by the fluid's bulk modulus K_f. The change in Bulk modules can further be used in the simple equation for P-wave velocity (Eq. 2.5) to calculate how the seismic velocities change with the saturation of different fluids. The effect of such velocity changes and pore pressure changes is what we see manifest themselves on seismic data as amplitude changes and time shifts. From a study at the Gullfaks Field (Bjorlykke, 2010), Figure 2.9 shows the relative change in seismic parameters with saturation change and pore pressure change, based on rock physics theory.
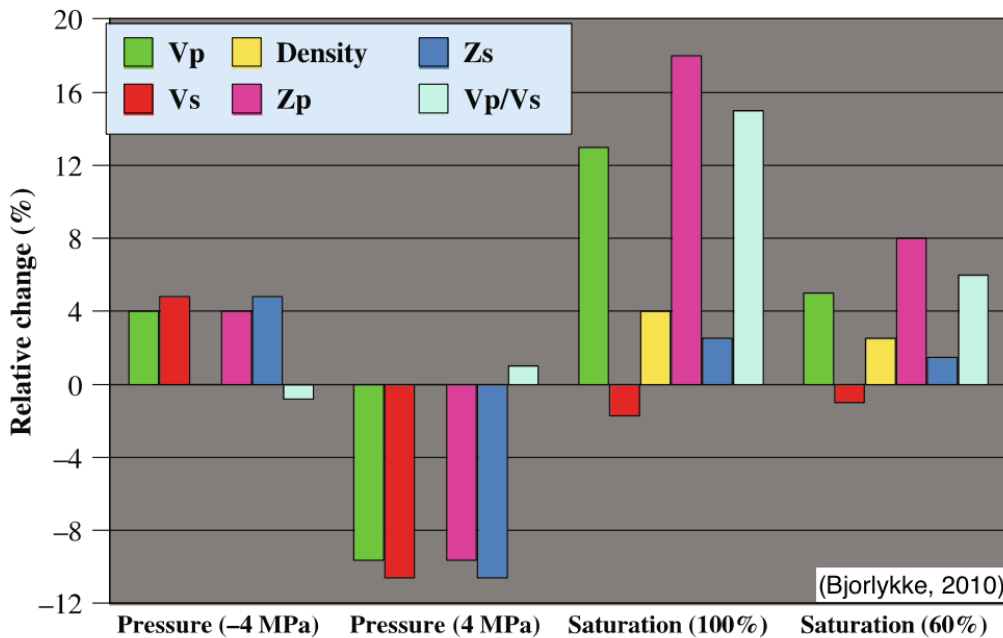
Figure 2.9: Relative change in seismic parameters with saturation and pore pressure change

The effects presented for pore pressure change in Figure 2.9, and more detailed shown in Figure 2.10, are produced from ultrasonic core measurements. The measurements will as mentioned in Ch. 1 only be performed under simulated in situ stress conditions and will be affected by the unloading process during coring. There will also be an issue related to upscaling the small core sample onto the seismic scale. The results from these core measurements presented in Landrø et al. (2001), state that one should expect P-wave velocity increase due to pore pressure decrease and a decrease in P-wave velocity when increasing the pore pressure, see Figure 2.10. If the change in velocity is

large enough, this change will manifest itself as detectable seismic time shifts.

The asymmetrical impact of pore pressure changes on seismic data

Typical Vp versus effective pressure curve obtained from core measurements
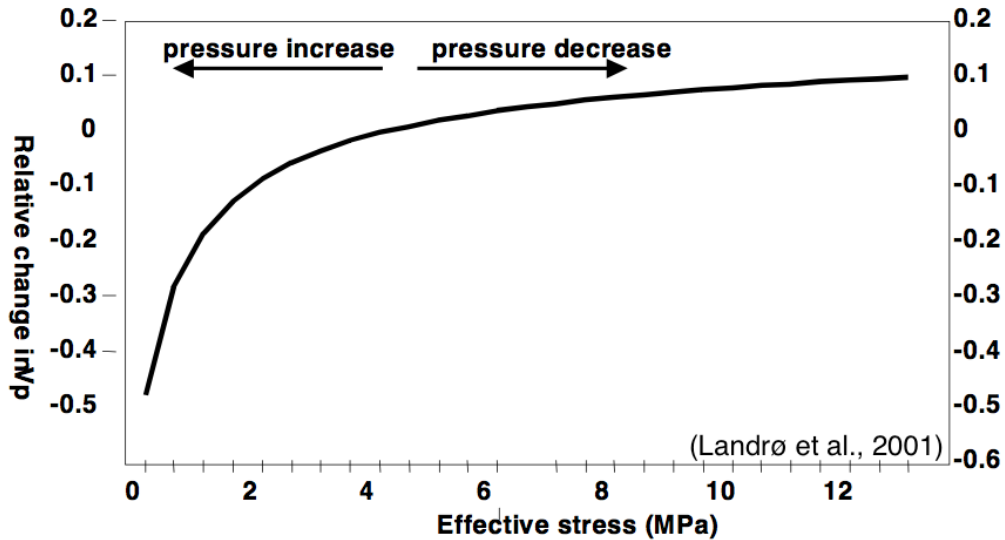
Figure 2.10: Effect of change in effective stress on relative P-wave velocity

The amplitude changes we see on time-lapse data are local features compared to time shifts for the same interface. The amplitude recorded on the seismic trace represents how prominent the acoustic impedance is across the interface. If the reservoir rocks geomechanical properties are "soft" enough, a change in either of the factors stated above as bullet points will cause a change in amplitude. That is why soft rocks such as sandstone and high porosity chalk, are best suited for 4D seismic studies. From fields with such soft reservoir, Kenter et al. (2004) developed a method to identify sealing faults and areas of different pore pressure based on 4D "fingerprints". Using theory based on stress arching, presented at the end of Section 2.2, they showed modeled time shifts which corresponded to measured time shifts from the overburden associated with heterogeneities within the reservoir. Their model purposed that such heterogeneities will function as stress attractors and will be recorded as negative time shifts or relatively less positive time shifts above in the overburden. Such heterogeneities can be sealing faults, where the stress will increase at the undrained fault block with different pore pressure. Sections with less compressible or thinner reservoir rock could also be such stress attractors.

Some fields will experience severe geomechanical changes within the reservoir during depletion. Leading to repercussions for the overburden, as observed at the Ekofisk Field, with around 10 m subsidence at the seafloor (NPD, 2017). In these cases, the focus of monitoring the changes of the subsurface is not just a focus on increasing the recovery factor, but also to decrease the chances of well instability and other HSE issues.

In 2010 ConocoPhillips installed a permanent reservoir monitoring system called Life of Field Seismic (LoFS) at the seafloor. The first repeated seismic survey acquired in 1999 after 28 years of production, showed compaction-induced geomechanical changes in the overburden, resulting in a massive time shift of 20 ms for the top reservoir reflector (Bertrand et al., 2014). At the date of installation, the amount of water injected since the initiation in 1987 was above three billion barrels of seawater (Folstad, 2010). The importance of understanding the drainage pattern of these water-fronts was of significance for further well planning and understanding of the compartmentalization of the reservoir. After installation, the risk of encountering water-swept zones had been reduced and led to accelerated production and fewer redrills (Folstad, 2010).

By installing the LoFS system it was not only easier to acquire new data over the area, but the data quality also tends to increase with ocean bottom seismic systems (OBS). OBS systems are often referred to as 4-C seismic, which stands for four component seismic. By placing receivers at the seafloor, it is possible to record data not only in vertical direction but also in horizontal direction, making it possible to record the converted PS-waves, the concept is shown in Figure 2.11.
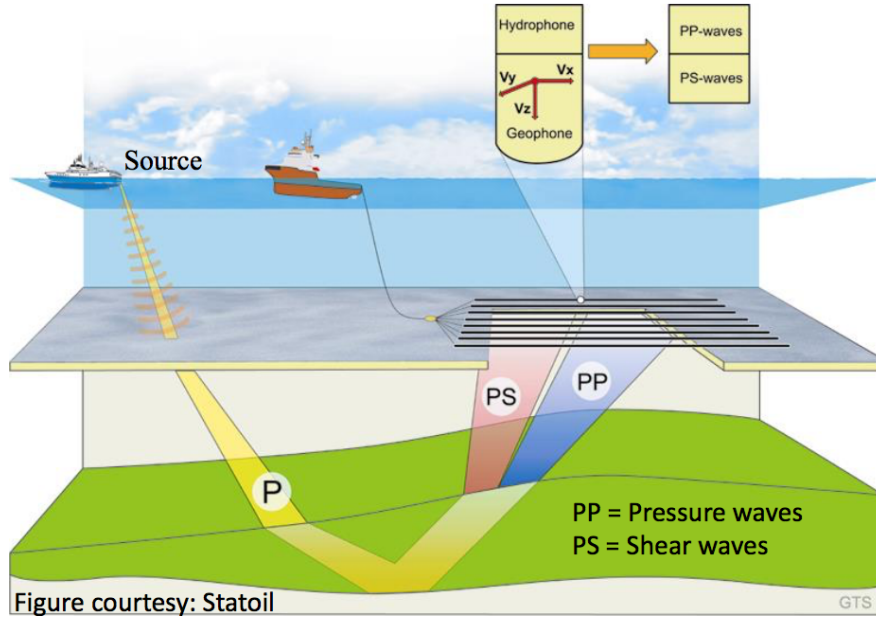
Figure 2.11: Simplified illustration showing the principles of 4-C seismic

The simplest equation for S-wave velocity is given by Eq. 2.27, applicable in a homogeneous isotropic medium.

$$V_s = \sqrt{\frac{G}{\rho}} \tag{2.27}$$

The shear modulus, G, in Eq. 2.27 is equal to zero for fluids, which mean that the only way to physically measure these converted pressure waves to shear waves, is by having the receivers at the seabed. One powerful advantage in recording S-waves is their ability to see through gas clouds. S-waves will not be affected as much by pore fluids as P-waves. They will just be slightly affected by the density term ρ, which is influenced by the different fluid saturation, see Eq. 2.28. Density is given by ρ where the subscript s is the solid/matrix density. The subscripts g, o and w stands for gas, oil and water and S is the fraction of saturation for either of these fluids.

$$\rho = \left(\rho_g S_g + \rho_o S_o + \rho_w S_w\right)\phi + \left(1 - \phi\right)\rho_s \tag{2.28}$$

The effect of imaging with converted waves and the ability to use multi-azimuth data, improved the data quality on Ekofisk severely. The repeatability has also increased drastically after implementation of the LoFS system. Bertrand et al. (2014) report that NRMS-values have decreased

from 12 % on regular streamer data down to the order of 4-5 % on LoFS data. NRMS stands for the normalized root-mean-square error and is a common way to quantify repeatability between a base and monitor survey (Bjorlykke, 2010). This low NRMS error allows us to detect smaller 4D responses. ConocoPhillips report that time shifts as little as 0.2 ms and amplitude changes on the order of 2-3% can be detected (Bertrand et al., 2014).

2.4   Inversion Theory

When we have the result but do not know what caused the event, an inversion problem can be useful to formulate. An inversion problem uses the result to calculate the cause. A forward problem takes the causes m and calculates the results d using the forward operator g, see Eq. 2.29.

$$d = g \cdot m \tag{2.29}$$

where

$$d = \text{Data vector}$$
$$g = \text{Forward matrix}$$
$$m = \text{Model parameters}$$

If the inversion problem is linear, it can be expressed by Eq. 2.30.

$$m = g^{-1} \cdot d \tag{2.30}$$

In reality, g is rarely invertible, and most often we need to rely on numerical methods in order to determine the best model parameters. To get information about the model parameters we need to do some observations during some physical experiments or modeling. The data space will be where this information is stored, see Eq. 2.31.

$$d = \begin{bmatrix} d_1^i \\ d_2^i \\ \vdots \end{bmatrix} \qquad (2.31)$$

In Tarantola (2005) d is calculated as a "forward problem", where the observable values d is predicted error-free and match the given model parameters m. A forward operator g is required to produce the model parameters m, which is represented by a set of equations, and express the physical system under study as a mathematical model.

$$d_{\text{obs}} = g(m) \qquad (2.32)$$

The inversion process tries to find the model parameters m that represent the data vector d_{obs} the best by using the forward operator with different values of m until the misfit between the observed data d_{obs} and d ($||d_{\text{obs}} - d||$) is minimized. In other words, the primary goal of the inversion process is to find the minimum of an error function. One such error function based on the principal of least-squares is given by χ in Eq. 2.33.

$$\chi^2 = \frac{\sum_i (d_{\text{obs}}^i - d^i)^2}{\sum_i (d_{\text{obs}}^i)^2} \qquad (2.33)$$

There are various inversion algorithms available to solve this problem. In this project, the method used is a global inversion method. This enumerative or grid-search based method involves a search through each point in the predefined model space to identify the best model parameters.

The model space for each model parameter will be defined by a m_{max}^i and m_{min}^i values, and with a search increment Δm^i (Sen and Stoffa, 2013). The total number of values each model parameter m^i can have, is then given by N^i in Eq. 2.34

$$N^i = \frac{m_{\text{max}}^i - m_{\text{min}}^i}{\Delta m^i} \qquad (2.34)$$

Chapter 3

Method: Inversion Using Geomechanical Modeling

The inversion process presented in this chapter was developed in the Specialization project (Kvilhaug, 2016), about 80 % of Ch. 3 is, hence, taken and revised from the Specialization project.

3.1   Inversion Algorithm: Forward Operator

Figure 3.1 illustrate the idea behind the inversion problem. To use known subsidence between two bathymetry surveys, together with known time shifts, calculated from two seismic vintages, as constraining data for the inversion process. The ultimate goal of the inversion process is to define a set reservoir parameters together with the dilation factor $\mathcal{R}$ for the overburden, which fit best with the constraining data.
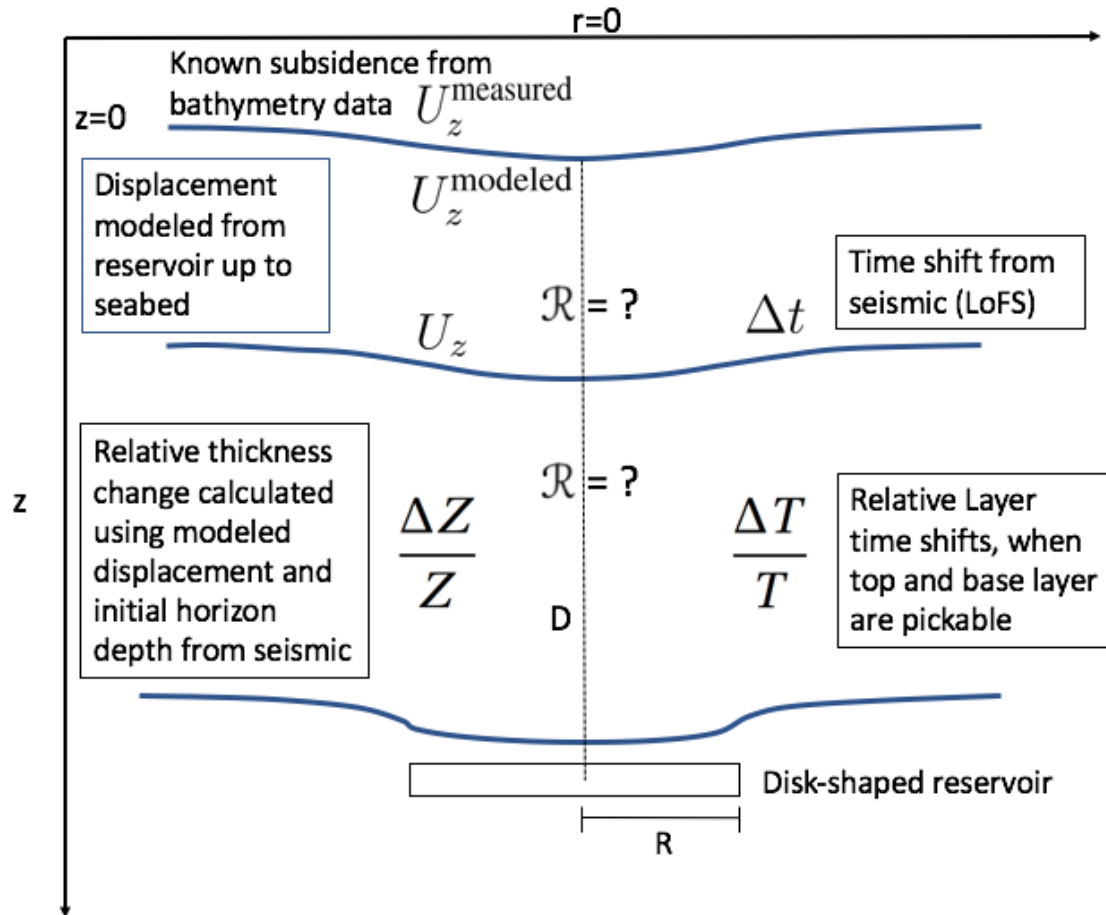
Figure 3.1: Schematic illustration of the inversion problem

Geomechanical modeling is used to estimate the displacement at the same reflectors as the time shifts are extracted from. For then to ultimately best resemble the known subsidence at the seabed. The geomechanical model by Geertsma (1973), mentioned in Ch. 2, is used and function as the first forward operator in the inversion process, Section 3.1.1. The rock physics relation for the $\mathcal{R}$-factor introduced in Ch. 1, together with the equation for relative time shift Eq. 1.2, provide the second forward operator, further explained in Section 3.1.2. Using these two forward operators we can through a global inversion process determine the best reservoir parameters together with the best $\mathcal{R}$-factor values explained further in Section 3.2.

3.1.1 Geertsma's Theory of Subsidence

The result of the first forward operator using the Geertsma equations is a displacement matrix u_z, which is dependent on a series of model parameters, see Eq. 3.1.

$$
m = \begin{bmatrix} D \\ R \\ \Delta p \\ h \\ C_m \\ \nu \\ \alpha \end{bmatrix}
\tag{3.1}
$$

Figure 3.2 shows an example of the calculated displacement on a set of horizons using model parameter values provided by Table C.1. The resulting displacement matrix is calculated using Eq. 2.23, with initiation point $r = 0$, at the center of the reservoir. In Figure 3.2 the dashed rectangle represents the vertical section of the disk-shaped reservoir. Due to the symmetry of the Geertsma equations, the resulting displacement is mirrored for the other side of the reservoir, and for illustration purposes, the displacement has been up-scaled 30 times.
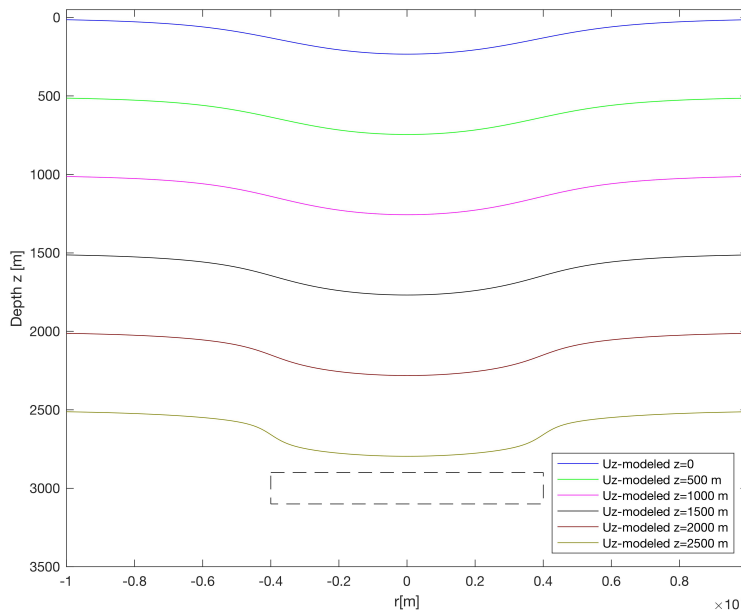
Figure 3.2: Displacement within the overburden every 500 m u_z up-scaled with 30 to visualize the subsidence effect better

The forward model operator g, represented by the Geertsma equations, will calculate the displacement for the whole half space for a set of parameters given by the m-vector Eq. 3.1. Through repeated bathymetry measurements, we can get a qualitative representation of the subsidence at the seafloor, and we can use this as the observed data in the inversion process. Thus Eq. 3.2 show how d_{obs} is represented by the values of u_z at $z = 0$.

$$d_{\text{obs}} = g(m) = u_z|_{z=0} \tag{3.2}$$

From the displacement matrix $u_z(z, r)$, we can get the relative change in thickness by dividing the difference in displacement on the base $u_z(z_{\text{base}}, r)$ and top $u_z(z_{\text{top}}, r)$ of the layer by the corresponding initial layer thickness Z, see Eq. 3.3. The lower-case z letters, $z_{\text{base}}(r)$ and $z_{\text{top}}(r)$ are referring to the depth position of the base and top of the layer.

$$\frac{\Delta Z}{Z} = \frac{(u_z(z_{\text{base}}, r) - u_z(z_{\text{top}}, r)}{(z_{\text{base}}(r) - z_{\text{top}}(r))} \tag{3.3}$$

u_z is calculated in cylindrical coordinates, and due to sign convention, displacement will point in the opposite direction of the coordinate axes, since Geertsma (1973) defined positive z-direction to be downwards, see Figure 2.4. Thus $\frac{\Delta Z}{Z} > 0$ when the overburden is stretched.

3.1.2 $\mathcal{R}$-factor Relation

The second forward model operator uses the rock physics relation from Eq. 1.3 and Eq. 1.2, presented in Ch. 1. If we take the relation from Eq. 1.3, and insert it into Eq. 1.2, we get an expression relating relative two-way traveltime change $\frac{\Delta T}{T}$ and relative thickness change $\frac{\Delta Z}{Z}$ within a layer, see Eq. 3.4.

$$
\begin{aligned}
\frac{\Delta T}{T} &= \frac{\Delta Z}{Z} - \frac{\Delta V_p}{V_p} \\
&= \frac{\Delta Z}{Z} - \left(-\mathcal{R} \cdot \frac{\Delta Z}{Z} \right) \\
\frac{\Delta T}{T} &= \left(1 + \mathcal{R} \right) \frac{\Delta Z}{Z}
\end{aligned}
\tag{3.4}
$$

Where

$$
\frac{\Delta T}{T} = \frac{\left(t_{\text{monitor}} - t_{\text{base}} \right)^{\text{Base of Layer}} - \left(t_{\text{monitor}} - t_{\text{base}} \right)^{\text{Top of Layer}}}{\left((t_{\text{base}})^{\text{Base of Layer}} - (t_{\text{base}})^{\text{Top of Layer}} \right)}
\tag{3.5}
$$

The time strains from Eq. 3.5 indicate that an increase in traveltime, t, in the monitor survey for a reflector, corresponds with positive time shifts for the particular reflector.

3.2 Global Inversion

From the vertical displacement Eq. 2.23 we see that C_m, α, h and Δp_f all are represented outside the Geertsma integrals and are represented as scaling factors of the displacement. Invert of each, and every one of these parameters will not be possible. They can rather be merged into one model parameter K, see Eq. 3.6.

$$
K = \frac{C_m \alpha h \Delta p_f}{2}
\tag{3.6}
$$

The first forward operator will now be given by Eq. 3.7.

$$
u_z = KR\left[\frac{z-D}{|z-D|} I_3 |z-D| - (3-4\nu)I_3(z+D) - 2zI_4(z+D) \right]
\tag{3.7}
$$

Hence the resulting model parameters are presented by the vector in Eq. 3.8. During the inversion process, we invert for the model parameters in the m-vector from Eq. 3.8 while keeping the Poisson's ratio ν fixed at $\nu = 0.2$. Geomechanical studies performed by ConocoPhillips, from

the reservoir unit, have concluded with a relatively constant value of around 0.2 for the porosities present in the reservoir (CoP, 2010). The value of ν will most likely be different in the overburden compared to the reservoir. Since Geertsma's geomechanical model represent a uniformly depleted disk-shaped reservoir, situated within a linear-elastic, homogeneous and isotropic half space. The parameter K in this study resemble the reservoir parameters, and K do not change for the overburden, even though this would be expected in reality both for K and ν since we have different lithologies with different elastic moduli. The model parameter D and R will be global parameters representing the reservoir, while K, hence in reality, is more layer-based than what the inversion process will be able to incorporate.

$$
m = \begin{bmatrix} K \\ D \\ R \end{bmatrix} \tag{3.8}
$$

We use a global inversion process, using every combination of the model parameters within the discretization of K, D, and R, to calculate the displacement matrix, utilizing the forward operator explained in Section 3.1.1. The depth position $z(r)$ where the displacements are calculated, will be the depth converted time picks along the horizons used in the model. The depth information is calculated using an internal velocity model provided by ConocoPhillips.

The known time shifts for the horizons in the model is used to calculate the relative time shifts for the different layers above the reservoir using Eq. 3.5. For then to combine this measured $\frac{\Delta T}{T}_{\text{measured}}$ with every combination of the modeled relative thickness change $\frac{\Delta Z}{Z}_{\text{modeled}}$ to estimate the $\mathcal{R}$-factor for the overburden, see Eq. 3.9.

$$
\mathcal{R}_{\text{modeled}} = \left(\frac{\frac{\Delta T}{T}_{\text{measured}}}{\frac{\Delta Z}{Z}_{\text{modeled}}} \right) - 1 \tag{3.9}
$$

The relative change in thickness $\frac{\Delta Z}{Z}$, from Eq. 3.9, is modeled using the forward operator in Section 3.1.1 and the model parameters from Eq. 3.8. The resulting modeled $\mathcal{R}$-factor will, hence, not be an independent model parameter, but rather depend on the other three model parameters.

Using this modeled $\mathcal{R}$-factor to further estimate a modeled relative time shifts through Eq. 3.10, we can in turn calculate the relative error between $\frac{\Delta T}{T}_{\text{measured}}$ and $\frac{\Delta T}{T}_{\text{modeled}}$.

$$\frac{\Delta T}{T}_{\text{modeled}} = \left(1 + \mathcal{R}_{\text{modeled}}\right)\frac{\Delta Z}{Z}_{\text{modeled}} \tag{3.10}$$

As mentioned in Section 2.4, the best model parameters will be the ones representing u_z and $\frac{\Delta T}{T}$ when the sum of Eq. 3.11 and Eq. 3.12 are minimized. Eq. 3.11 will check the modeled displacement $u_z|_{z=0}^{\text{modeled}}$ at the surface against the measured displacement at the surface $u_z|_{z=0}^{\text{measured}}$ provided by the two bathymetry surveys.

$$\chi_{U_z}^2 = \frac{\sum_i^N \left(u_z^i|_{z=0}^{\text{measured}} - u_z^i|_{z=0}^{\text{modeled}}\right)^2}{\sum_i^N \left(u_z^i|_{z=0}^{\text{measured}}\right)^2} \tag{3.11}$$

$$\chi_{\frac{\Delta t}{t}}^2 = \frac{\sum_i^N \left(\frac{\Delta t}{t}^i_{\text{measured}} - \frac{\Delta t}{t}^i_{\text{modeled}}\right)^2}{\sum_i^N \left(\frac{\Delta t}{t}^i_{\text{measured}}\right)^2} \tag{3.12}$$

Where i is the index number of the elements of $\frac{\Delta T}{T}$ and $u_z|_{z=0}$. N represents the total number of discretization of r on the $u_z|_{z=0}$ vector for $\chi_{U_z}^2$. While for $\chi_{\frac{\Delta t}{t}}^2$, N will be the total number of discretization of r on the $u_z|_{z=0}$ vector multiplied by the total number of discretization of z (rows). The number of indices N must be the same for $\frac{\Delta T}{T}$ and $\frac{\Delta Z}{Z}$ since these matrices are both used together in the estimation of the $\mathcal{R}$-factor in Eq. 3.9.

Eq. 3.13 represents the objective function used in the inversion process, that is minimized. Here c is a weighting term that can be used to balance the influence from the two terms. In this study $c = 1$. The displacement at the seafloor will be the dominating element of the resulting objective function value. The measured relative time shifts are used together with the modeled relative thickness change to calculate the $\mathcal{R}$-factor. The modeled relative time shifts calculated using this $\mathcal{R}$-factor will, therefore, be almost identical, and the dominating element of the error function will further be the displacement term, $\chi_{U_z}^2$.

$$\Phi = \chi^2_{U_z} + c \cdot \chi^2_{\frac{\Delta t}{t}} \tag{3.13}$$

Every value of Φ is stored in a resulting relative error matrix ϵ, see Eq. 3.14. Each element of the ϵ-matrix is checked against each other, and only the element with the lowest value is kept as the new value to beat when comparing to a new set of values for the model parameter vector Eq. 3.8.

$$\epsilon = \epsilon_{(K,D,R)} \tag{3.14}$$

The corresponding model parameters with the lowest objective function value, will be the resulting best-fit model parameters given by m_{Best}-vector Eq. 3.15.

$$m_{\text{Best}} = \begin{bmatrix} K_{\text{Best}} \\ D_{\text{Best}} \\ R_{\text{Best}} \end{bmatrix} \tag{3.15}$$

When the best model parameters from Eq. 3.15 are determined, the modeled $\frac{\Delta Z}{Z}$ and $\frac{\Delta T}{T}$ matrices produce the $\mathcal{R}$-factor as the last biased model parameter. With matrix size equal to the calculated $\frac{\Delta Z}{Z}$ and $\frac{\Delta T}{T}$ matrices.

Chapter 4

Data Sources and Preparation

4.1 Time-Lapse Seismic Data

Two full-offset stack 3D seismic cubes were available from the Ekofisk Field's Life of Field Seismic installation, presented in Ch. 2. LoFS 2 was acquired in 2011, and LoFS 8 was acquired in 2014. The geometry of the surveys are listed in Table 4.1 and shown in Figure 4.1. Where X- and Y-positions are given in meters.

Description	Value
Origin X	519872.08
Origin Y	6260078.94
End first inline X	516586.81
End first inline Y	6273777.78
End first crossline X	511194.31
End first crossline Y	6257996.95
Inline spacing [m]	12.5
Crossline spacing [m]	12.5
Length of Inline [m]	14087.5
Length of Crossline [m]	8925.01

Table 4.1: Geometry settings for the full-offset stack seismic cubes L02 and L08
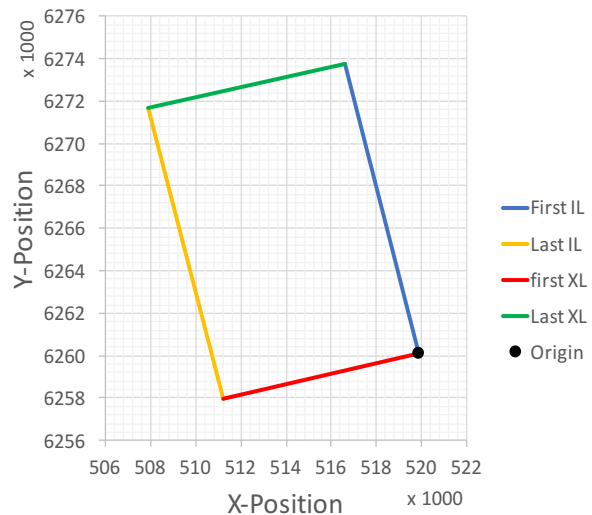
Figure 4.1: Geometry of full-offset stack 3D seismic cube

A time shift cube between LoFS 2-8 was also available. Where LoFS 8 is the monitor survey, and LoFS 2 is the base survey. A positive time shift correspond with an increase in traveltime in the monitor survey, see Eq. 4.1.

$$\Delta t = t_{\text{monitor}} - t_{\text{base}} \tag{4.1}$$

Figure 4.2 shows the extracted time shifts on the structured top Ekofisk formation, representing the top reservoir surface. The extracted time shifts show a complex image of positive and negative time shifts. For a compacting reservoir, we would intuitively expect only positive time shifts on the top reservoir horizon. The overburden above a compacting reservoir is stretched, causing an increase in thickness, and decrease in velocity in the monitor case, which should be detected as a positive time shift. This is not the case across the top reservoir surface in Figure 4.2.
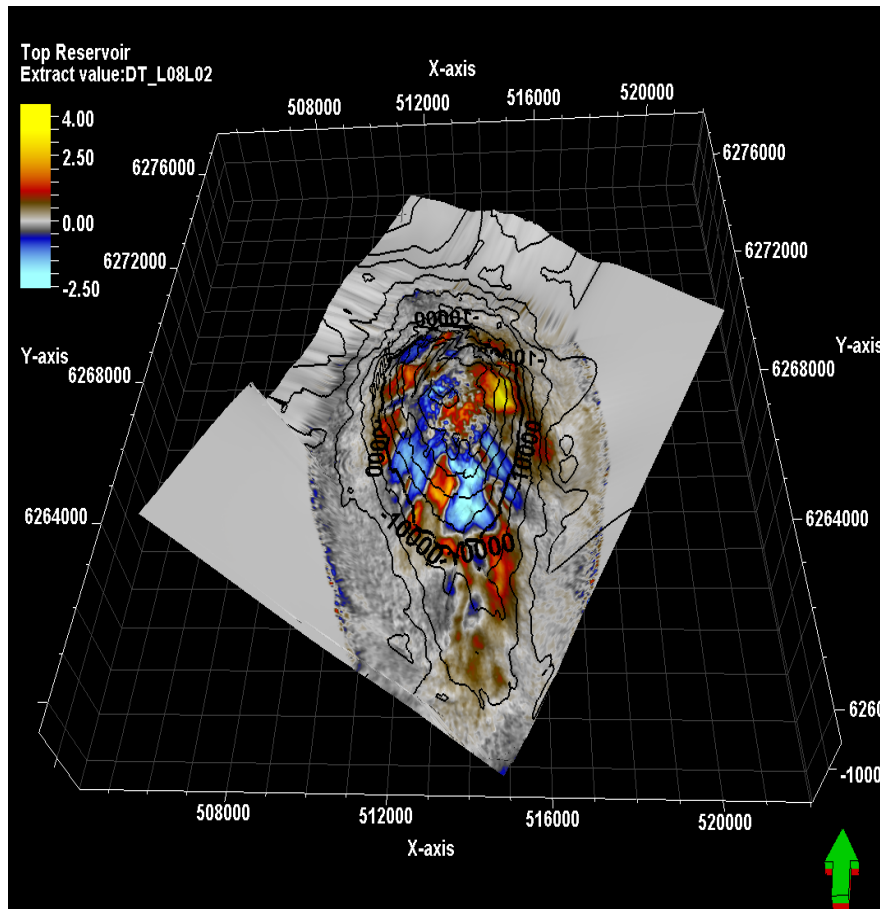
Figure 4.2: Time shift values overlaid structured top reservoir surface (contour increment of 100 ft), time shift values in ms and coordinate axis are in meters

Within the reservoir zone, ConocoPhillips has interpreted numerous faults which some also cut through the top reservoir. Figure 4.3 show a zoomed image of the time shift map from Figure 4.2, with the fault locations represented by blue lines. The heterogeneity of the chalk reservoir becomes clear when we see this dense fault network.
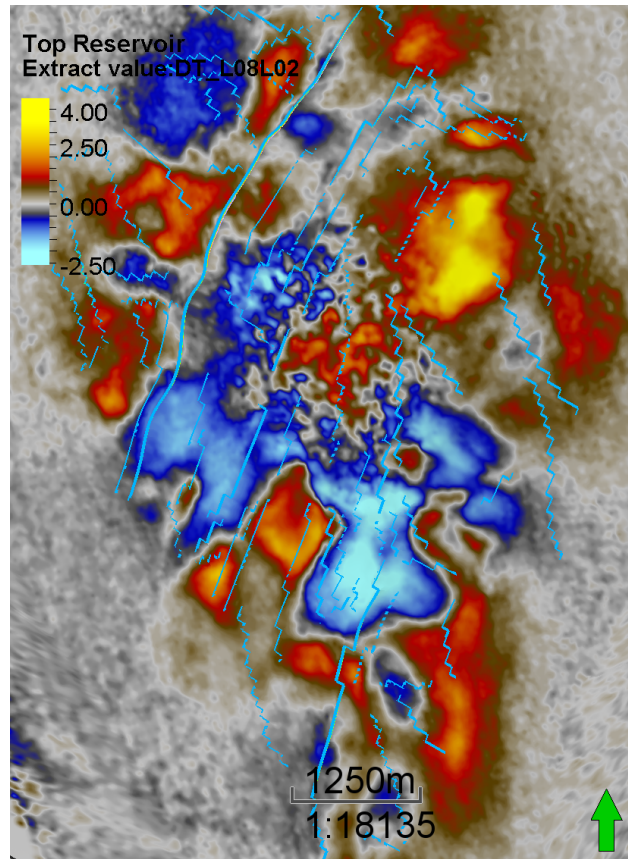
Figure 4.3: Zoomed top reservoir time shift map from Figure 4.2, fault locations represented by blue lines

The time shift effects we see from the reservoir level affect the layers in the overburden. Figure 4.4 shows time shift slices from the reservoir level at 10500 ft (3200 m) up to near seabed. Highlighted is one area where we throughout the overburden see continuously positive time shifts. The geomechanical model presented in Ch. 2 is built upon the simplified assumption that the reservoir is uniformly depleted, resulting in strictly positive time shifts in the overburden. The area highlighted is, therefore, an area where our inversion model could potentially be used. The negative time shifts observed at top reservoir are also present in the overburden with decreasing anomaly, as we see for the highlighted area of positive time shifts.
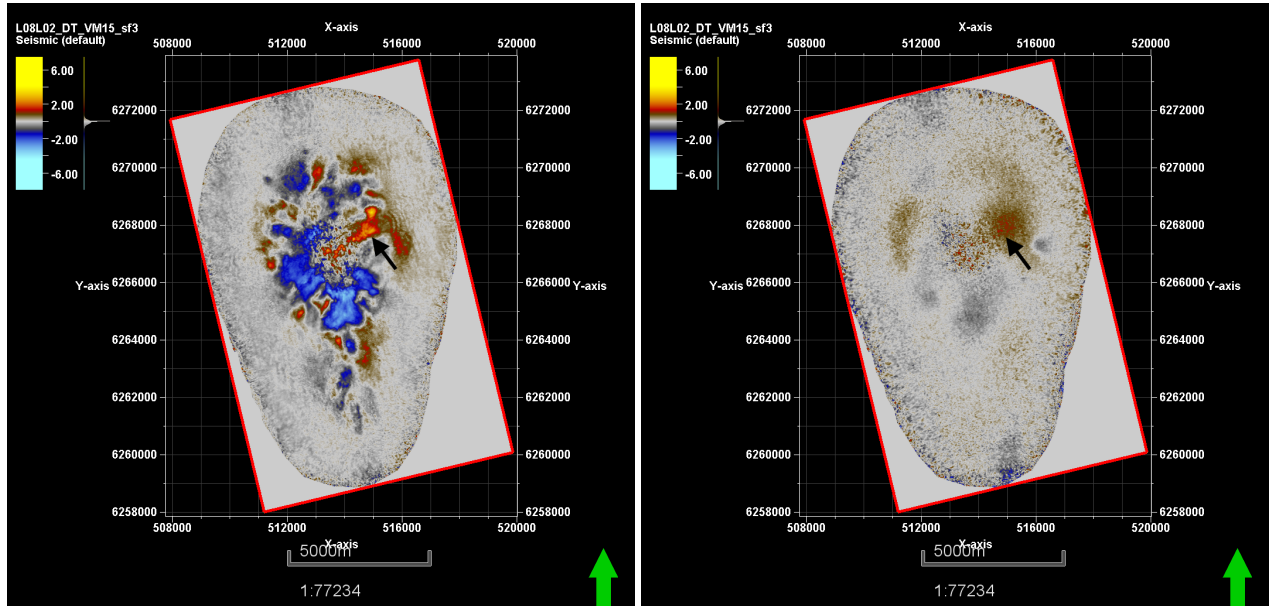
(a) Time shift slice at depth≈ 3200 m (10500 ft)

(b) Time shift slice at depth≈ 1700 m (5500 ft)
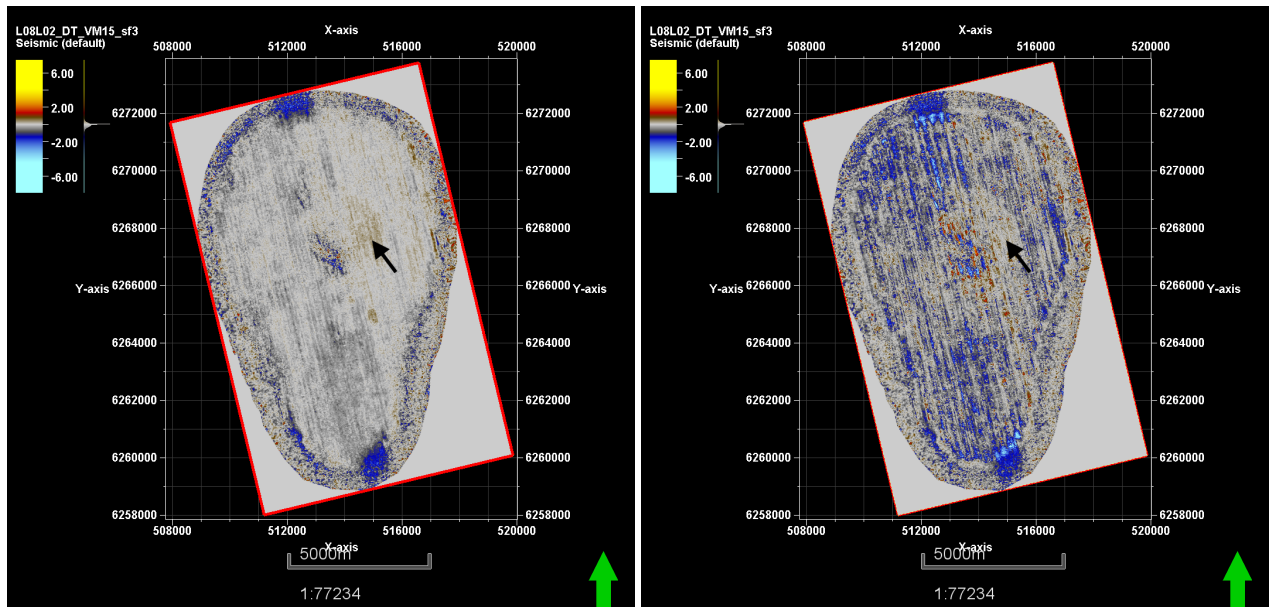
(c) Time shift slice at depth≈ 500 m (1500 ft)

(d) First time shift sample at depth≈ 3 m (9.37 ft)

Figure 4.4: Time shift slices from reservoir level up to near seabed, arrow pointing towards an area with mostly positive time shifts up towards the surface

4.2 Pressure Data

The driving mechanism of subsidence is the changes we inflict the reservoir by producing or injecting fluids. Pressure maps were made available by ConocoPhillips for the full reservoir from 2011 and 2014. These maps have been produced from reservoir simulation based on pressure measurements from wells.
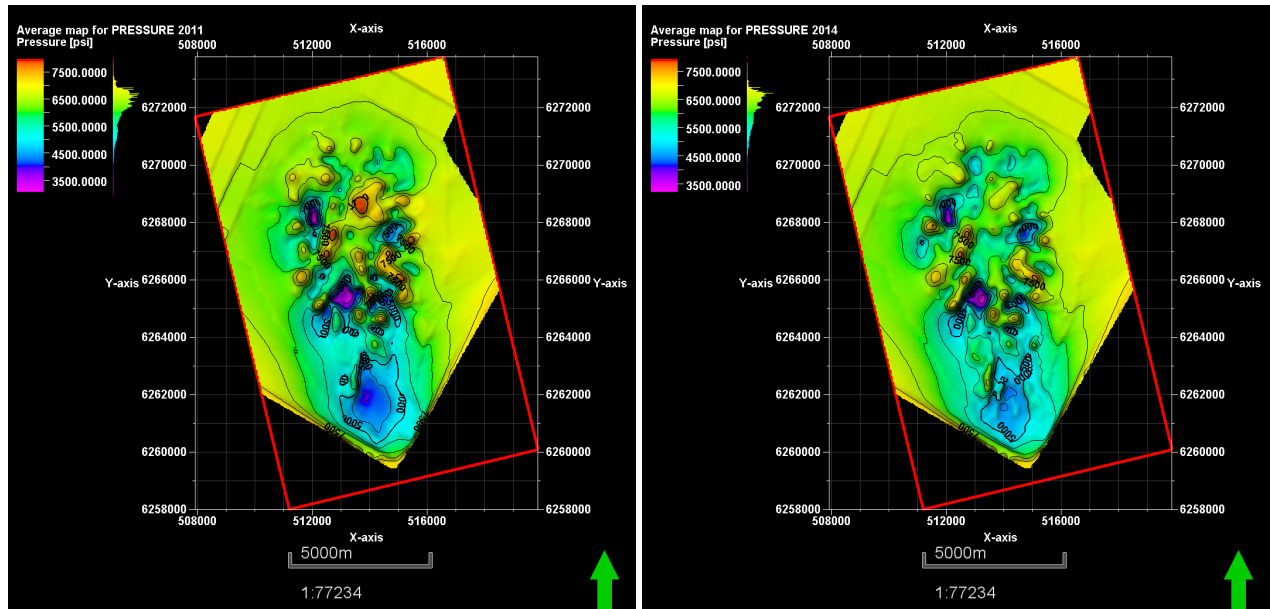
(a) Average reservoir pore pressure 2011   (b) Average reservoir pore pressure 2014

Figure 4.5: Average reservoir pore pressure map calculated over all reservoir zones for 2011 and 2014

The map is an average map calculated across all the reservoir zones for 2011 (Figure 4.5a) and 2014 (Figure 4.5b). The calculation has been performed using Petrels internal average map function. Figure 4.6 show the resulting change in pore pressure between 2014 and 2011. Taking $\Delta p_f = P_{2014} - P_{2011}$. The geomechanical model presented in Ch. 2, based on the superposition of depleting spheres, implies that in theory the method should be utilized on a uniformly depleted reservoir. There are very few reservoirs that are uniformly depleted; the real picture is more like Figure 4.6.
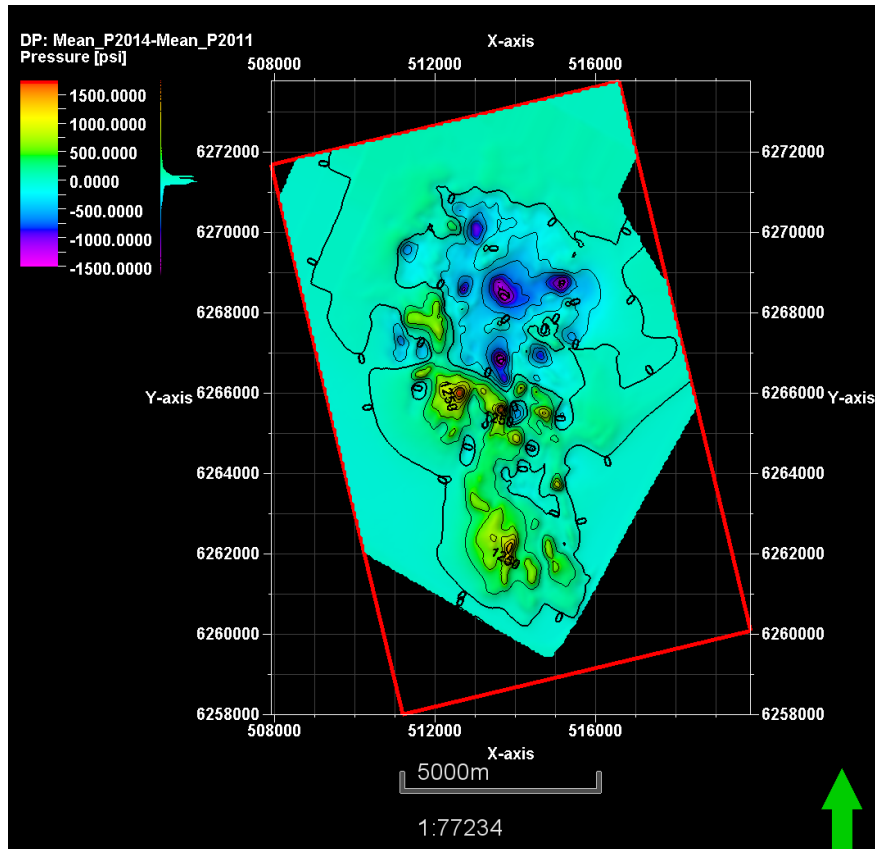
Figure 4.6: Change in average reservoir pore pressure from 2011-2014

The resulting Δp_f-map does not show a uniform depletion of the reservoir, but rather a complex picture of average pore pressure increase and reduction. With Ekofisk's production history, with a complex map of injectors and producers, this is what to expect. A zoomed image of the reservoir pore pressure differences is shown in Figure 4.7, where each contour line represents a change in 250 psi. The outer bold contour represents $\Delta p_f = 0$, as was labeled in Figure 4.6. Roughly we can say that between 2011 and 2014 there is one northeastern zone of average pressure decrease and one southwestern zone of on average pressure increase.
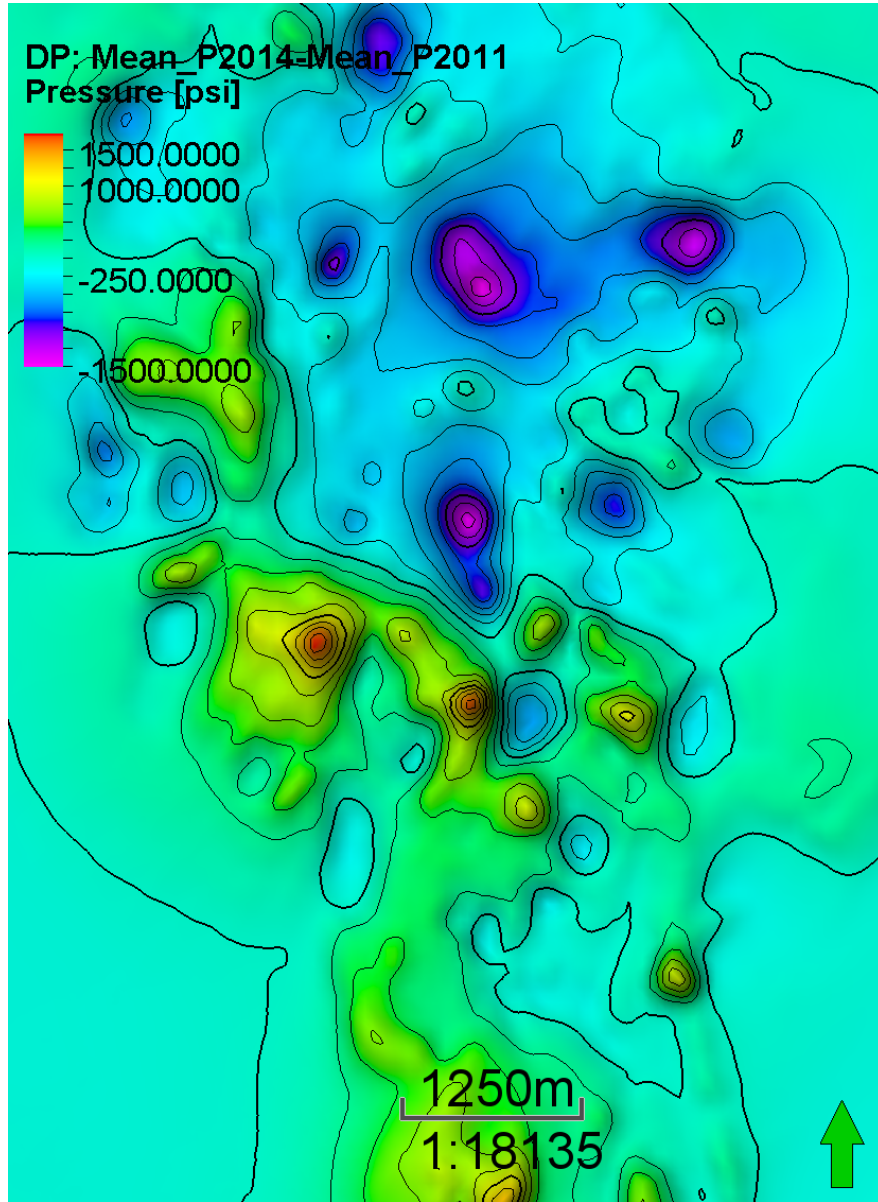
Figure 4.7: Zoomed Δp_f-map [psi], bold contour furthest out represent $\Delta p_f = 0$ and contour levels are 250 psi

4.3   Bathymetry Data

The two maps shown in Figure 4.8 represent the bathymetry surveys from 2011 (Figure 4.8a) and 2014 (Figure 4.8b), representing depth measurements of the seafloor. The 2014 survey was cut short compared to plans due to bad weather, and for that reason, the survey lines did not cover the entire subsidence area. The 2011 survey is more widespread than the 2014 survey, so the 2011 survey has been cropped outside the extent of the 2014 survey. The difference between these two datasets can give us information regarding the level of subsidence between 2011 and 2014. Figure 4.9 shows the calculation of the first pass displacement at the seafloor, measurements given in feet.
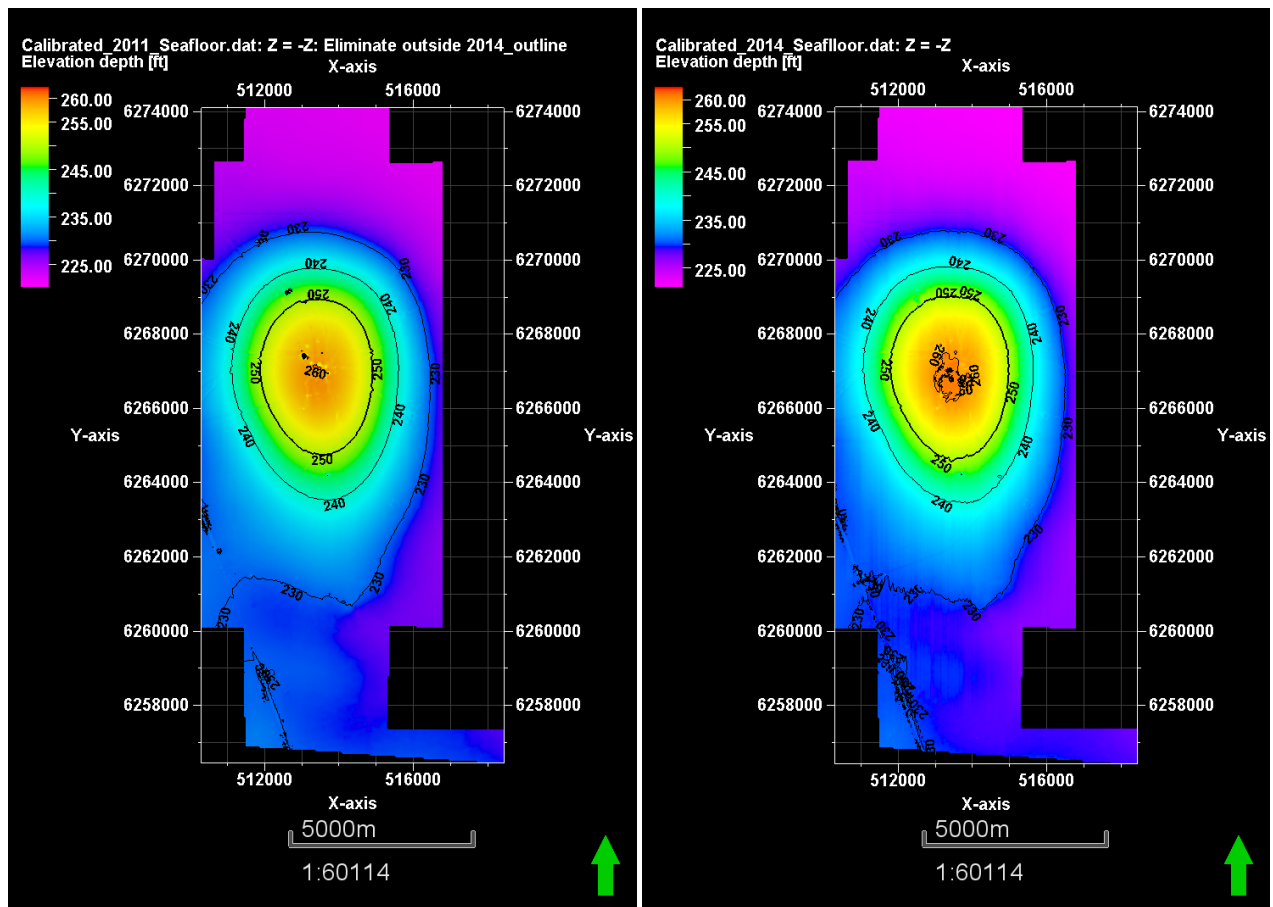
(a) Bathymetry survey 2011   (b) Bathymetry survey 2014

Figure 4.8: Original bathymetry surveys from 2011 and 2014, bathymetry survey from 2011 is cropped outside the outline of bathymetry survey 2014 (contours of 10 ft)
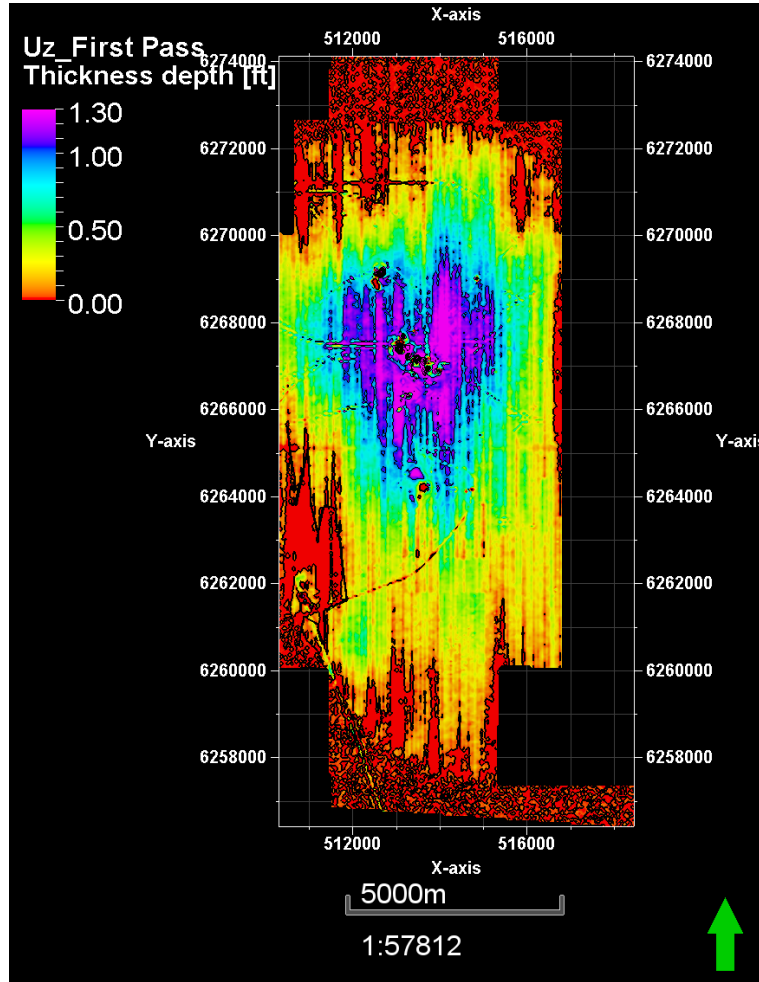
Figure 4.9: First pass displacement map at the seabed [ft]

The two bathymetry maps have been generated with a different sampling rate, making the details unevenly resolved on the two bathymetry maps. The X-and Y-increments on the 2011 bathymetry map has been produced with 10 m spacing, while the 2014 bathymetry map has an X-and Y-increments of 50 m.

The inversion algorithm presented in Ch. 3 uses the subsidence at the seabed as constraining data. The displacement calculated using this geomechanical model will be a smooth curve with increasing subsidence as we approach the center of the subsidence bowl. Due to the irregular first pass displacement map, shown in Figure 4.9, and the fact that we have different spacing between the data points in the two bathymetry maps, we need to smooth the input bathymetry maps, to create a displacement map closer to what will be calculated using the geomechanical model. The two

45

bathymetry maps have been smoothed using four iterations of Petrels internal Gaussian smoothing operator taking the five neighboring points as filter influence width. This operator removes random noise and spikes and works as a low-pass filter.

Figure 4.10 shows the resulting smoothed bathymetry maps, which has been further cropped outside the outline of the 3D seismic cube. We do not have any seismic data outside of this area, so information beyond this outline will be irrelevant and not used in the study.
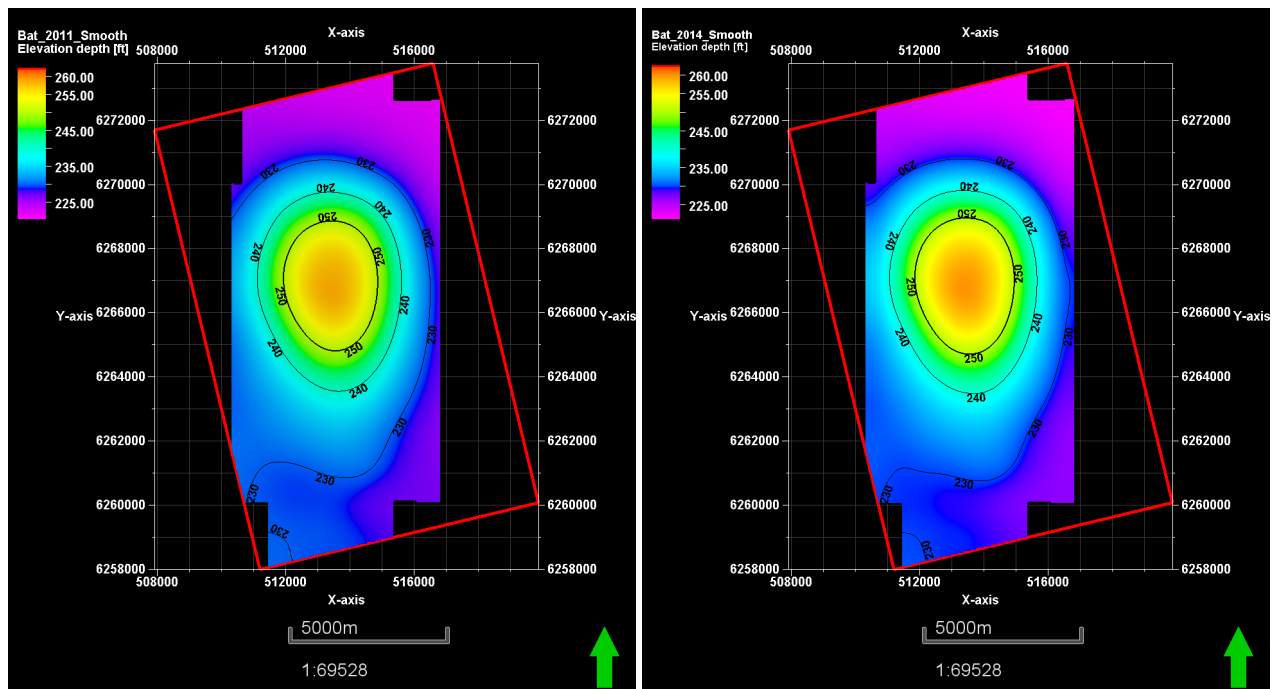
(a) Smoothed bathymetry survey 2011   (b) Smoothed bathymetry survey 2014

Figure 4.10: Bathymetry surveys smoothed with 4 iterations of Petrels builtin gaussian smooth function using 5 neighbouring points. Maps cropped outside 3D seismic survey outline (red)

The resulting displacement between these two vintages has been calculated using Petrels internal thickness operator. Since the two datasets have different spacing, this is the best approach. The resulting displacement map is shown in Figure 4.11a. We can see the procedure resulted in some edge effects with increasing displacement, where we would expect a reduction in displacement. These values have been cropped out along with small amount of negative values. Before running the same smoothing procedure, 4 iterations and filter width of 5, as for the bathymetry surveys.
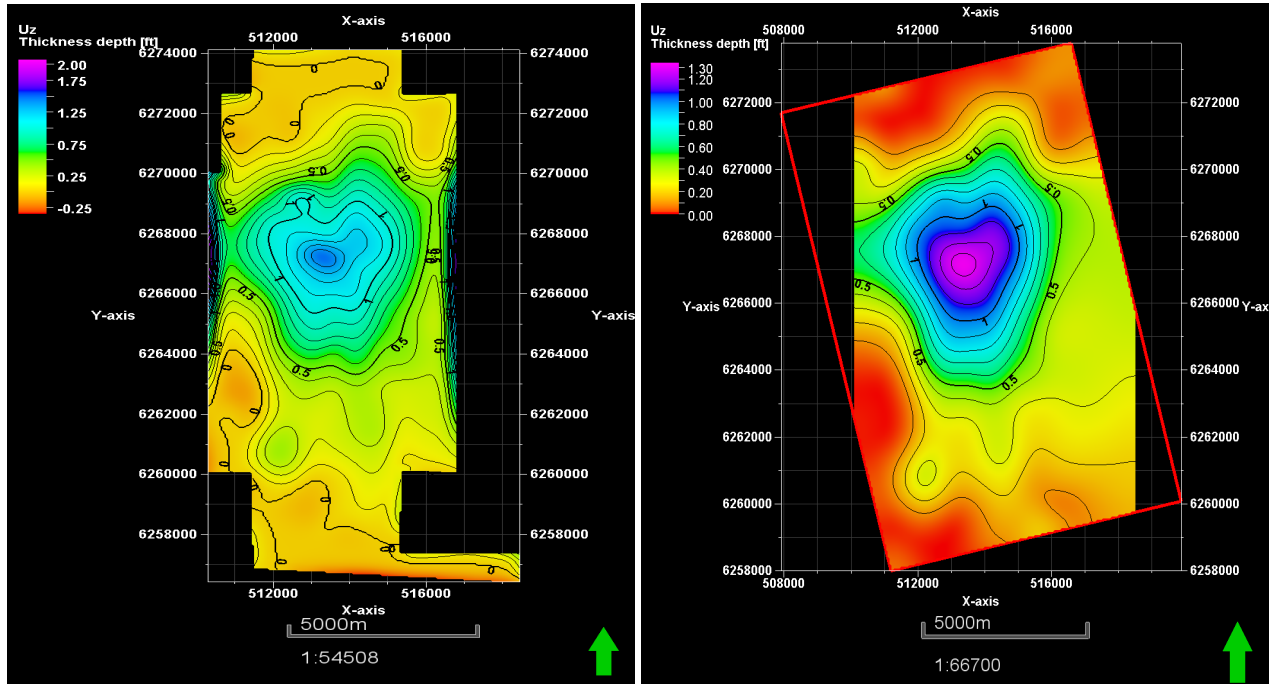
(a) Resulting seabed displacement map between 2011 and 2014 bathymetry map

(b) Smoothed and extrapolated seabed displacement map and removed measurements outside 3D survey

Figure 4.11: Process of creating the resulting displacement map between 2011 and 2014
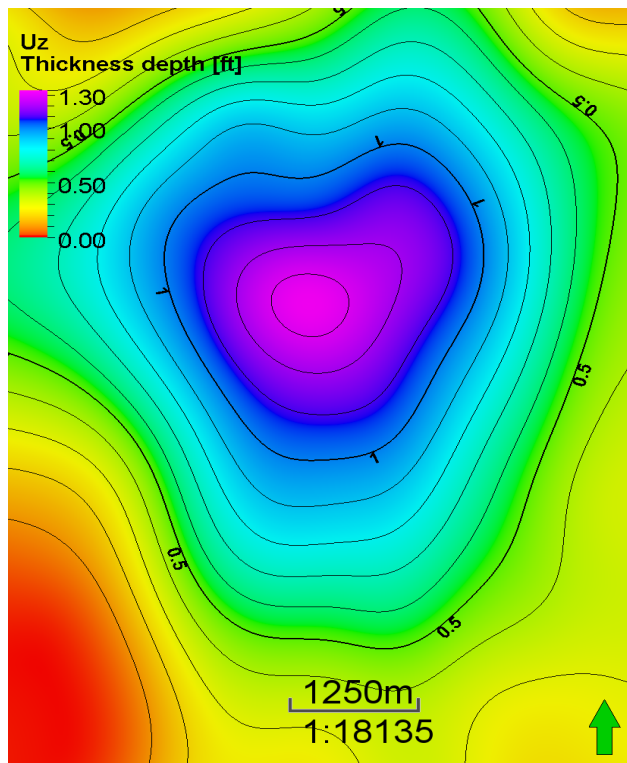
Figure 4.12: Zoomed image of the subsidence bowl from Figure 4.11b

The resulting survey has further been cropped outside the 3D seismic outline, and since we know that the subsidence effect will approach zero when moving further away from the center of the subsidence bowl, Petrel's minimum curvature extrapolation method has been used up towards the edges of the 3D seismic cube. Which is an extrapolation method supposed to maintain the trends within the dataset. The final displacement map is shown in Figure 4.11b, and a zoomed image of the subsidence bowl is shown in Figure 4.12, with contour levels of 0.1 feet.

A zoomed image of the time-lapse differences presented in these previous three Sections 4.1-4.3, are shown in Figure 4.13. The contours from the displacement plot (Figure 4.13a) are overlaid on the reservoir pore pressure map (Figure 4.13c) and on the top reservoir time shift map (Figure 4.13b), to better show and compare the locations and interaction between the effects. As mentioned in Ch. 2, reservoir pressures affect the seismic data responses. The average pressure decrease is causing effective stress to increase, causing velocity to increase and the reservoir to ultimately compact. The speed up within the reservoir will most commonly cause a slowdown in the overburden due to positive strain and, hence, positive time shifts. The area which was highlighted on the time shift slices on Figure 4.4 from the overburden is the same area where we see on average pore pressure reduction (purple area), in Figure 4.6. This connection is easier to see on the zoomed images from Figure 4.13c and Figure 4.13b. We can also notice that the area of average pressure increase also coincides with the area of mostly negative time shifts which propagate up into the overburden. The figure also shows the geometry of the reservoir. It is not a simple disk-shaped reservoir as the method presented in Ch. 3 is built upon. To make the process work, it will be necessary to approximate an area of the reservoir as a disk and focus the inversion process in this area.

(a) u_z [ft]

(b) Δt [ms], Contours [ft]

(c) Δp_f [Psi], Contours [ft]
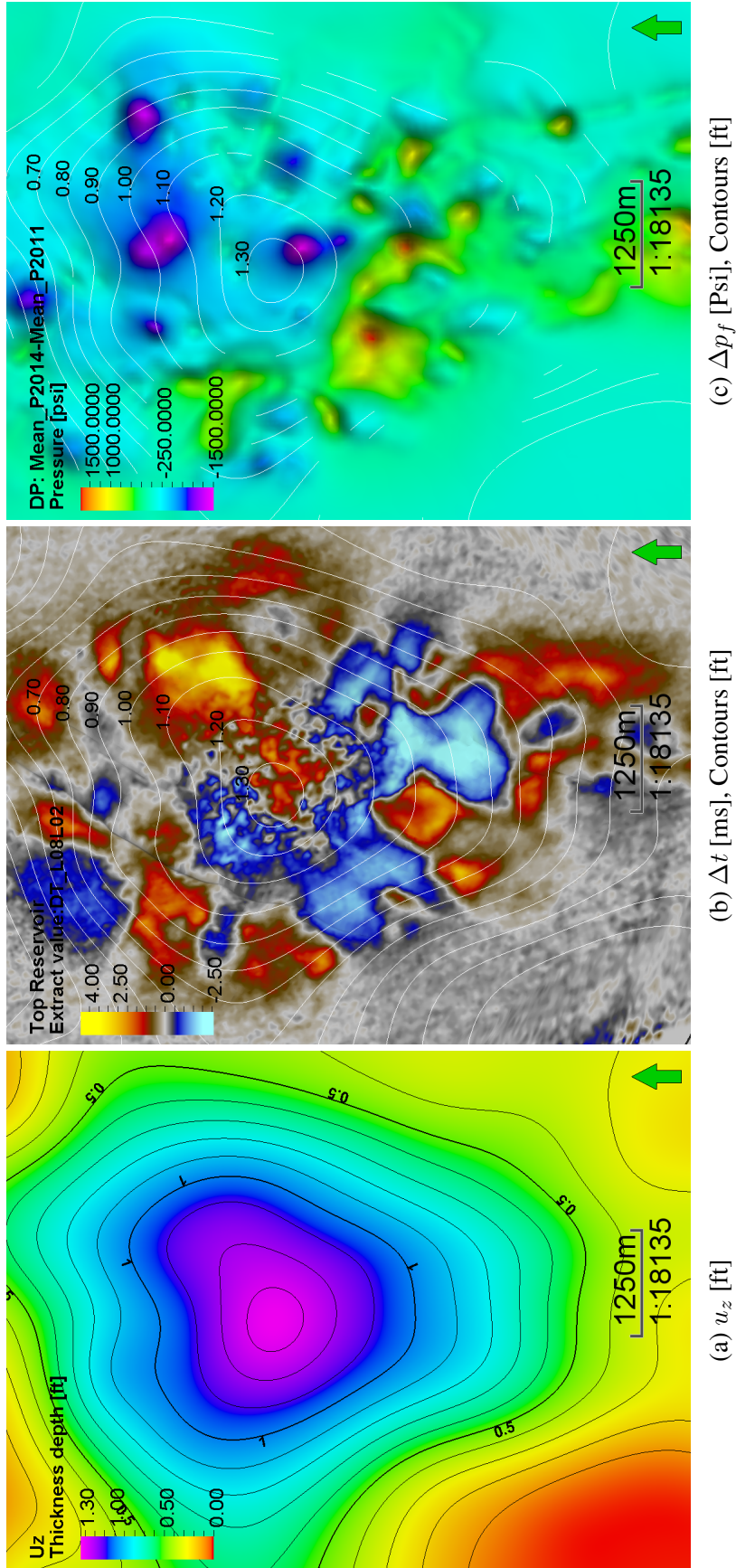
Figure 4.13: Seabed displacement (a) with contour lines overlaid both on top reservoir time shift map (b) and reservoir pore pressure difference map (c)

49

4.4   Data Selection for Inversion

The theory behind the displacement above a disk-shaped reservoir is based on symmetry, as presented in Ch. 2. The resulting displacement calculation represents a vertical section above the reservoir, from the center of the subsidence bowl (CSB) and out. This resulting displacement with radial position from the center will represent every point with the same radial position and same depth in a 3-dimensional space. The geomechanical model will produce a smooth result for the displacement above the disk-shaped reservoir. Therefore we need to pick a representative 2D seismic line running through the CSB and collect data from one side of the center of the subsidence bowl. The data collected need to be in SI-units, hence depth measurements need to be converted from feet (ft) to meters (m), and extracted pressure measurements from Pounds per square inch (Psi) to Pascal (Pa).

To be able to use seismic data alongside this model, we need the time shifts fluctuation to be at a minimum, and rather follow the same trend as the displacement produced by the geomechanical model. Implying increasing positive time shifts with increasing depth, and decreasing time shifts with increasing radial position from the center of the subsidence bowl.

Figure 4.14a show three 2D seismic lines running through the center of the subsidence bowl, which is represented by the crossing point of these three seismic lines. The same three 2D seismic lines are shown on the pressure map (Figure 4.14b) from Section 4.2, and on the time shift map (Figure 4.14c) presented in Section 4.1.

At the end of Section 4.3, it was pointed out that the area of depletion, represented by "cold" colors, correspond with the area of positive time shift. Figure 4.14 show the same maps together with the position of the potential input seismic lines. From the center of the subsidence bowl (the crossing point) and to the northeastern half of the seismic lines, the seismic lines are within the depleted zone (Figure 4.14b), and with corresponding positive time shifts (Figure 4.14c). These parts of the seismic lines could all be possible input lines for the inversion process.
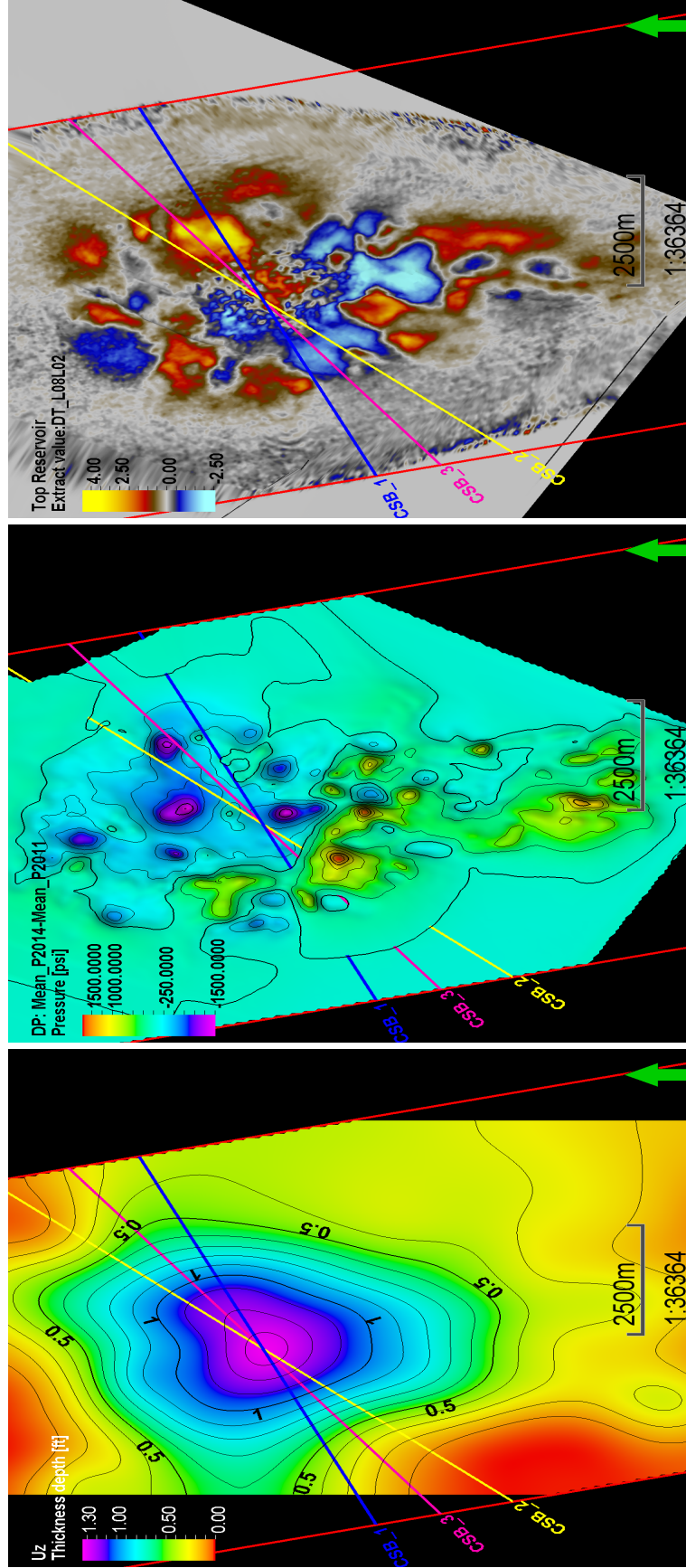
(a) Displacement map, CSB represented by the crossing point of the seismic lines

(b) Average reservoir Δp_f-map. NE-part show on average pressure reduction

(c) Δt-map from top reservoir. NE-part show positive time shifts

Figure 4.14: Three potential input 2D seismic lines going through the center of the subsidence bowl (CSB) and shown on top of average reservoir pressure map and top reservoir time shift map

Geertsma (1973) built his model upon superposition of depleting spheres, which in practice bounds the reservoir to experience uniform depletion. Figure 4.15 show the extracted Δp_f along each of these three 2D seismic lines. The positioning system along these lines run from 0 in SW adding the spacing between data points correspond with the in-line and cross-line spacing of the data, see Table 4.1. One calculated example of the positioning system is further explained in Section 4.4.1 below.

(a) Δp_f extracted along CSB Line 1

(b) Δp_f extracted along CSB Line 2

(c) Δp_f extracted along CSB Line 3
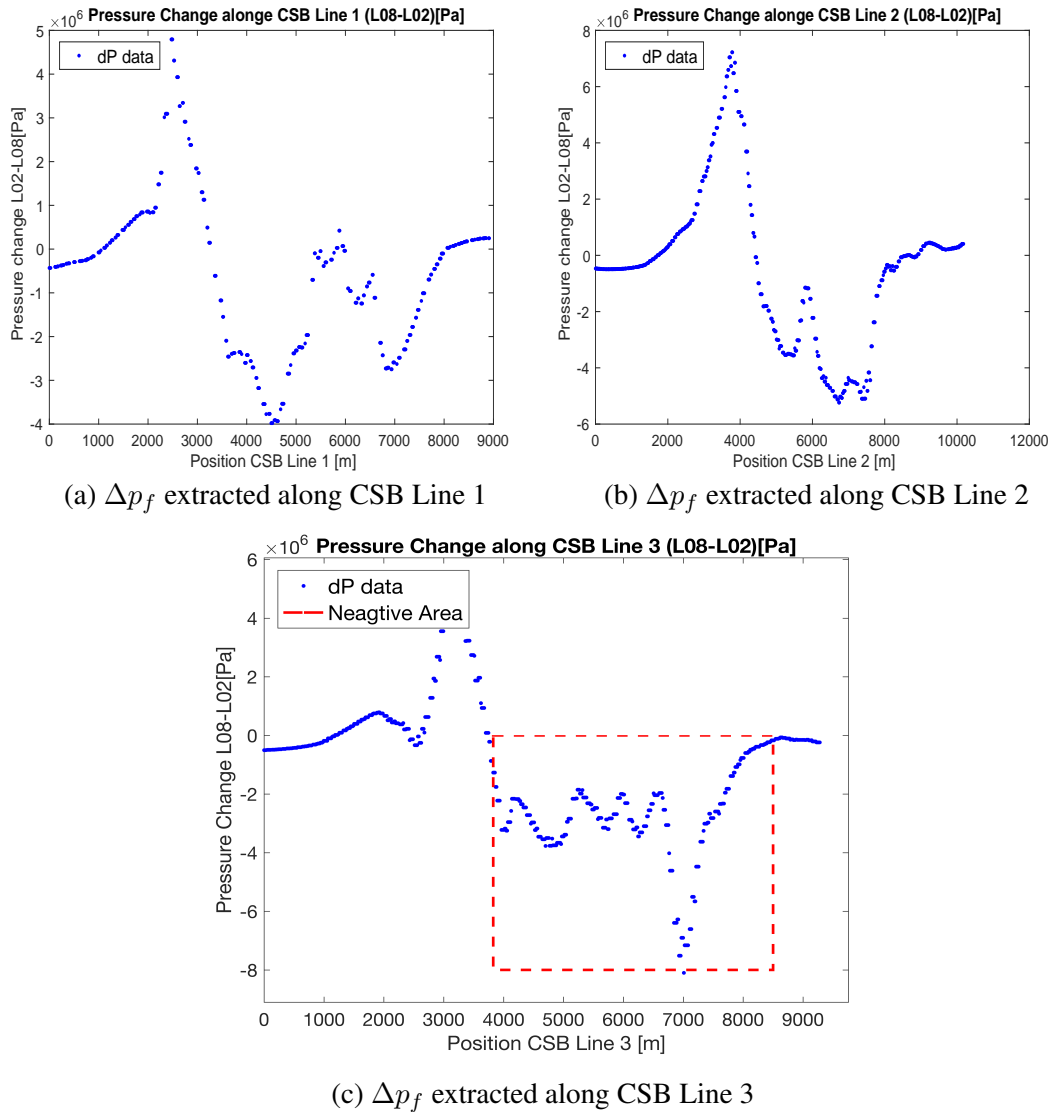
Figure 4.15: Change in reservoir pore pressure extracted from the Δp_f-map shown in Figure 4.14b along 3 2D seismic lines

The depleted section on CSB Line 3, marked by the red box on Figure 4.15c, show the most stable depleted zone compared to the other two seismic lines and will closer represent the uniform

pressure depletion setting. That is why we further look into the seismic data along CSB Line 3 as input data.

4.4.1 Input: Time-Lapse Seismic Data

The geometry of the seismic line (CSB Line 3) chosen as potential input for the inversion process, is shown in Figure 4.16. From Table 4.2, we can see the total length of the seismic line equal 9758 m. This can also be shown using simply the Pythagoras theorem. Since we know the maximum and minimum X- and Y- position, which is given by 1 m spacing, we can calculate the total length using Eq. 4.2.

Description	Value
X min	519872.08
X max	6260078.94
Y min	516586.81
Y max	6273777.78
Number of Traces	715
Spacing [m]	≈ 13.64
Length of CSB Line [m]	9758

Table 4.2: Geometry settings for input seismic line, seismic cubes L02 and L08
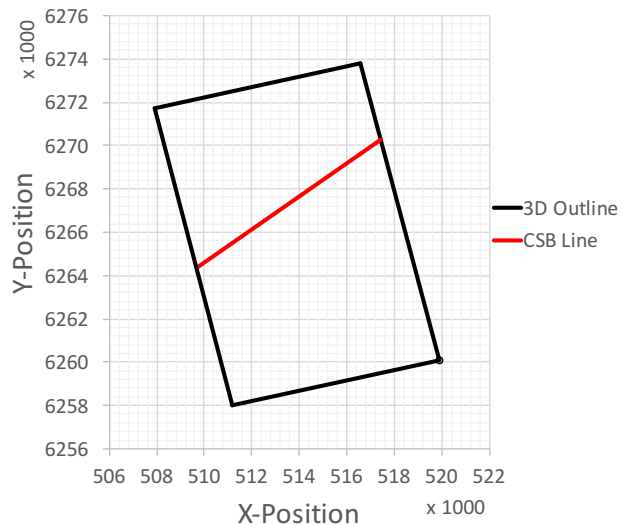
Figure 4.16: Geometry of CSB Line 3 within the 3D Seismic Cube

$$Length = \sqrt{(X_{\max} - X_{\min})^2 + (Y_{\max} - Y_{\min})^2} \tag{4.2}$$

We have 715 traces along this arbitrary line resulting in a time pick spacing of $\frac{length}{\#traces} \approx 13.64$. Due to small differences in rounding error between the data points this spacing may vary slightly for the last digit. The position along the arbitrary line will be the summation of the spacing between the time picks, referred to the origin of the seismic line $(X_{\min}, Y_{\min})$. This is an attempt to simplify, instead of referring to an X- and Y-coordinate for each time pick.

4.4.2 Input: Bathymetry Data

(a) Displacements extracted along CSB Line 3

(b) Location of CSB Line 3 on displacement map
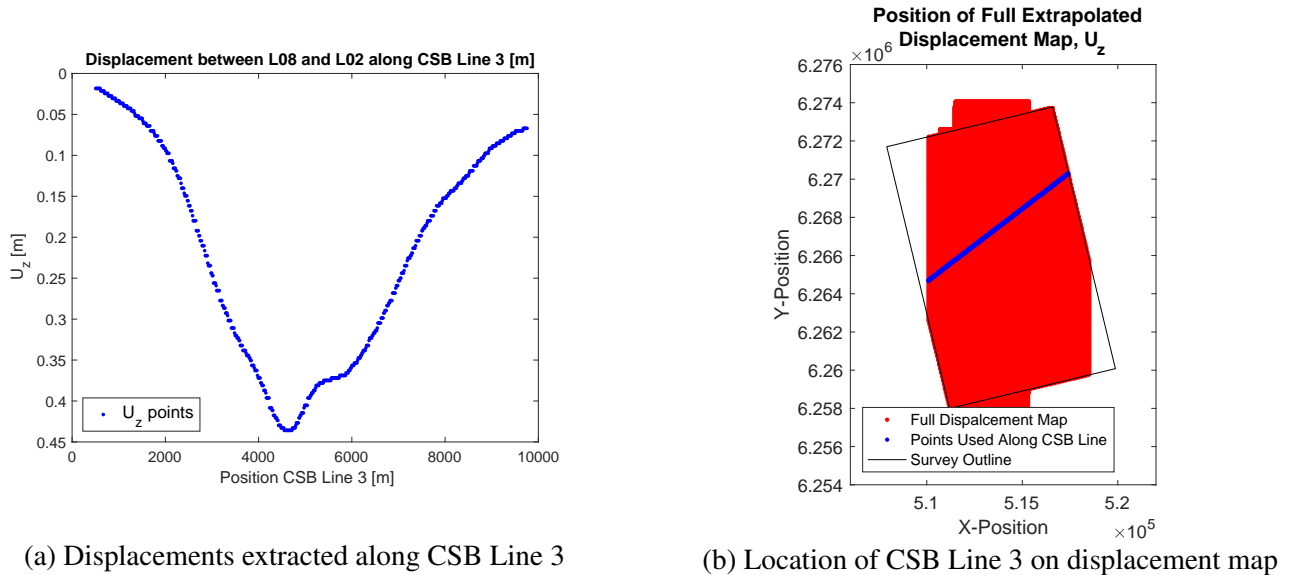
Figure 4.17: Input displacement extracted along CSB Line 3

The displacement measurements extracted along CSB Line 3 from the final displacement map are shown in Figure 4.17. The spacing of the seismic line shown in Table 4.2 compared to the increment of 50 m in X- and Y-direction from the final displacement map, results in a mismatch between the data points from the displacement map and the seismic, see Figure 4.18a. The resulting displacement measurements used are the points which are closest to the seismic data points, see Figure 4.18b. These are the displacement points on the NE side of the center of the subsidence bowl. Corresponding with pressure reduction from Figure 4.14b and positive time shifts from Figure 4.14c. These are not as densely spaced as the seismic data. Therefore, the final input data has been linearly interpolated between the measured displacement points, to make the input measurements of equal vector length. The final input displacement measurements are plotted in Figure 4.18d. This figure also introduces a new position system; the radial position from the center of the subsidence bowl. The largest displacement at the seabed will be at position $r = 0$. The difference between the interpolated displacement points and the measured displacement points are shown in Figure 4.18c. We can see that the data trend is kept through the interpolation process.

(a) Position of seismic data points for CSB line 3 vs displacement data points

(b) Displacement points from the center of the subsidence bowl with increasing position

(c) Interpolated (red) vs measured displacement points

(d) Final input displacement points from $r = 0$
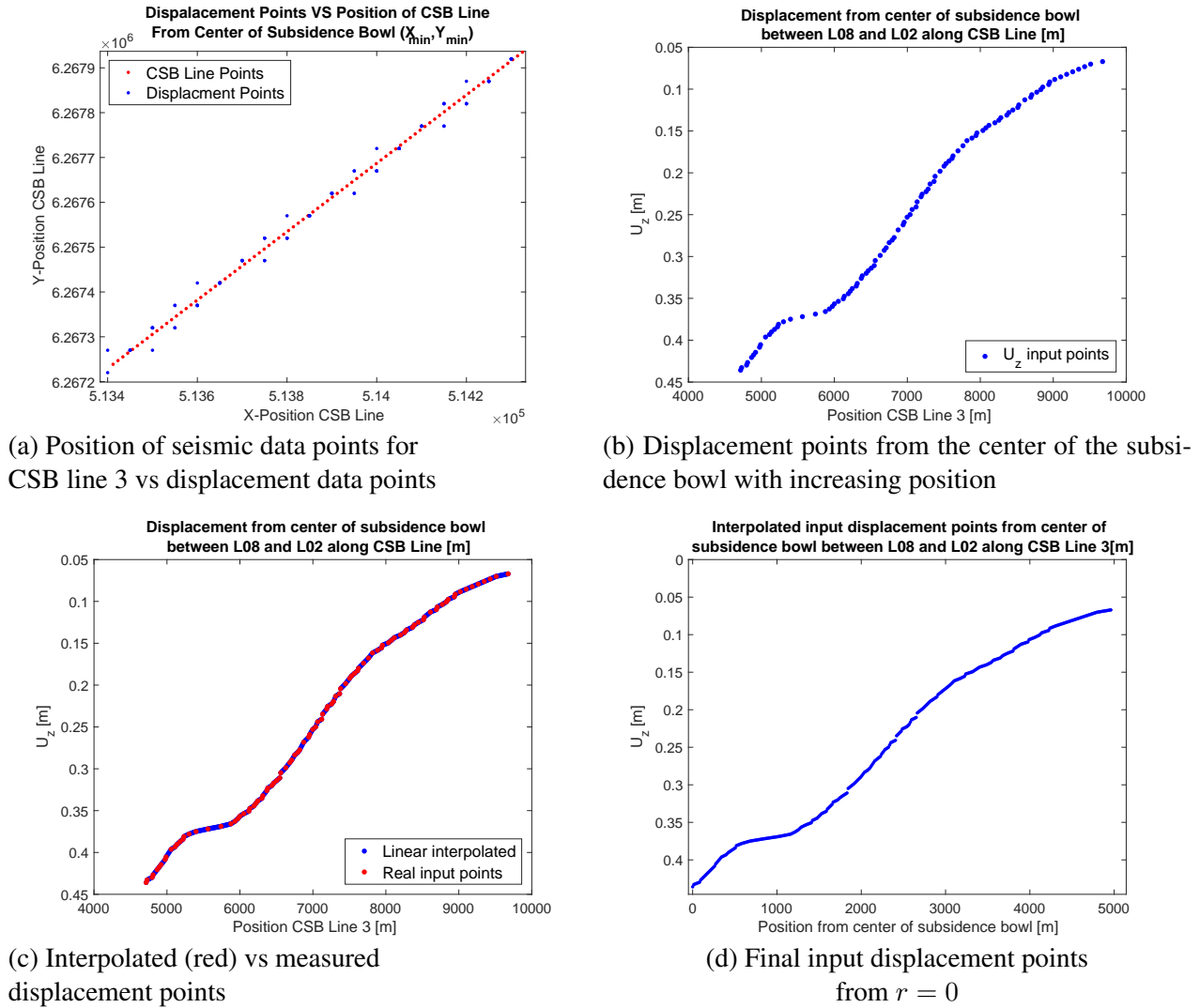
Figure 4.18: Process of choosing the representative displacement points along CSB Line 3

4.4.3 Expected Model Parameters

The inversion process does not use the pressure data as input, but rather to give an indicator of the model space for the model parameter K. As mentioned in Section 3.2 the factor K depend on α, h, C_m and Δp_f. The Biot coefficient α for chalk is approximate 1 and the reservoir thickness is in the order of 300 m as mentioned in Ch. 2. The compaction coefficient for the Ekofisk chalk reservoir has been estimated to around $C_m = 2.1 \cdot 10^{-9}$ Pa, using an average porosity of $\bar{\phi} = 37.5\%$. The estimate is calculated from internal data provided by ConocoPhillips (Narongsirikul, Sirikarn, 2017). The last factor needed to represent the factor K is the pressure change. The average pressure

change from the center of the subsidence bowl until the position of no pressure change is posted in the header of Figure 4.19.

Factor	Value
α	≈ 1
h	≈ 300 m
$\bar{\phi}$	$\approx 37.5\%$
C_m	$\approx 2.1 \cdot 10^{-9}$ Pa
Δp_f	$\approx -2.66 \cdot 10^6$ Pa

Table 4.3: Rough estimates of the factors going into Eq .3.6 for the parameter K
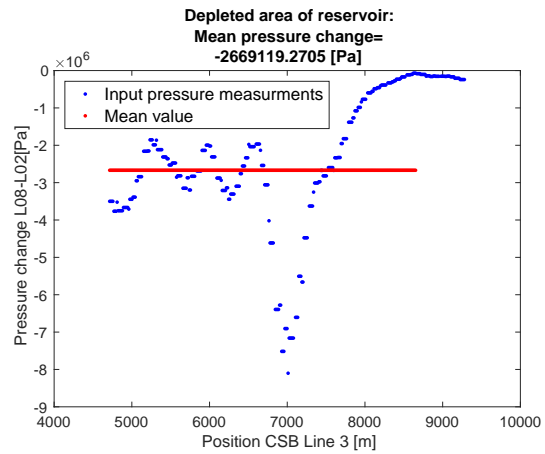
Figure 4.19: Average pressure change from the center of the subsidence bowl, red line illustrates the mean pressure change across the depleted area

The pressure change extracted from the center of the subsidence bowl along CSB Line 3, until the position corresponding to zero pressure change, can give an indicator of both the simplified reservoirs average pressure change and the extent of the reservoir radius. The radius of the approximated disk-shaped reservoir will be the extent from the center of the subsidence bowl till the position of no change in pressure. The reservoir depth is known from Ch. 2. These values give the rough estimates shown in Table 4.4. These approximations are where we would expect the inversion parameters to fluctuate close to if we assume $r = 0$ at the center of the subsidence bowl, and that the geomechanical model is reliable and able to describe the seafloor subsidence.

Parameter	Value
K [m]	≈ -0.71
R [m]	≈ 3940
D [m]	≈ 3300

Table 4.4: Rough estimate of expected model parameters

4.5   Seismic Interpretation and Time Shift Extraction

The seismic data from LoFS 2 and LoFS 8 are of generally good quality, but due to the limited amount of near offset reflections in the shallow parts, the imaging quality shallow is not as good as it is in the deeper section. The shallow section also has a lower fold, and will due to the dominating influence by far offset reflections potentially be more affected by anisotropy. As mentioned in Section 2.1, we have a seismically obscured area (SOA) above the central part of the seismic cube. On the edges of the SOA, we can also see some high amplitude reflectors, which can affect the quality of the calculated time shifts, see Figure 4.20a. The same section from the velocity cube show decrease in interval velocity in the uppermost part of the SOA, darker blue color on Figure 4.20b. This is where the gas accumulation has been reported to be most prominent (CoP, 2010). The dataset is in American polarity, where a zero-phase wavelet, with positive reflection coefficient, is represented by a central peak.

(a) Seismic section of CSB Line 3, TWT [ms]   (b) Interval velocity, V_{int} [m/s]
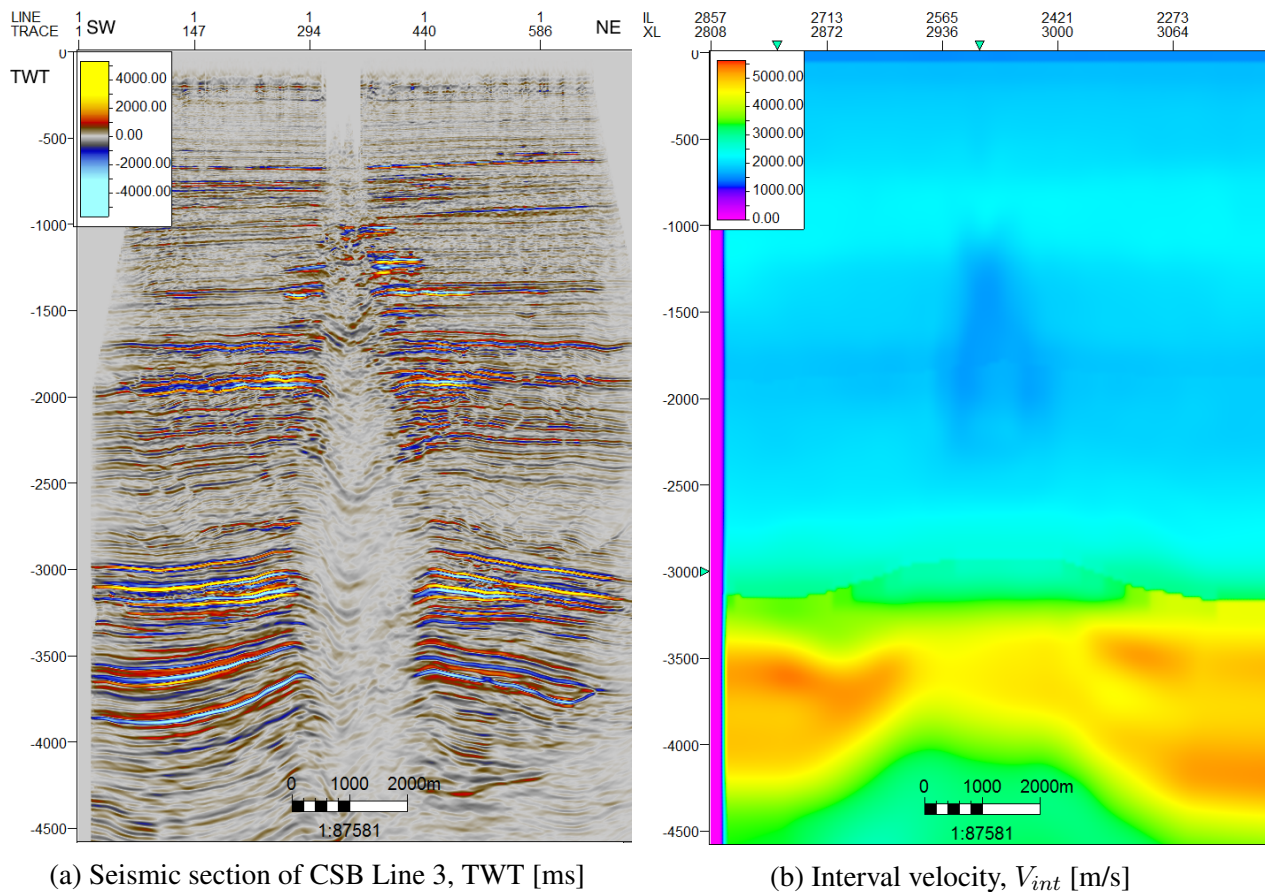
Figure 4.20: Seismic section of CSB Line 3 and corresponding section of Interval velocity

Nine continues reflector from Top Ekofisk fm and up has been interpreted on LoFS 2 and LoFS 8. Horizon 9 and 8 within the Rogaland Gp, respectively the Top Ekofisk- and Top Balder fm, which both are continues high amplitude reflectors. Horizon 7 and 6 are within the more faulted section of the Hordaland Gp. The remaining reflectors picked, are within the Nordland Gp. The lower part of Nordland Gp is affected by the fault slip extension from the Hordaland Gp. The upper part of the Nordland Gp has also been reported to contain smaller scale fractures and faults (CoP, 2010), not as prominent as in the Hordaland Gp. Some high amplitude anomalies are located along the edges of the SOA, see Figure 4.20a. These may be related to low saturation gas within silty layers. The most prominent are within the Miocene section. There are also some pull-effects along the edges of the SOA. These can be related to gas effect or by the presence of high-pressure zones, which has been reported in the Nordland Gp (CoP, 2010).
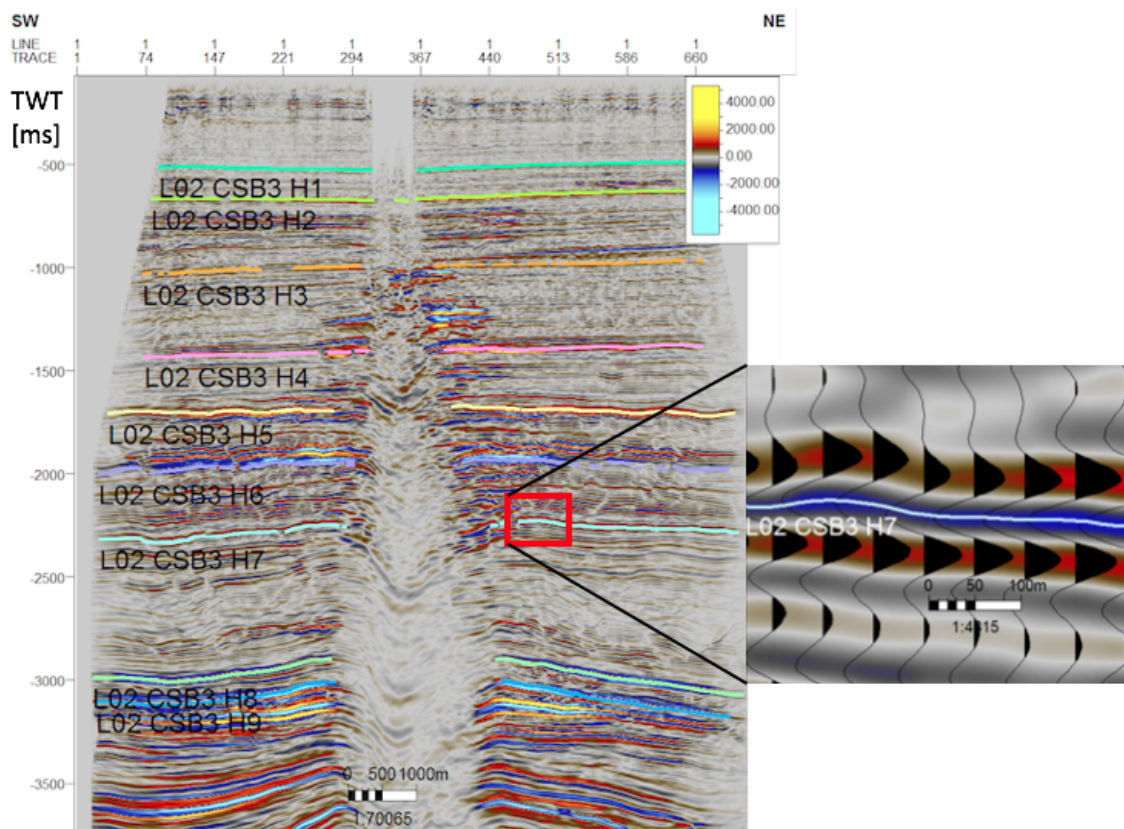
Figure 4.21: Series of continuous reflectors picked from top Reservoir (H9) and up. Strict maximum amplitude pick strategy is shown in zoomed image of H7

The horizons have been interpreted using Petrel. The interpretation settings have been changed to very strict to assure that the calculated time shifts correspond with the correct reflector. The method is using wavelet tracing, where the seed trace is correlated with neighboring traces accepting new traces with a correlation factor larger or equal to 0.8. The seeds are picked on maximum amplitude, see Figure 4.21.

4.5.1 Time-Lapse Seismic Data Correction

Due to these high amplitude anomalies and pull-effects, we need to take these factors into account before applying the time shifts in the inversion process. Below is the workflow used to correct and prepare the time shifts, before running the inversion process. The following data preparation has been performed using MATLAB, a programming software developed by MathWorks. The workflow has been completed for all the interpreted horizons, but is only shown for Horizon 7 below, as an example of the procedure.

Figure 4.22a shows the extracted TWT measurements along Horizon 7 (H7) for CSB Line 3. Red points are LoFS 2, and blue points are LoFS 8. Figure 4.22b show the time shifts between the monitor and base survey. In Figure 4.22 the SOA is shown as the vertical black/gray box. The red extension of this box represents the area in which the time shifts most likely has been affected by the amplitude anomaly on the edges of the SOA. We see on the extracted TWT that we have a sharp decrease close to the SOA, associated with a pull-down potentially due to gas saturation. The time shift measurements within this red area are removed for that reason. We can see from Figure 4.22b that the time shift measurements within this area are more scattered, and does not follow the same trend as the measurements outside the red area.

(a) TWT

(b) Δt
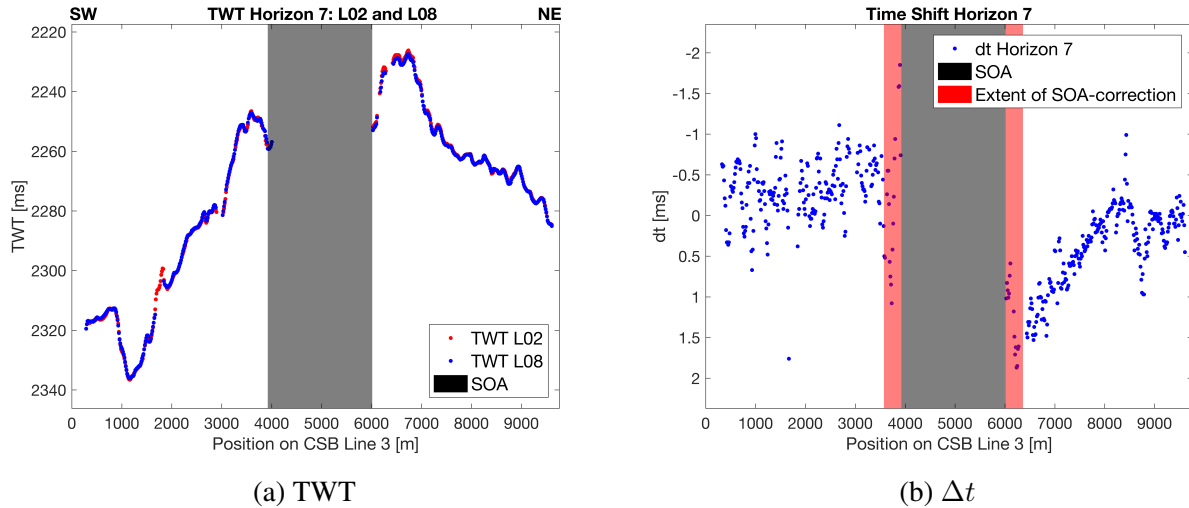
Figure 4.22: Extracted TWT and calculated time shift between LoFS 2 and 8

Figure 4.23 shows the extracted amplitude on both LoFS 2 and LoFS 8 on Horizon 7. On the stacked seismic data, Figure 4.20, we can see issues with low fold becoming clear on the edge of the seismic section. For that reason, there will be more uncertainty related to time shifts extracted on the edges of the data. Therefore, to be sure the data points used are credible, we remove time shifts with corresponding amplitude values lower than half of the mean amplitude. Figure 4.23 shows the extracted amplitudes with mean amplitude written in the header. The horizontal red line represents the cutoff for amplitude correction. Data points below this line are regarded as too weak to be used for the time-lapse study. From Figure 4.23 we see that most of the weak signals are on the edge, with a few low amplitude measurements around position 8500 m on the seismic line.

(a) Extracted amplitude H7 LoFS 2

(b) Extracted amplitude H7 LoFS 8
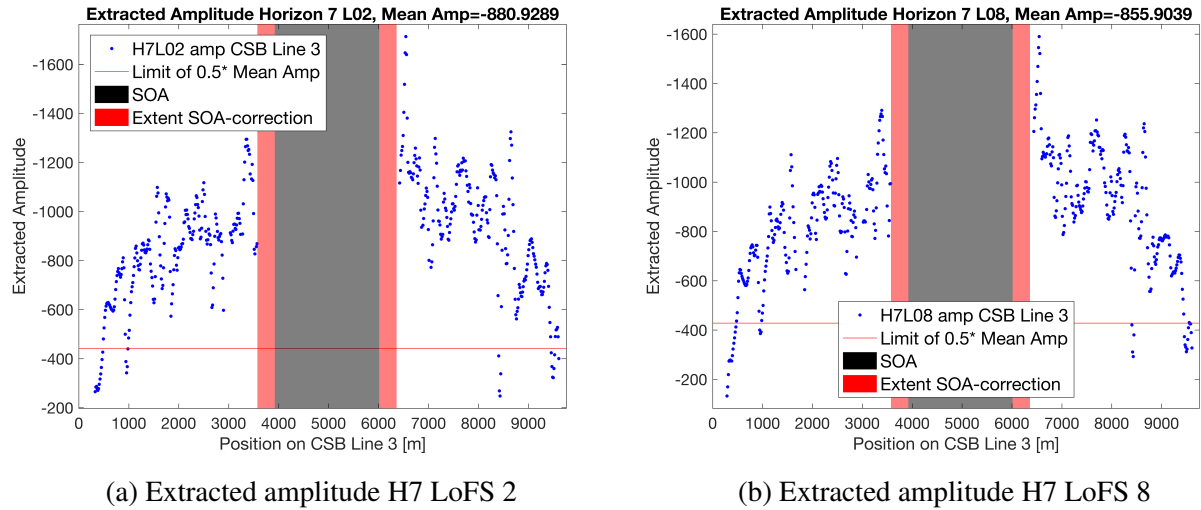
Figure 4.23: Extracted amplitude from H7 on LoFS 2 and LoFS 8 with threshold on amplitude correction as a horizontal red line

The red points in Figure 4.24a mark the time shift points corresponding with the weak signals. These points are removed on Figure 4.24b. The time shifts on the NW-side of the SOA are also removed, to give the input needed for the inversion, strictly positive time shifts as explained at the beginning of Section 4.4.

(a) Δt before amplitude correction

(b) Δt after amplitude correction
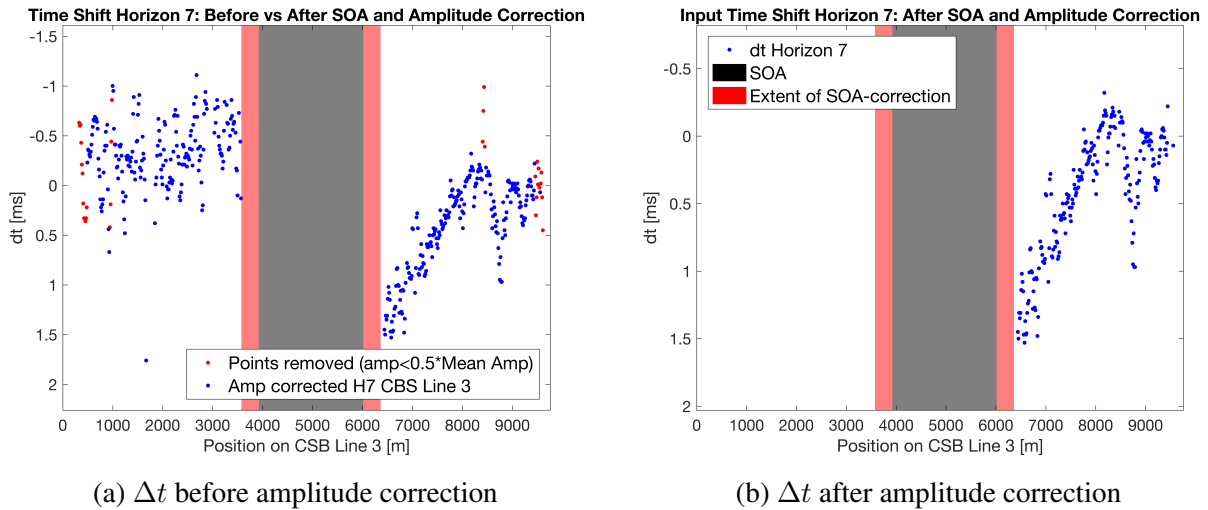
Figure 4.24: Before and after amplitude and outlier correction for the time shifts

Figure 4.25a shows the original data points in red, and the smoothed time shifts in blue. The final time shifts used for H7 is shown in Figure 4.25b. The time shifts were smoothed using MATLAB's internal "rlowess' method, a robust local regression using weighted linear least-squares and a first-degree polynomial model. The method is less influenced by outliers since the method assign zero weight to data points outside six mean absolute deviations. The method uses a span of 30 %, meaning that 30 % of the data points is used in the calculation of every smoothed value, using neighboring data points within the span.
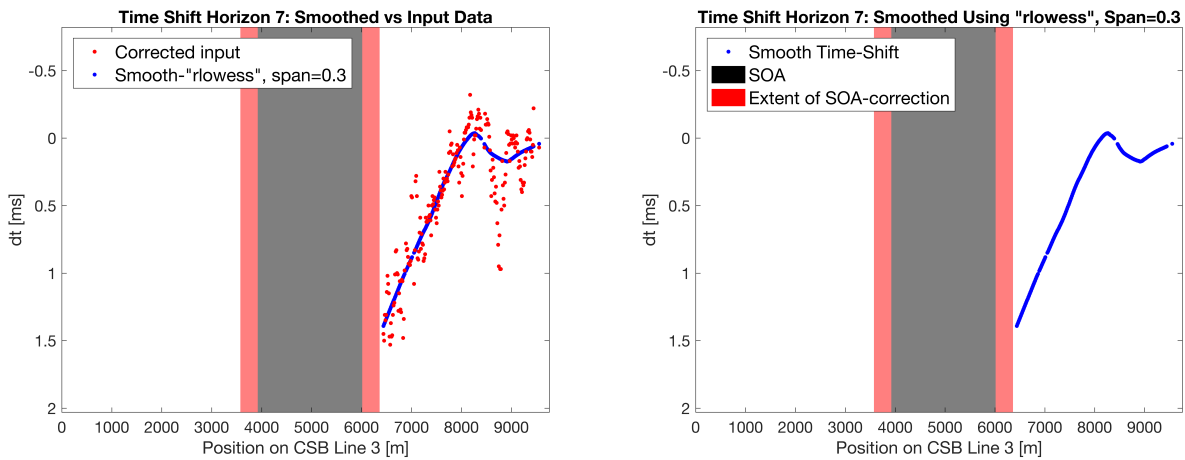
(a) Corrected Δt in red and smoothed Δt in blue　　　(b) Final Δt used as input

Figure 4.25: Final input time shifts, before and after smoothing using "rlowess"

After correcting all the horizons presented in Figure 4.21, we had to disregard the faulted Horizon 6 and Horizon 3. Too many data points were removed during these correction methods. Horizon 4 was also heavily corrected and was left out of the process. In the end, Horizon 1 and Horizon 8 were removed to level out the thickness of the resulting layers. The final input model going into the inversion process is represented by the horizons shown in Figure 4.26.
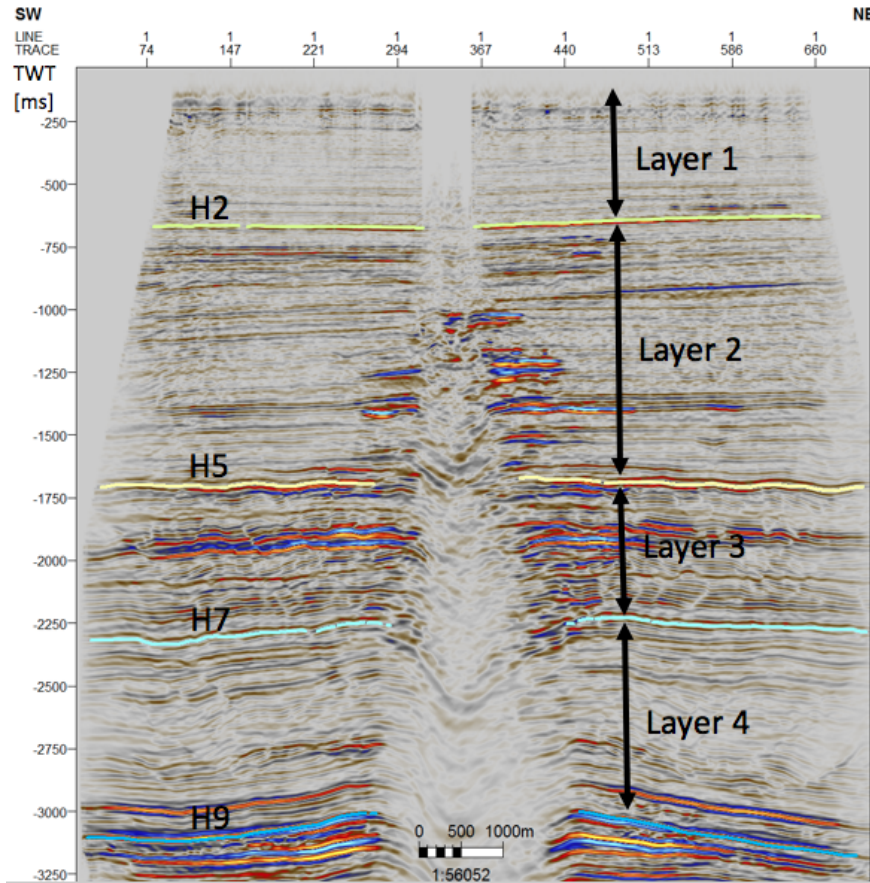
Figure 4.26: Seismic horizons used as input for the inversion process

From Figure 4.27, and the printed time shifts from Table 4.5, we can for the NE side of the SOA see an increasing trend in mean time shift with increasing depth. The number of data point used on each horizon is printed under NoE. The increasing trend in time shifts is what would be expected from an increasing trend in stretching of the overburden, calculated with Geertsma's geomechanical model.

Input Horizon	NoE	Average time shift
H2	254	0.19 ms
H5	222	0.33 ms
H7	215	0.42 ms
H9	190	0.59 ms

Table 4.5: Average time shift for input horizons and number of measurement points from NE-side of SOA
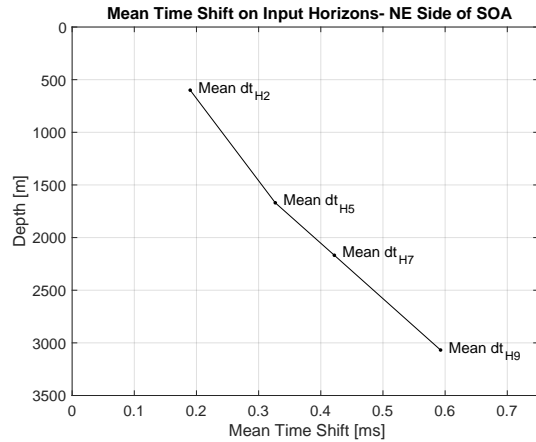
Figure 4.27: Input seismic horizons and corresponding average time shift from NE-side of SOA

From Section 4.1, Figure 4.2-4.4 showed how the time shift slices from reservoir level and into the overburden was dominated by negative time shift. The SW-side of the SOA show on average increasing negative time shift with depth, see Figure 4.28. From Figure 4.14b we can see that the SW-part of the seismic section is dominated by an area of average increase in pore pressure, compared to the NE-side with depletion.

Input Horizon	NoE	Average time shift
H2	163	-0.12 ms
H5	159	-0.13 ms
H7	194	-0.33 ms
H9	221	-0.50 ms

Table 4.6: Average time shift for input horizons and number of measurement points from SW-side of SOA

Figure 4.28: Input seismic horizons and corresponding average time shift from SW-side of SOA

Figure 4.29 shows the average time shifts for the same horizons interpreted along XL 1286 and XL 412, outside the reservoir zone. Ideally, we should see no time-lapse changes in these areas. As mentioned in Section 2.3, repeatability is an important issue in order to detect small time-lapse differences. Horizon 2 in XL 412 shows the largest difference compared to the other interpreted horizons from Figure 4.29a. From Figure 4.29b we can see that the number of data points going into the mean value calculation along XL 412, are less than for XL 1286, due to the geometry of the LoFS installation. Large time shift measurements will, therefore, have more influence on XL 412 than on XL 1286, and may help to explain the large mean time shift difference for H2. From Figure 4.29 we can, therefore, indicate that the time shifts on average are in the order of -0.1 ms. The error associated with the extracted time shifts may, therefore, be around this magnitude. The magnitude is better shown plotting the average time shifts from the cross lines together with the average time shifts from CSB Line 3, see Figure 4.30.
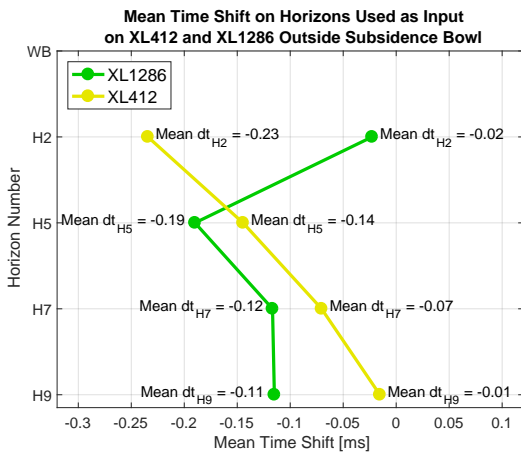
(a) Average time shift from XL412 (yellow) and XL1286 (green) outside the reservoir zone
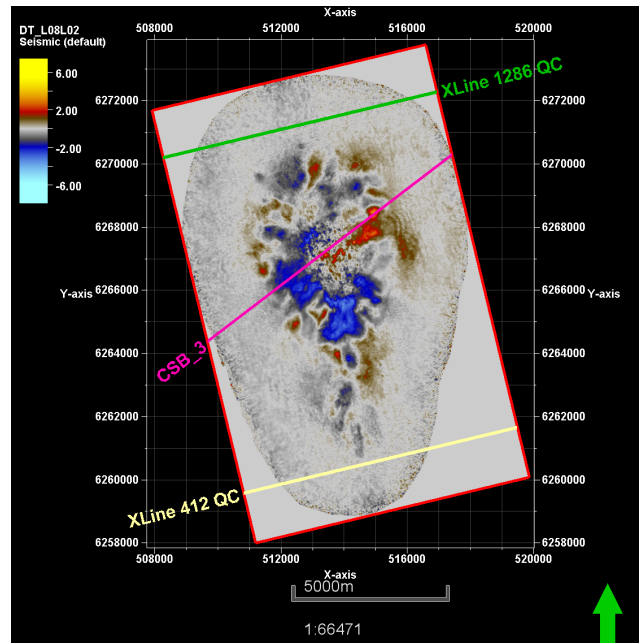
(b) Position of XL412 and XL1286 in comparison to the input line CSB Line 3 shown on top of a time shift slice at 10500 ft (3200 m)

Figure 4.29: Quality control of repeatability between LoFS 2 and 8
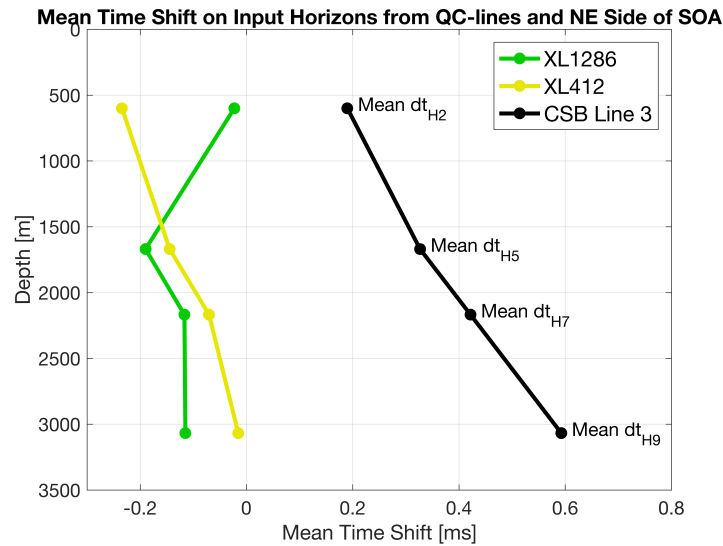
Figure 4.30: Figure 4.29a and 4.27 together showing the magnitude difference between what is associated with error (Cross Lines) and data above reservoir (CSB Line 3)

The resulting time shifts for each of the horizons used as input are plotted in Figure 4.31a. The input time shifts are using the same position system as introduced for the bathymetry data, see Figure 4.18d, where $r = 0$ represents the center of the subsidence bowl along CSB Line 3. For each of the horizons, we see an increasing variance in time shift measurements with increasing position. Plot showing input time shifts, and resulting data after smoothing for each of the horizons, are shown in Appendix B.3. The magnitude of the time shifts decreases with increasing position, making these measured time shifts more sensitive to error. The data points in red are, therefore, defined as data associated with more uncertainty. These points all lie around time shifts of 0-0.5 ms. Uncertainty with a magnitude around -0.1 ms will have a greater effect here, than where the time shifts are larger closer to the center of the subsidence bowl, since the error will make up a more substantial portion of the resulting time shift. The smoothed time shift curves are more fluctuating with increasing position, which is easier to see when only looking at time shifts down to 2 ms, Figure 4.31c. The dashed lines are here representing the data associated with more errors.
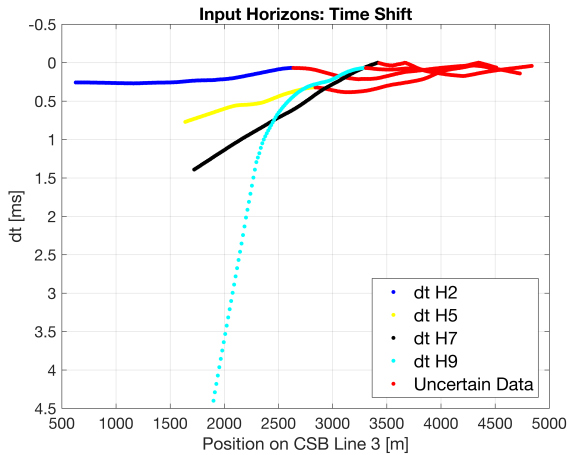
(a) Input time shifts on horizons used. Red points mark uncertain data
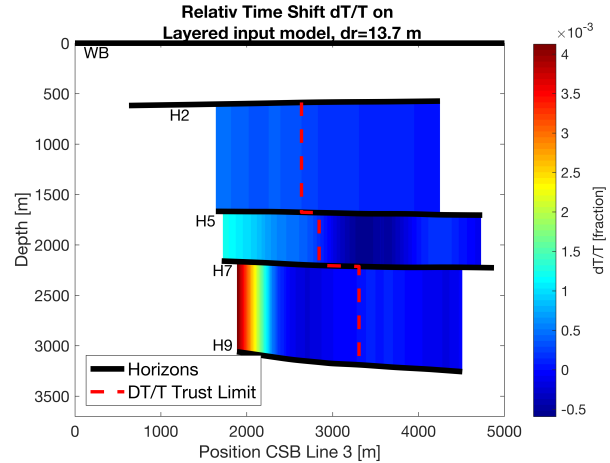
(b) Relative time shifts within layers, trust limit defined by dashed red line
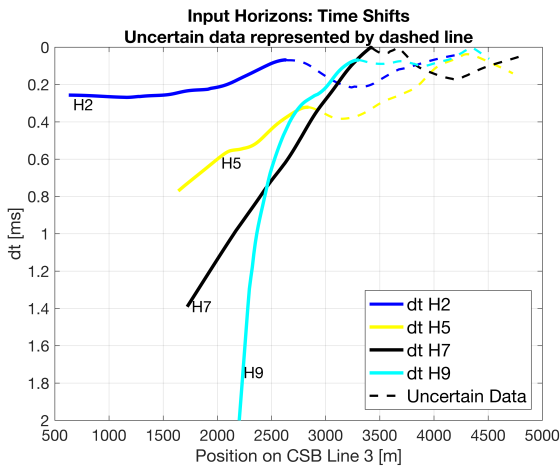
(c) Zoomed image of input time shifts, uncertain data represented by dashed lines
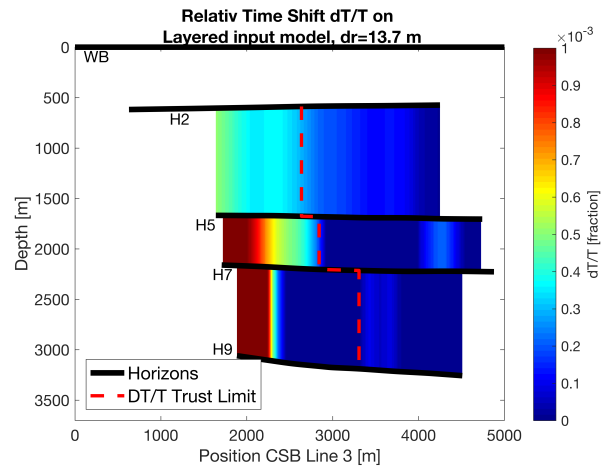
(d) Same as Figure 4.31b but with colorbar limit of $1 \cdot 10^{-3}$

Figure 4.31: Input time shifts for the horizons and corresponding relative time shifts for the four layers, and the definition of the trust limit from the time-lapse seismic data

Figure 4.31b shows the resulting relative time shifts for the four layers. The threshold for trustworthy relative time shifts is defined together with the limits from Figure 4.31a. The lowest limit of trustworthy time shifts from the two horizons represented within the calculation of relative time shifts, is used as the limit for relative time shifts within the layer. In Figure 4.31d the color bar limit has been set at $1 \cdot 10^{-3}$, to show the subtle differences within the layers better.

From Figure 4.31b and 4.31d we see the initial depth measurements from the horizons interpreted. The water bottom is shown as well, but since we do not have a clear reflector to pick on seismic, we can not calculate any relative measurements for the first layer. The initial depth measurements for the input horizons are calculated from depth conversion, and the resulting initial thickness variations are shown in Figure 4.32.
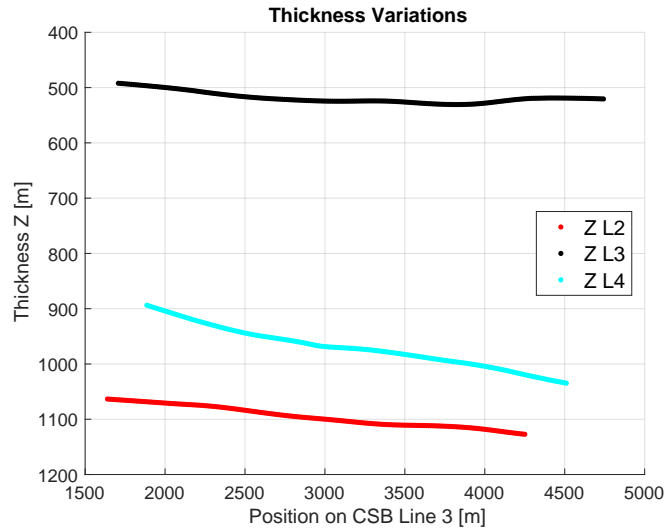
Figure 4.32: Thickness variations calculated from depth conversions on base survey (LoFS 2)

The chosen input values for the inversion process show coherence with the trends expected from a depleting reservoir. Figure 4.33 sum up the data extracted along the NE-side of the chosen seismic line (CSB Line 3). Where we have decreasing displacement with increasing position from the center of the subsidence bowl, Figure 4.33a. On average decrease in reservoir pore pressure, Figure 4.33b. And positive time shifts which increase with increasing depth, where Figure 4.33c only shows the most trustworthy time shift measurements.

(a) Extracted u_z

(b) Extracted reservoir Δp_f

(c) Extracted Δt for input horizons
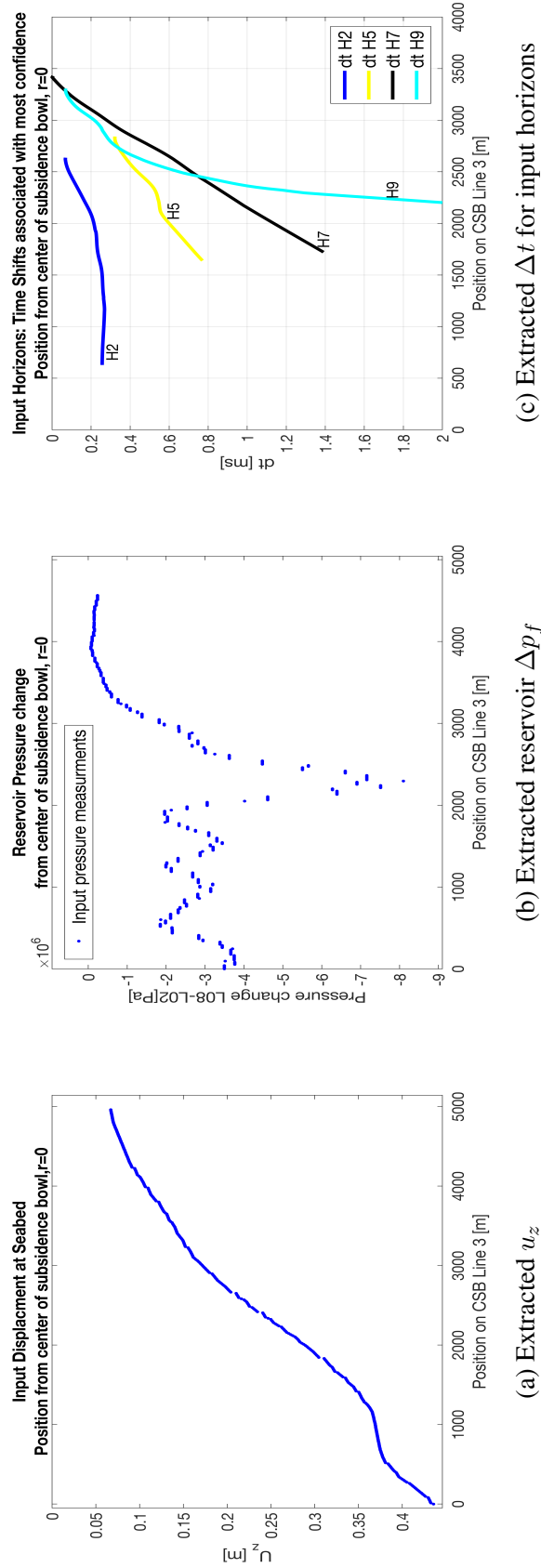
Figure 4.33: Pressure, displacement and time shifts extracted along NE-part of CSB Line 3 representing the input values for the inversion process. Position $r = 0$ representing the center of the subsidence bowl.

Chapter 5

Results

5.1 Global Inversion for K, R and D

The inversion process was initiated on a course grid, with model space from Table 5.1. The factor K was kept negative since the data acquired was in a zone of depletion, as presented in Ch. 4.

Parameter	Range	Discretization Δ
K [m]	[-0.1, -2]	-0.1
R [m]	[1000, 10000]	1000
D [m]	[1000, 10000]	1000

Table 5.1: Coarse model space used in the initial global inversion process for K, R and D

Figure 5.1 represent the surface- and contour plot of the relative error function. Relative error values above 4 have not been shown on the surface plot. The color bars on both surface and contour plot have been cut to display the minimum better. From the contour plot in Figure 5.1b the minimum is better illustrated by the red dot at $D = 3000$, $R = 2000$ and $K = -0.7$.
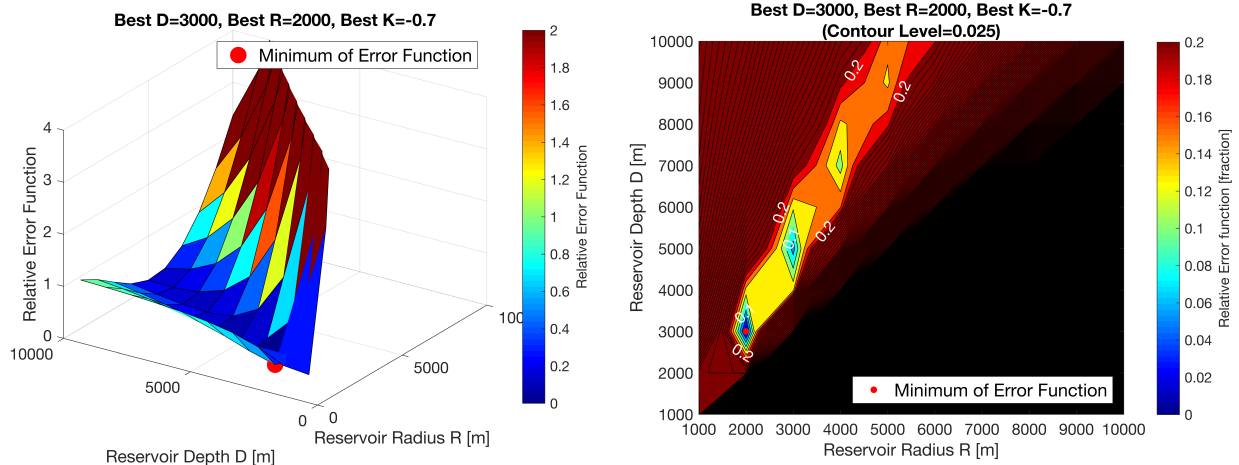
(a) Surface plot of error function
best model parameter given above the plot

(b) Contour plot of error function
contour level of 0.025

Figure 5.1: Surface and contour plot of error function with input values from Table 5.1, for the K, R and D inversion process. The valley shaped error function has a minimum defined by the red dot

The same inversion process is executed with a denser model space confined by the minimum from Figure 5.1. The discretizations provided in Table 5.2 show a much denser model space. The number of elements within the error function will increase and provide a further detailed representation of the minimum, but at a high computational cost due to the increasing number of model parameters to check.

Parameter	Range	Discretization Δ
K [m]	[-0.1, -1.3]	-0.05
R [m]	[1000, 6000]	250
D [m]	[500, 5000]	250

Table 5.2: Dense model space used in the initial global inversion process for K, R and D

From the surface plot in Figure 5.2a the finer grid becomes apparent with the increasing number of calculated error function values. The contours defining the minimum is also better formed, see Figure 5.2b. The elliptically shaped contour lines with a spacing of 0.01 indicate that the slope of the error function is not very steep, giving an indication of the sensitivity related to the inversion process.
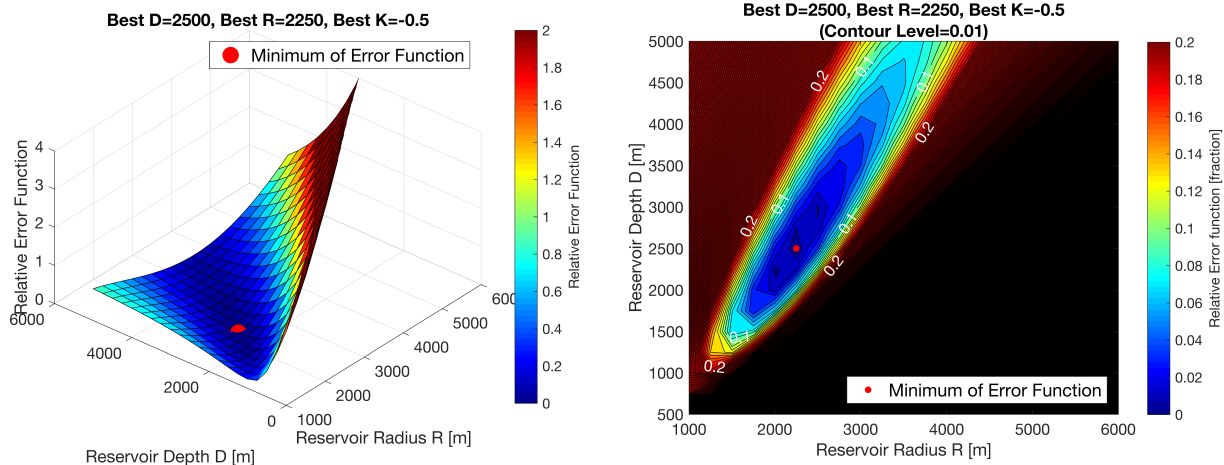
(a) Surface plot of error function
best model parameter given above the plot

(b) Contour plot of error function
contour level of 0.01

Figure 5.2: Surface and contour plot of error function with input values from Table 5.2, from the inversion process for K, R and D. The dense model space around the minimum provide a more detailed error function

The minimum of the error function is represented by the two elements of the objective function, see Eq.3.13. The value of these two elements $\chi^2_{U_z}$ and $\chi^2_{\frac{\Delta T}{T}}$ for the minimum is represented in Table 5.3. The magnitude of the relative error in displacement at the seabed is dominating the resulting value of the objective function, as expected from the presentation of the method in Ch. 3. The difference between measured and modeled displacement at the seabed is visually shown in Figure 5.3.

Figure 5.3: Measured displacement (blue) compared to modeled displacement (red), from the inversion process for K, R and D

Element of Error Function	Value [fraction]
$\chi^2_{U_z}$	$1.1 \cdot 10^{-3}$
$\chi^2_{\frac{\Delta T}{T}}$	$5.2 \cdot 10^{-33}$

Table 5.3: Value of the elements within the error function with input values from Table 5.2

The resulting calculated $\mathcal{R}$-factor for each of the layers is shown in Figure 5.4, except for layer 1 where we only have the modeled displacements, see Figure 5.4a. $\mathcal{R}$-factor values are plotted together with the corresponding relative time shifts and relative thickness change for the particular layer, represented by the Y-axis on the right. The Y-axis on the left represents the values of the modeled $\mathcal{R}$-factor. The modeled $\mathcal{R}$-factor relies on both $\frac{\Delta Z}{Z}$ and $\frac{\Delta T}{T}$ as shown in Eq. 3.9 from Ch. 3. Hence, the values of modeled $\mathcal{R}$-factor is better understood if we simultaneously look at the modeled $\frac{\Delta Z}{Z}$ and $\frac{\Delta T}{T}$.

(a) Layer 1

(b) Layer 2

(c) Layer 3

(d) Layer 4
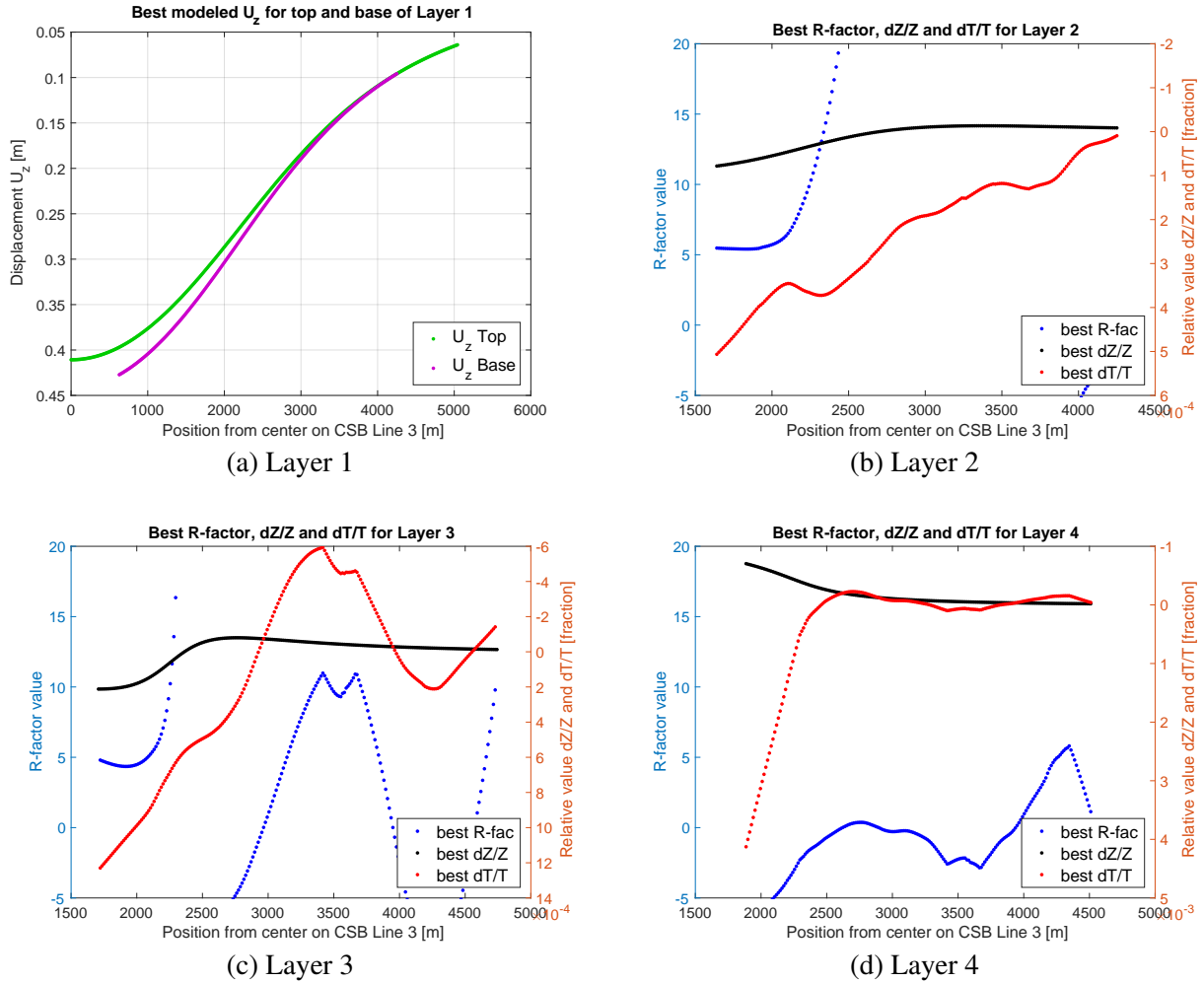
Figure 5.4: Modeled best $\frac{\Delta T}{T}$, $\frac{\Delta Z}{Z}$ and resulting $\mathcal{R}$-factor with position from the center of the subsidence bowl, from the inversion process for K, R and D. Right Y-axis for the relative changes, and left Y-axis for $\mathcal{R}$-factor values up to 20

From Eq. 3.9 the relative thickness change, $\frac{\Delta Z}{Z}$, is in the denominator. When this value approaches zero, the inversion process will become mathematically unstable. The instability becomes apparent for layer 2 and 3 as a rapid increase in $\mathcal{R}$-factor values. The resulting best model parameters are the input values determining the geomechanical setting of the overburden.

The model parameter which is easiest to quality control is the reservoir D. We know that it lies in the range of 2900-3300 m. For this inversion process, the calculated best reservoir depth was at 2500 m, implying that parts of layer 4 will be beneath the calculated best reservoir depth. Due to the elasticity of the Geertsma equations, the displacements beneath the reservoir will have negative values, and the resulting relative thickness change and $\mathcal{R}$-factor values will also become negative,

see Figure 5.4d. The negative $\mathcal{R}$-factor values are not of interest in this setting, which is why the Y-axis only include values down to -5 for illustration purposes.

(a) Color plot of $\mathcal{R}$-factor values

(b) Contour plot of the modeled vertical displacement
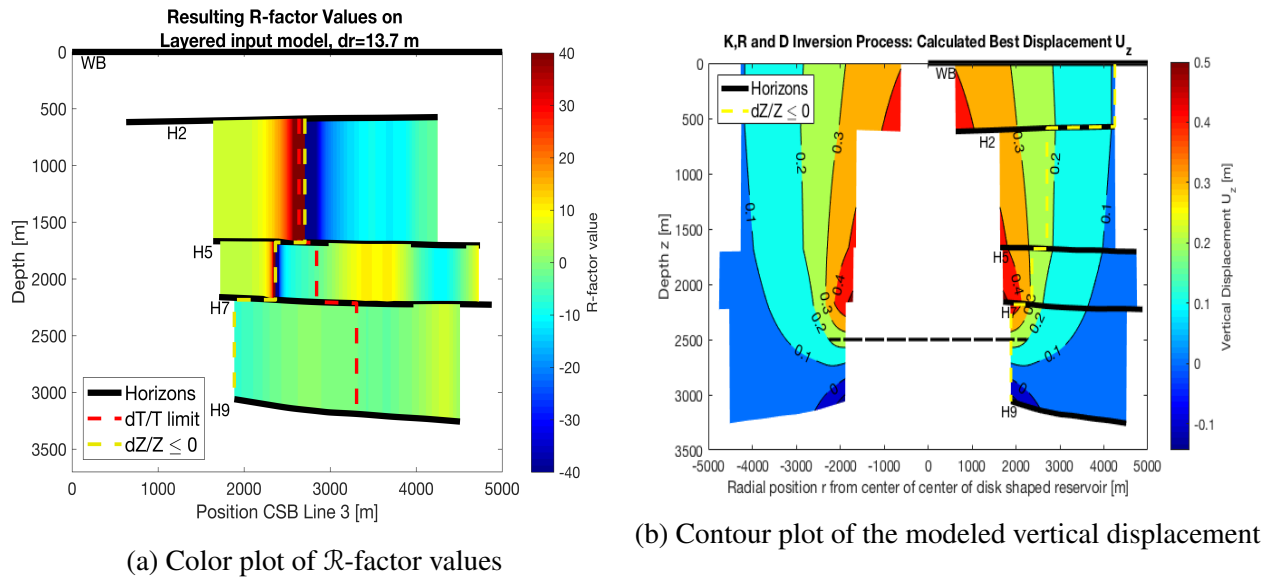
Figure 5.5: Color plot of modeled $\mathcal{R}$-factor values from the inversion process for K, R and D, with trust limits for $\frac{\Delta T}{T}$ (red) and limit for $\frac{\Delta Z}{Z}$ (yellow). Displacement plot used to show the $\frac{\Delta Z}{Z}$-limit

Figure 5.5a shows the interpretation setting as presented in Figure 4.31b. The color bar in this plot represents the estimated $\mathcal{R}$-factor values. The time shift trust limit, presented in from Figure 4.31b (dashed red line), is overlaid the plot together with a limit of where the relative thickness change cross from positive to negative (dashed yellow line). This limit is better shown in Figure 5.5b, a contour plot illustrating the best-calculated displacement after the inversion process. The limit will be drawn where there is no change between top and base displacement, or where the top reservoir has a larger displacement than the base of the layer, which is the case for most of layer 4. Since the geomechanical model is based on symmetry, the calculated displacement from the input data can be mirrored laterally. A dashed line shows the lateral extent of the best-calculated radius of the reservoir. The SOA is apparent as the middle area without data (white background color).

The trend we saw from Figure 5.4, with increasing $\mathcal{R}$-factor values when approaching zero relative thickness change, is better visualized in Figure 5.5a, with the trust limits included. We can see for layer 2 and 3 up towards the dashed yellow line that we have an increasing $\mathcal{R}$-factor value trend which switches to large negative value when crossing the line. For layer 4 we have, as mentioned,

due to the inversion process negative $\frac{\Delta Z}{Z}$ from the first data point resulting in negative $\mathcal{R}$-factor values.

5.2 Reservoir Depth Kept Constant

One attempt to improve the resulting $\mathcal{R}$-factors was to lock the model parameter associated with the reservoir depth at the known depth of the reservoir, using $D = 3300$ m, hoping to improve the modeled values for the four layers.

Parameter	Range	Discretization Δ
K [m]	[-0.1, -2]	-0.1
R [m]	[1000, 10000]	1000

Table 5.4: Coarse model space used in the global inversion process for K and R, constant depth at $D = 3300$ m

We repeated the inversion process with the same approach as in Section 5.1, first around a large model space with course grid, Table 5.4, to identify the inner minimum contours lie close to the same area as before, but now with a reservoir depth at $D = 3300$ m. From the surface- and contour plots from Figure 5.6 we can see that the shape of the error function is different compared to Figure 5.2b, where the reservoir depth was included as a model parameter. A boomerang-shaped feature confines the lowest contour values in 5.6b.
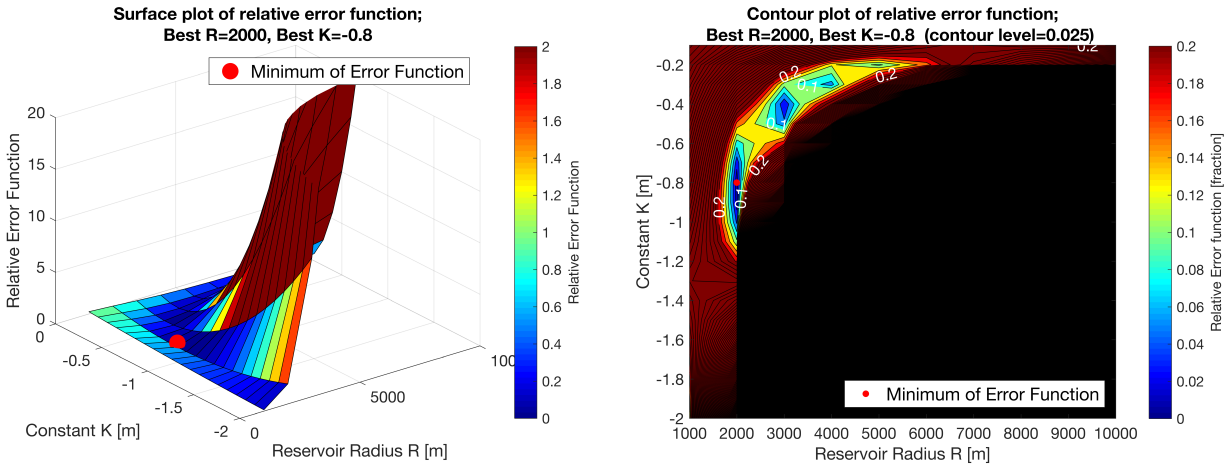
(a) Surface plot of error function
best model parameter given above the plot

(b) Contour plot of error function
contour level of 0.025

Figure 5.6: Surface and contour plot of error function with input values from Table 5.4, from the inversion process for K and R

The inversion process was repeated around the minimum from Figure 5.6 with model space given by Table 5.5. Figure 5.7 gives the resulting plots of the error function.

Parameter	Range	Discretization Δ
K [m]	[-0.1, -1.3]	-0.05
R [m]	[1000, 6000]	250

Table 5.5: Dense model space used in the global inversion process for K and R, constant depth at $D = 3300$ m

The radius R and constant K corresponding with the minimum of the error function, are respectively $R = 1750$ m and $K = -1.05$ m, see header of Figure 5.7. The contour level of Figure 5.7b is 0.01, and the shape of the contour lines are better defined due to the denser model space. From the contour plot, it becomes clear that the minimum is better defined with D included as a model parameter. Take for instance the shape of the inner contour of the contour plot in Figure 5.7b. The inner contour is expanded/stretched more than the inner contour of Figure 5.2b, indicating that the definition of the minimum is reduced. Making it easier to keep wrong model parameters when running the algorithm.
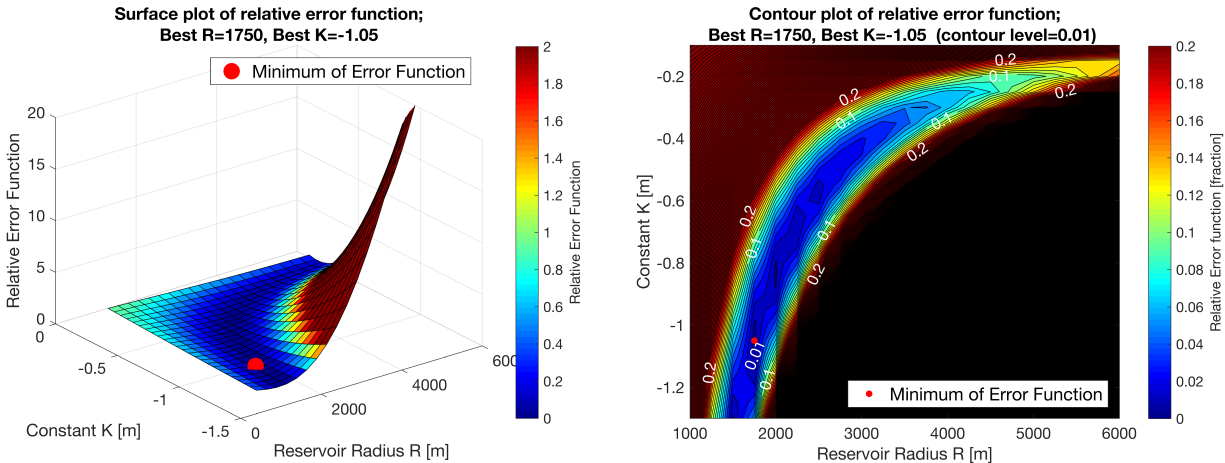
(a) Surface plot of error function
best model parameter given above the plot

(b) Contour plot of error function
contour level of 0.01

Figure 5.7: Surface and contour plot of error function with input values from Table 5.5, from the inversion process for K and R. From the contour plot we can see that the blue area is dragged along a large model space

The discretization of K and R from Table 5.5 are the same as used in Table 5.2, but after locking the reservoir depth at a constant level, the resulting minimum of the error function is becoming higher. Table 5.6 show the relative error of the elements within the objective function. We have an increase in $\chi^2_{U_z}$ but a decrease in $\chi^2_{\frac{\Delta T}{T}}$. Due to the order of magnitude, the relative error in seafloor subsidence is dominating the error function. The resulting displacement at the seafloor calculated using the best model parameters compared to the measured displacement, is shown in Figure 5.8. The fit is decreased compared to the fit from Figure 5.3.

Figure 5.8: Measured displacement (blue) compared to modeled displacement (red), from the inversion process for K and R

Element of Error Function	Value [fraction]
$\chi^2_{U_z}$	$4.4 \cdot 10^{-3}$
$\chi^2_{\frac{\Delta T}{T}}$	$3.1 \cdot 10^{-33}$

Table 5.6: Value of the elements within the error function with input values from Table 5.5

By locking the reservoir depth at $D = 3300$ m, we know that the displacement calculated by the geomechanical model will be positive when using the model space from Table 5.5. The best-calculated radius at 1750 m will, hence, mean that most of the input data available will be outside the extent of the reservoir, where the modeled displacements from the geomechanical model are smaller. From Figure 5.9 we can see that the relative thickness change closest to the center of the subsidence bowl, is positive for all the four layers, but only marginally since the calculations are on the edge of what the inversion process has calculated as the reservoir radius.

(a) Layer 1

(b) Layer 2

(c) Layer 3

(d) Layer 4
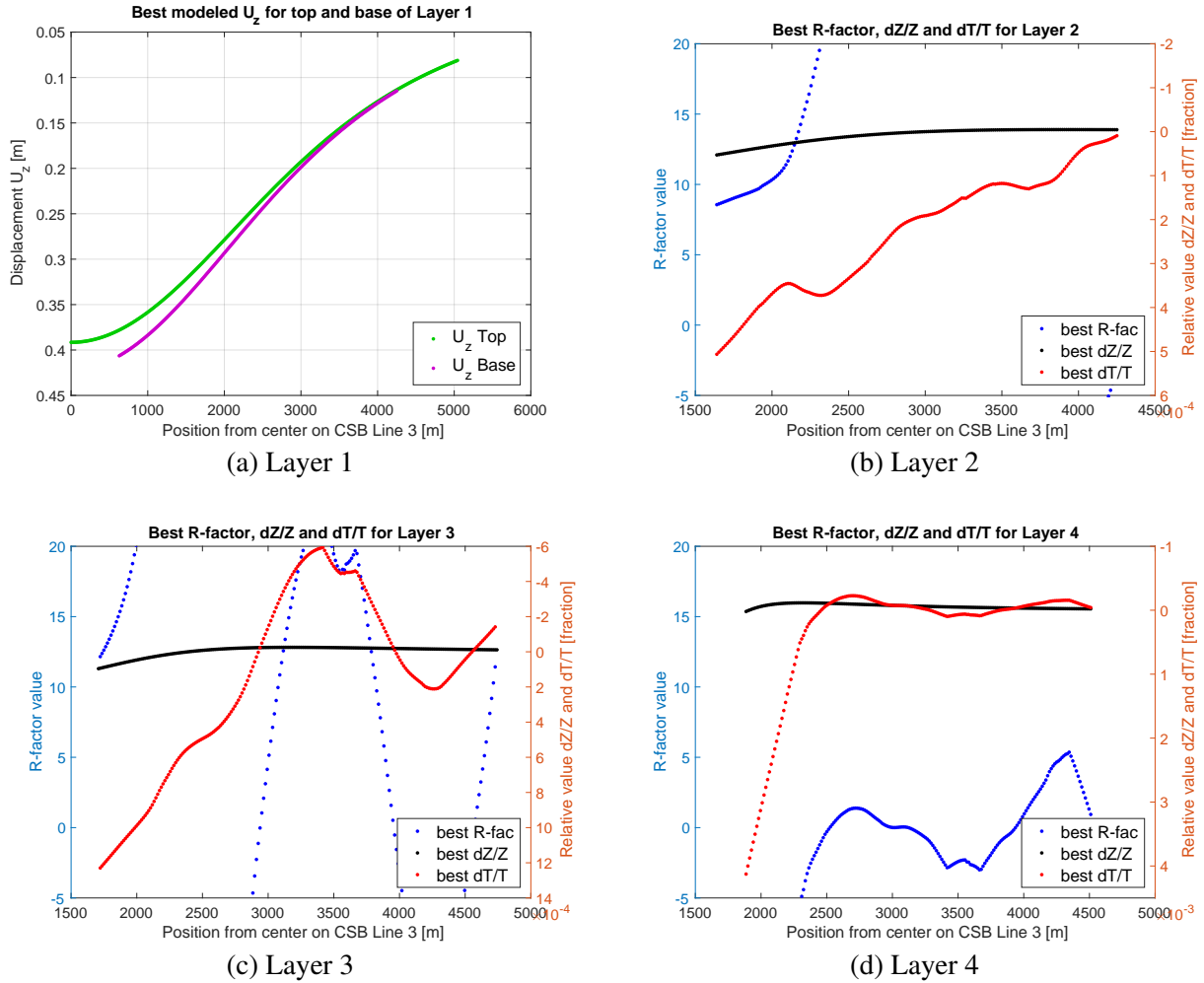
Figure 5.9: Modeled best $\frac{\Delta T}{T}$, $\frac{\Delta Z}{Z}$ and resulting $\mathcal{R}$-factor with position from the center of the subsidence bowl, from the inversion process for K and R. Right Y-axis for the relative changes, and left Y-axis for $\mathcal{R}$-factor values up to 20

Layer 2 show $\mathcal{R}$-factor values larger than for the layer 2 in Figure 5.4b. The $\mathcal{R}$-factor values are gradually increasing until $\frac{\Delta Z}{Z}$ approach zero, and the calculation becomes unstable. For Layer 3 and 4, $\frac{\Delta Z}{Z}$ approach zero almost instantly for the data available, and the $\mathcal{R}$-factor values become large very fast, and even negative, were the displacement at the top of the layer is greater than the displacement at the base of the layer.

(a) Color plot of $\mathcal{R}$-factor values

(b) Contour plot of the modeled vertical displacement
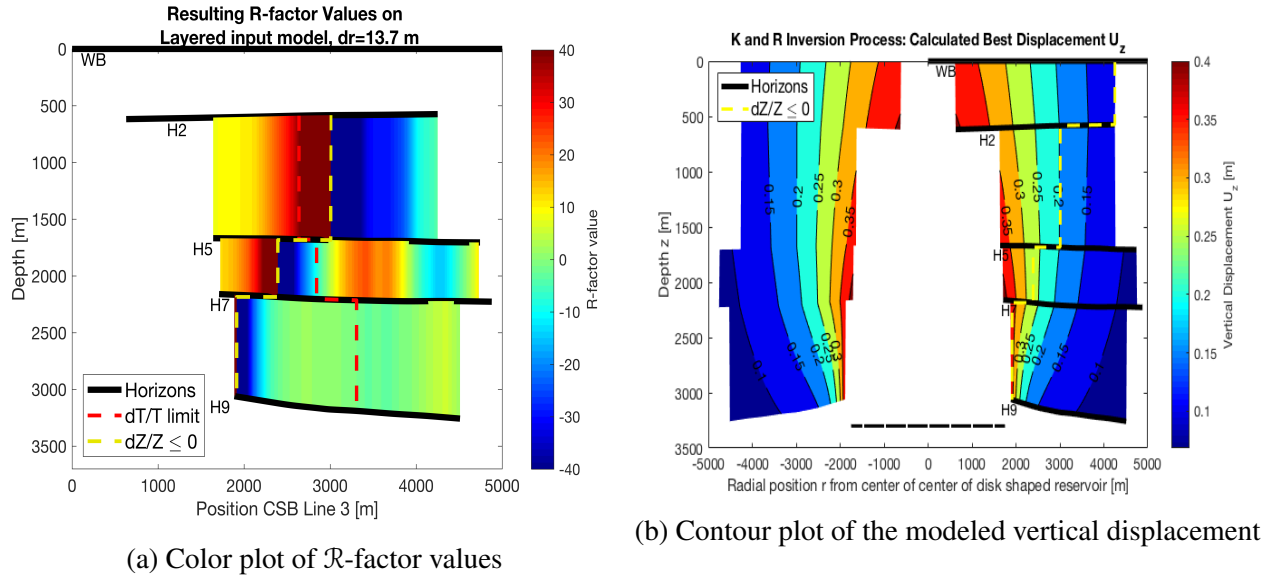
Figure 5.10: Color plot of modeled $\mathcal{R}$-factor values from the inversion process for K and R, with trust limits for $\frac{\Delta T}{T}$ (red) and limit for $\frac{\Delta Z}{Z}$ (yellow). Displacement plot used to show the $\frac{\Delta Z}{Z}$-limit

The color plot of the layers shows the trends even better, see Figure 5.10a. With increasing $\mathcal{R}$-factor values towards the limit of $\frac{\Delta Z}{Z} \leq 0$, we see that these limits are drawn with decreasing position on the CSB line for increasing depth, better shown with Figure 5.10b as support. For layer 3 it seems that we only have data from the position where the $\frac{\Delta Z}{Z}$ graph in Figure 5.9c are too close to zero and the calculated $\mathcal{R}$-factor values start to increase drastically. For layer 4 we only have data outside the calculated best reservoir radius R. For that reason, we only have negative $\mathcal{R}$-factor values since $\frac{\Delta Z}{Z}$ is negative throughout the layer.

5.3 Reservoir Depth and Radius Kept Constant

The last attempt to "push" the inversion process towards the expected model parameters from Table 4.4, was to run the inversion process with only K as a free model parameter. While keeping $D = 3300$ m and $R = 3940$ m. The model space for K was the same as used in the inversion process from Section 5.1 and 5.2. Intuitively this will not provide the lowest error function value, because the calculated errors in this process will essentially be one vertical slice from $R = 3940$ m on Figure 5.7b. The extracted errors do not cross the inner contour of the error function, but by

running the inversion process with larger radius R, more of the data used will now be located above the reservoir, where we expect the displacement to be greater and continuously positive $\frac{\Delta Z}{Z}$.

In the header of Figure 5.11 we see that the best value of $K = -0.3$ after the inversion process. The resulting elements of the error function are given in 5.7. The relative error in seabed subsidence has increased, also clearly shown in Figure 5.11. The relative error in subsidence is dominating the resulting error function value.

Element of Error Function	Value [fraction]
$\chi^2_{U_z}$	0.059
$\chi^2_{\frac{\Delta T}{T}}$	$7.0 \cdot 10^{-34}$

Table 5.7: Value of the elements within the error function with input values for the factor K from Table 5.5

Figure 5.11: Measured displacement (blue) compared to modeled displacement (red), from the inversion process for only K, keeping $D = 3300$ m and $R = 3940$ m

Since more of the data is situated above the reservoir, the position of the limit of $\frac{\Delta Z}{Z} \leq 0$ has position further away from the center of the subsidence bowl. The modeled relative thickness change is still very close to zero for all the layers, especially layer 3 and 4, see Figure 5.12, causing instabilities in the calculated $\mathcal{R}$-factor. By locking R at the increased value, caused the best K to decrease, and the resulting the marginal relative thickness changes.

(a) Layer 1

(b) Layer 2

(c) Layer 3

(d) Layer 4

Figure 5.12: Modeled best $\frac{\Delta T}{T}$, $\frac{\Delta Z}{Z}$ and resulting $\mathcal{R}$-factor with position from the center of the subsidence bowl, from the inversion process for K. Right Y-axis for the relative changes, and left Y-axis for $\mathcal{R}$-factor values up to 20

The color map illustrating the calculated $\mathcal{R}$-factor values are shown in Figure 5.13a, where we can see the limit of negative relative thickness change is far from the center of the subsidence bowl. The resulting $\mathcal{R}$-factor values are still very high due to the marginal modeled $\frac{\Delta Z}{Z}$-values. Figure 5.13b show the calculated best displacement after the inversion process.

(a) Color plot of $\mathcal{R}$-factor values

(b) Contour plot of the modeled vertical displacement
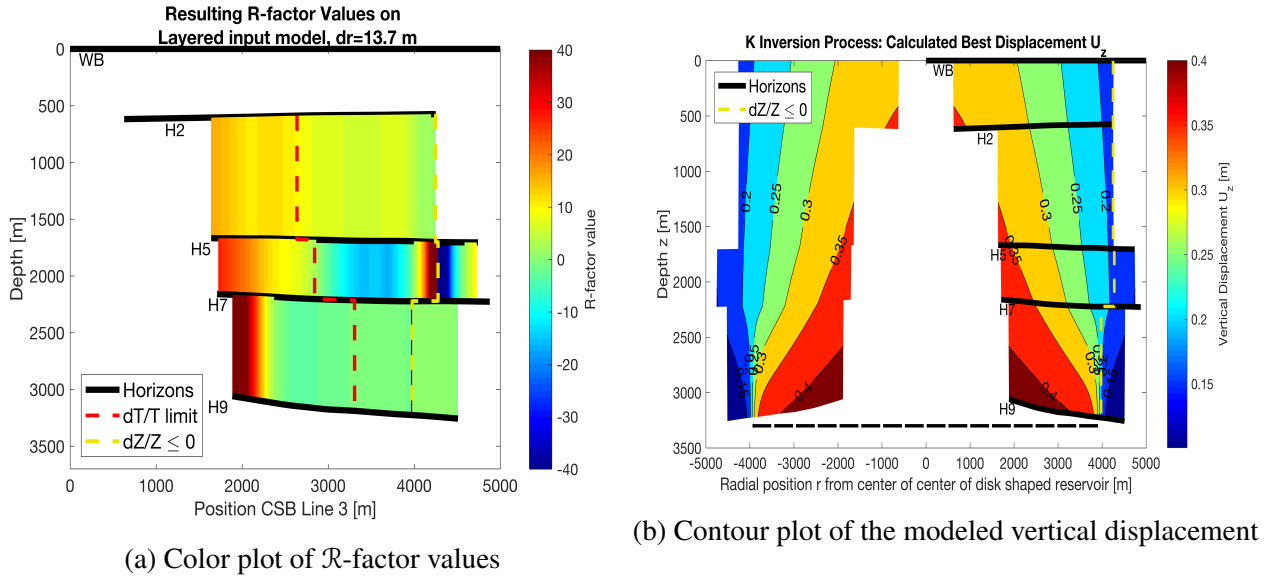
Figure 5.13: Color plot of modeled $\mathcal{R}$-factor values from inversion process for K, with trust limits for $\frac{\Delta T}{T}$ (red) and limit for $\frac{\Delta Z}{Z}$ (yellow). Displacement plot used to show the $\frac{\Delta Z}{Z}$-limit

5.4 Depleted Zone Estimated as one Disk-Shaped Reservoir

Figure 4.33c represents the most trusted time shifts along CSB Line 3. Due to the SOA, we are missing the time shifts associated with the largest displacement from Figure 4.33a. From the center of the subsidence bowl, $r = 0$, until $r = 2000$ m we almost have no seismic data. An attempt to improve the inversion process was to move the "center of subsidence bowl," or the initiation point for the inversion process, to where most of the seismic data starts. The new center was chosen at $r = 1968$ m, and the inversion process will start at $r = 1968$ m, where it earlier started at $r = 0$. The displacement measurements from $r = 0$ to $r = 1968$ m will hence not be used in the inversion process, the adapted displacement measurements will be given by Figure 5.14a, and the associated time shifts are shown in Figure 5.14b, which we calculate the input relative time shifts from. The positioning system from earlier is used, to make it easier to compare the results. From Figure 4.33b the position $r = 1968$ m is situated further into the on average depleted area.

From this new input data, new model parameters can be inferred, compared to the ones indicated in Table 4.4 for the inversion process constrained by displacement from $r = 0$. The modeled reservoir radius will be smaller due to the decreasing constraining displacement curve at the seafloor, Figure

5.14a. While the model parameter K and D still should be close to the presented values in Table 4.4, if we believe the geomechanical model presented can describe the geomechanical setting and the resulting seafloor subsidence.

(a) Adapted input u_z
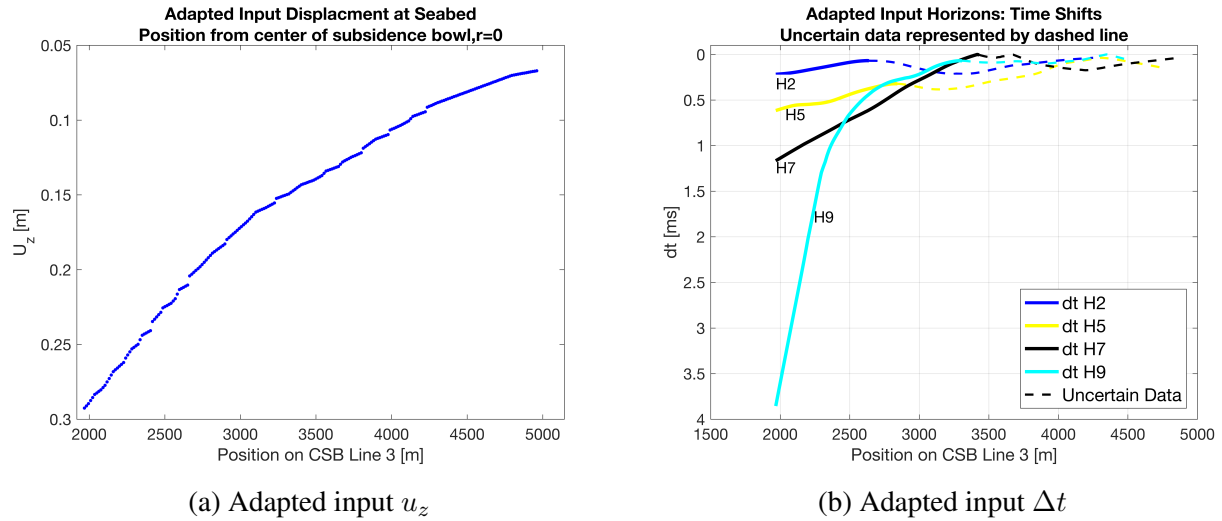
(b) Adapted input Δt

Figure 5.14: Adapted input displacement (u_z) and time shifts (Δt) with new initiation point for the inversion process at $r = 1968$ m

The inversion process with the model space from Table 5.8 resulted in the best model parameters shown in the header of Figure 5.15; $K = -1$ m, $D = 2500$ m and $R = 1000$ m. The resulting elements of the error function are given in Table 5.9, and we can see that the error is slightly increased compared to the process from Section 5.1, using data from the center of the subsidence bowl $r = 0$.

Parameter	Range	Discretization Δ
K [m]	[-0.1, -2]	-0.2
R [m]	[500, 5000]	500
D [m]	[500, 5000]	500

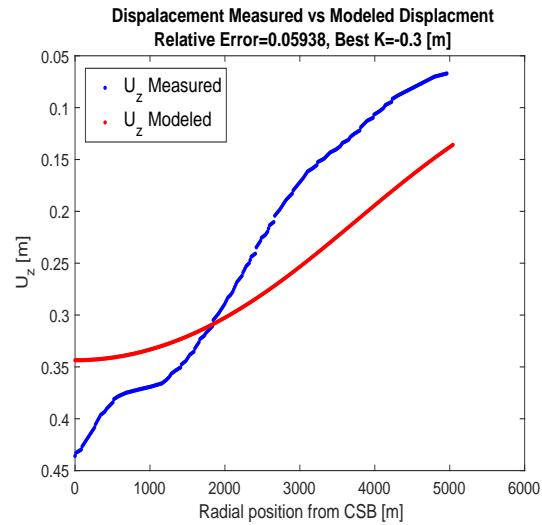Table 5.8: Model space used in the adapted global inversion process for model parameters K, R and D

Figure 5.15: Measured displacement (blue) compared to modeled displacement (red), from the adapted inversion process for K, R and D

Element of Error Function	Value [fraction]
$\chi^2_{U_z}$	$1.4 \cdot 10^{-3}$
$\chi^2_{\frac{\Delta T}{T}}$	$7.4 \cdot 10^{-33}$

Table 5.9: Value of the elements within the error function with input values for the factor K, R and D from Table 5.8

Layer 2 and 3 presented in Figure 5.16 show fairly stable modeled $\mathcal{R}$-factor values around $\mathcal{R} \approx 1$, notice the Y-axis limit is different due to the lower $\mathcal{R}$-values, to be able to show the effects better. Since the best-modeled reservoir depth is $D = 2500$ m, layer 4 will be partly above and beneath the modeled reservoir position causing strictly negative $\mathcal{R}$-factor values as we also got in the inversion process shown in Section 5.1. Changing the point of largest displacement from $r = 0$ to $r = 1968$ m, essentially meant that more of the seismic data are now associated with the larger displacements close to what is estimated as the center of the subsidence bowl.

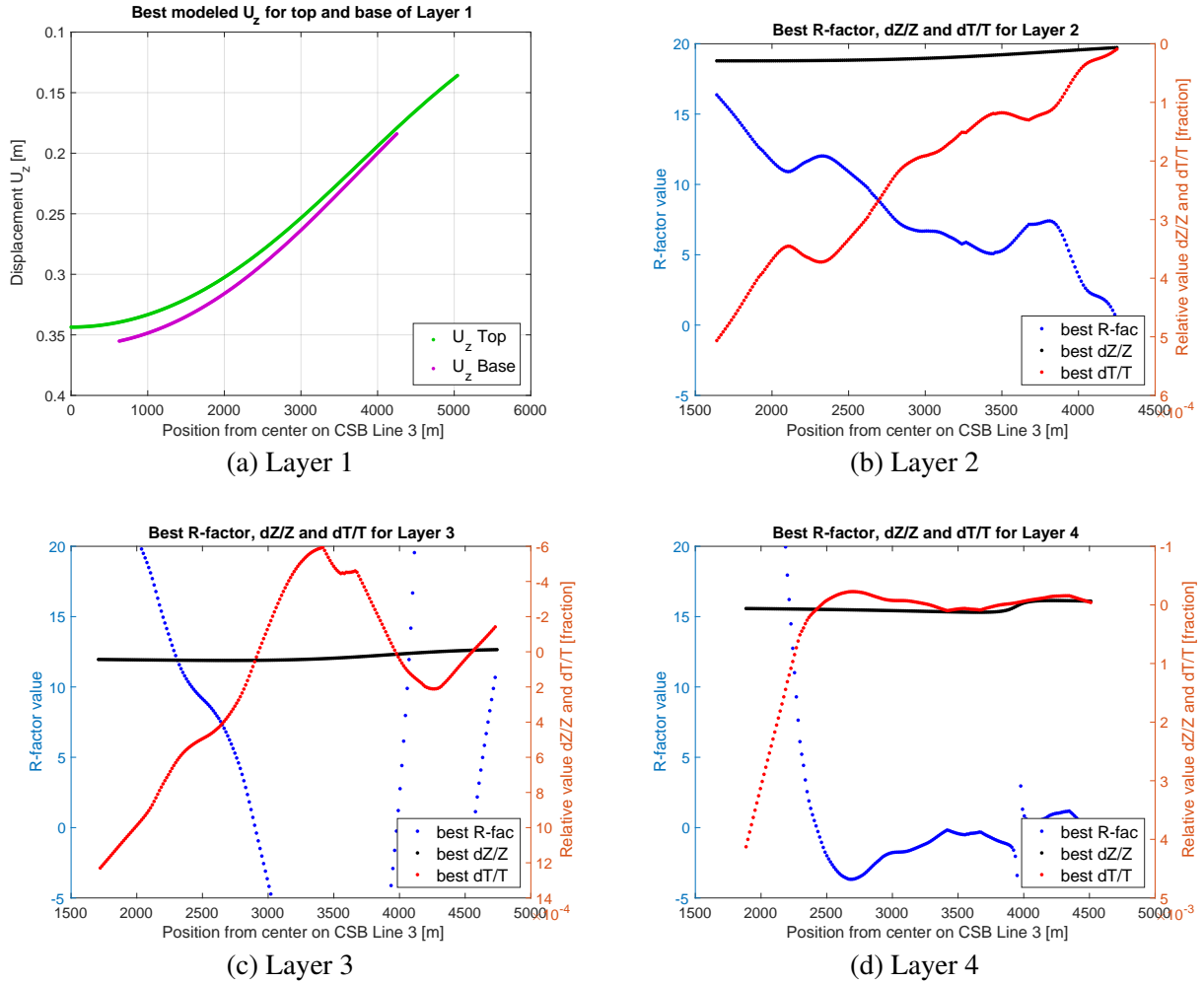(a) Layer 2   (b) Layer 3
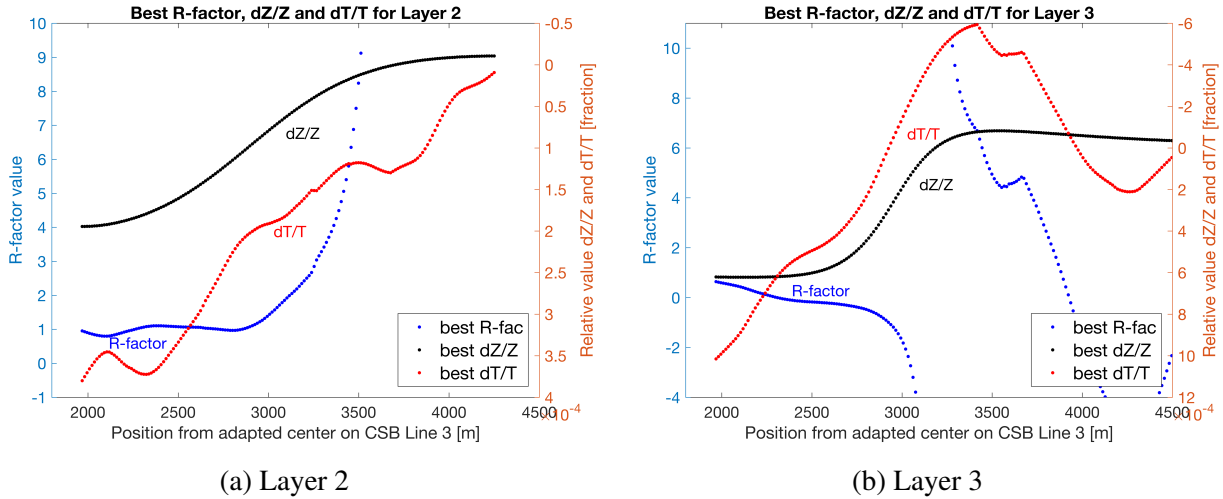
Figure 5.16: Modeled best $\frac{\Delta T}{T}$, $\frac{\Delta Z}{Z}$ and resulting $\mathcal{R}$-factor with position from the center of the subsidence bowl, from the adapted inversion process for K, R and D. Right Y-axis for the relative changes, and left Y-axis for $\mathcal{R}$-factor values up to 10

The negative $\mathcal{R}$-factor values in layer 4 are caused by the modeled negative relative thickness change marked by the yellow limit from Figure 5.17a. The color bar limit is cut at $\mathcal{R} = 3$ to better illustrate the variation in $\mathcal{R}$, until position larger than the $\frac{\Delta T}{T}$- and $\frac{\Delta Z}{Z}$-limit. The limit is more evident from Figure 5.17b, where we see the reservoir is modeled to be situated within layer 4. The reservoir is illustrated by the dashed black line. In order to mirror the displacements from the process, $r = 0$ in Figure 5.17b refer to $r = 1968$ m.
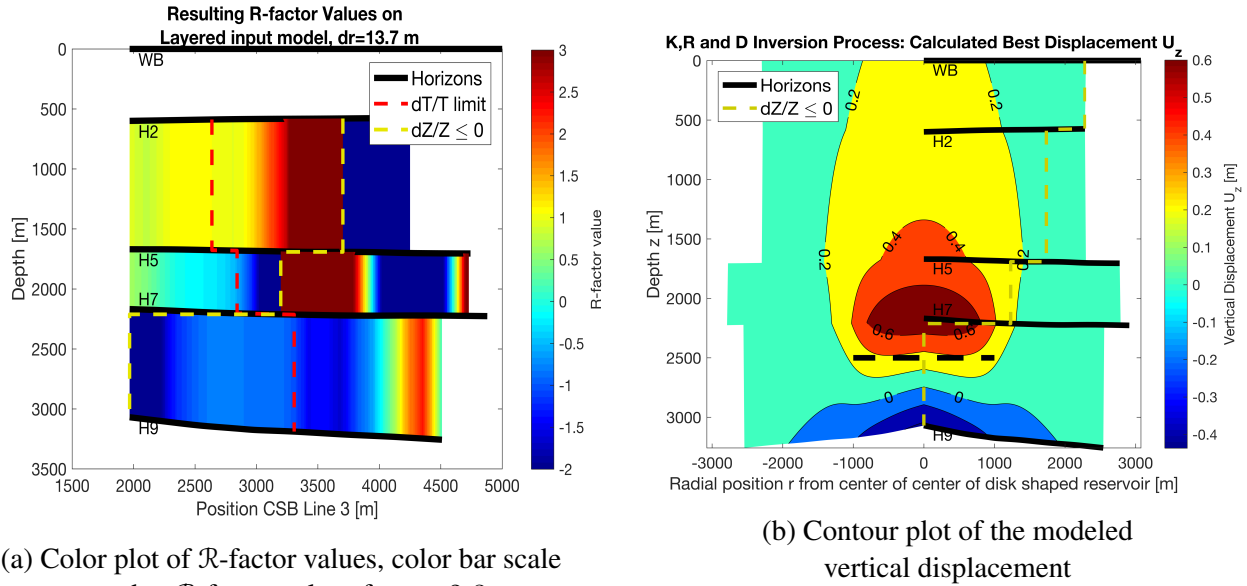
(a) Color plot of $\mathcal{R}$-factor values, color bar scale compressed to $\mathcal{R}$-factor values from -2-3

(b) Contour plot of the modeled vertical displacement

Figure 5.17: Color plot of modeled $\mathcal{R}$-factor values from the adapted inversion process for K, R and D, with trust limits for $\frac{\Delta T}{T}$ (red) and limit for $\frac{\Delta Z}{Z}$ (yellow). Displacement plot used to show the $\frac{\Delta Z}{Z}$-limit

5.4.1 Reservoir Depth Kept Constant

A second attempt to get more realistic values for the overburden layers using constant reservoir depth at $D = 3300$ m was performed, this time using the adapted input data presented in Section 5.4.

Parameter	Range	Discretization Δ
K [m]	[-0.1, -1.5]	-0.1
R [m]	[250, 3500]	250

Table 5.10: Model space used in the adapted global inversion process for K and R, constant depth at $D = 3300$ m

The errors associated with inversion process increased compared to when D was included as a model parameter, see Table 5.11 and Figure 5.18, as we also got for the process presented in Section 5.2. The best model parameters are now $K = -1.5$ and $R = 1000$ m, which produce a displacement curve at the seafloor shown in Figure 5.18.

89

Figure 5.18: Measured displacement (blue) compared to modeled displacement (red), from the adapted inversion process for K and R

Element of Error Function	Value [fraction]
$\chi^2_{U_z}$	$3.7 \cdot 10^{-3}$
$\chi^2_{\frac{\Delta T}{T}}$	$1.8 \cdot 10^{-33}$

Table 5.11: Value of the elements within the error function with input values for the factor K and R from Table 5.10

Figure 5.19 shows the modeled displacement in layer 1 and the resulting $\mathcal{R}$-factor values for the remaining layers, together with the associated relative thickness- and relative time shifts. Layer 2 shows $\mathcal{R}$-factor values fairly constant around 2.5-3. Along the $\frac{\Delta T}{T}$-curve for layer 2 we see two areas of increasing relative time shifts different from the overall decreasing trend. These coincide with the increasing $\mathcal{R}$-factor values outside the trend around 2.5-3. Notice how the $\mathcal{R}$-factor increase much faster for the area of increasing relative time shifts where $\frac{\Delta Z}{Z}$-curve is closer to zero. For layer 3 and 4 we have decreasing $\mathcal{R}$-factor values until position larger than the underlying reservoir, where $\frac{\Delta Z}{Z}$ becomes small and the calculation unstable.

(a) Layer 1

(b) Layer 2

(c) Layer 3

(d) Layer 4
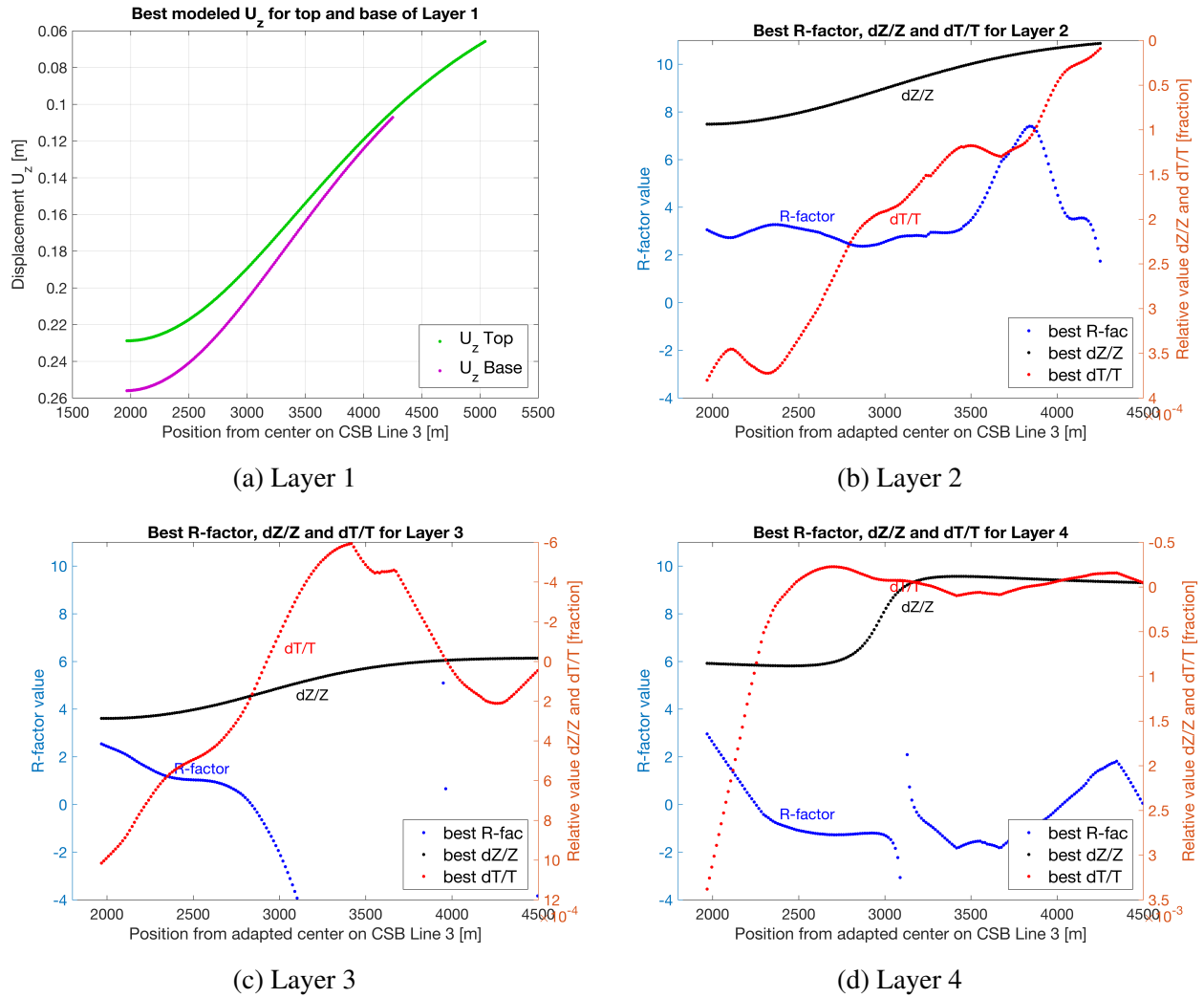
Figure 5.19: Modeled best $\frac{\Delta T}{T}$, $\frac{\Delta Z}{Z}$ and resulting $\mathcal{R}$-factor with position from the center of the subsidence bowl, from the adapted inversion process for K and R. Right Y-axis for the relative changes, and left Y-axis for $\mathcal{R}$-factor values up to 10
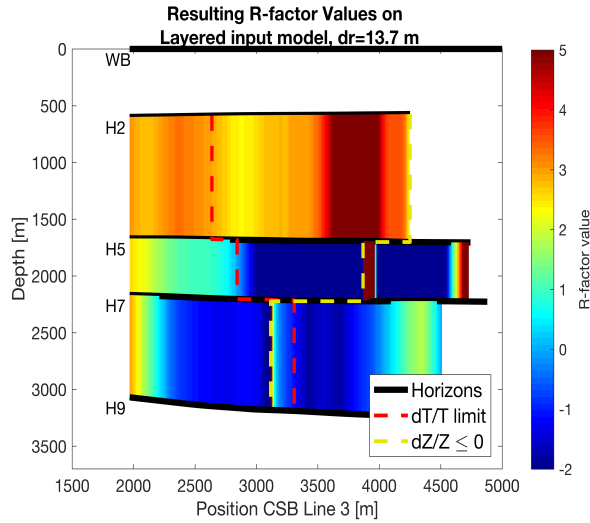
(a) Color plot of $\mathcal{R}$-factor values
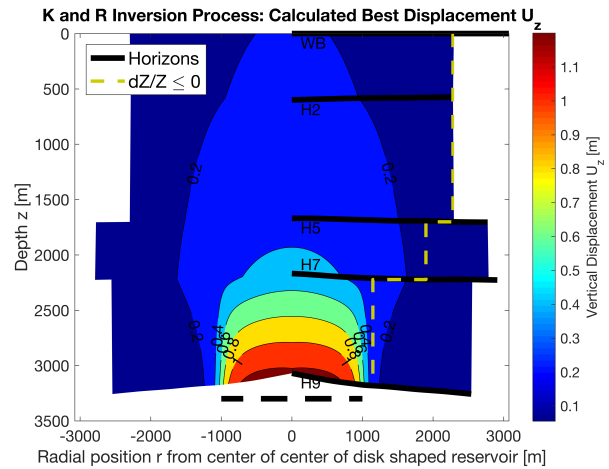
(b) Contour plot of the modeled vertical displacement

Figure 5.20: Color plot of modeled $\mathcal{R}$-factor values with trust limits for $\frac{\Delta T}{T}$ (red) and limit for $\frac{\Delta Z}{Z}$ (yellow), from the adapted inversion process for K and R. Displacement plot used to show the $\frac{\Delta Z}{Z}$-limit

From the color plot in Figure 5.20a we see the $\mathcal{R}$-factor variations with position and with depth. Keeping $D = 3300$ m led to the $\frac{\Delta Z}{Z}$-limit being drawn at increasing position, see Figure 5.20b. Resulting in limited positive $\mathcal{R}$-factor values for layer 4 compared to only negative as we saw from Figure 5.17a. The $\mathcal{R}$-factor values are decreasing as we see from Figure 5.20a, and ultimately becomes negative. The color bar has been cut at $\mathcal{R} = 5$ to better illustrate the subtle $\mathcal{R}$-factor variations.

Chapter 6

Discussion

The inversion processes presented in Ch. 3, with the ultimate goal to model the $\mathcal{R}$-factor values of the Ekofisk overburden, has been performed with all available data after the corrections performed in Ch. 4. The error analysis performed on synthetic data from the specialization project Kvilhaug (2016), showed an improvement in the definition and robustness of the global minimum when utilizing increasing amount of radial information. In the synthetic study, the radial information needed to exceed the radius of the reservoir to get a clear elliptical shaped error function. As we analyze more data with position larger than the reservoir radius, the time shifts and displacements will be smaller, and the associated error related to the data will make up a larger fraction of the underlying data. The data collected along CSB Line 3 exceed the area where we have a pressure reduction, but not by a substantial amount. Where we have a pressure reduction within the reservoir, is where we intuitively should expect the extent of the calculated reservoir radius to be, see Figure 4.19.

The results from the inversion process, presented in Ch. 5, reveal a different story. The inversion process with factor K, reservoir radius R and reservoir depth D as model parameters, resulted in the lowest error function value after running the "KRD"-inversion process summarized in Table 6.1. These model parameters provide the best fit against the observed displacement at the seafloor and the relative time shifts. For each of the three inversion processes, the relative error in displacement at the seafloor is the dominating element of the resulting error function value. The measured

relative time shifts are used together with the modeled relative thickness change to calculate the $\mathcal{R}$-factor. The modeled relative time shifts calculated using these $\mathcal{R}$-factors will, therefore, be almost identical, and the dominating element of the error function is hence the displacement term.

The best fit subsidence was achieved through inversion process 1 with K, R, and D as model parameters, even though the resulting best model parameters were not what was expected from the rough estimates in Table 4.4. The contour plot of the error function associated with the inversion process in Figure 5.2b show a clear minimum, but with 0.01 contour levels, indicating that we are dealing with a subtle minimum. The stretched elliptical shape of the error function contours between the model parameters R and D indicate that they are both important factors with an equal influence on the error function.

Inversion Process	Model Parameter	Value [m]
1: KRD	Best K	-0.5
	Best R	2250
	Best D	2500
2: KR	Best K	-1.05
	Best R	1750
3: K	Best K	-0.3

Table 6.1: Best model parameter values after the initial three inversion processes from $r = 0$

The attempt to push the inversion result towards the correct depth led to an error function with a minimum worse defined than before. The shape of the error function contours between the model parameters R and K reviled an inner contour stretched across a larger model space than on the error function contours between R and D. Since K is only present outside the equations as a scaling factor, see Eq. 3.7, the inversion process that relies on R and K, will not have the chance to shape the displacement curve as much as with D as a factor as well. The difference becomes apparent when comparing the resulting minimum of the error functions, especially when the inversion process relies on only one model parameter, the factor K.

From the attempts to estimate the $\mathcal{R}$-factor values, we gain an understanding of the dynamics between the elements incorporated into the equation of the dilation factor, Eq. 3.9. From the equation, it becomes clear that $\frac{\Delta Z}{Z}$ close to zero will cause very high $\mathcal{R}$-factor values and instabilities in the estimate. A ratio less than 1 would produce negative $\mathcal{R}$-factor values, which in this setting would not be expected.

From Section 4.5 the issue of imaging in the shallow part of the subsurface was mentioned. The representative seismic line used for the analysis (Figure 4.20a), did not have a clear pickable water bottom reflector due to the dominance of far offset traces in the shallow part. The time strains for the first layer was, hence, not possible to calculate without including the water layer. Due to the dominance of far offset traces in the shallow part of the final stack, lateral velocity differences compared to vertical may also overrepresent the resulting extracted time shifts. For these two reasons, the calculated $\mathcal{R}$-factor for layer 1 would be associated with more error than the layers below and is, hence, left out of the study.

The time shifts extracted from the representative seismic line are continuously positive and increasing towards the top reservoir horizon. The relative time shifts produced are, hence, also mostly positive within the trust limit of the time shifts, presented at the end of Ch. 4. Except for layer 4, where the decrease in time shifts are quicker for the base of layer (H9) than from the top of the layer (H7) causing negative relative time shifts around $r = 2500$ m. Positive $\frac{\Delta T}{T}$ require also the right side of Eq. 1.2 to be positive, where $\frac{\Delta Z}{Z}$ is usually much smaller than $\frac{\Delta V_p}{V_p}$. Since the $\mathcal{R}$-factor relating the two from Eq. 1.3 by definition is positive, we need $\frac{\Delta V_p}{V_p} < 0$ and $\frac{\Delta Z}{Z} > 0$ or $\frac{\Delta V_p}{V_p} > 0$ and $\frac{\Delta Z}{Z} < 0$ to withhold the statement. By combining the two as shown in Eq. 3.4, $\frac{\Delta Z}{Z}$ need to be positive, which in the end produce Eq. 3.9, used in this project to calculate the $\mathcal{R}$-factor. Since we in the area of study have almost only positive relative time shifts, we will also expect almost only positive relative thickness changes. From the $\mathcal{R}$-factor color maps the location of the $\frac{\Delta Z}{Z} \leq 0$ limit is defining the position where this statement does not hold. From the same plots, the limit of trustworthy relative time shifts, $\frac{\Delta T}{T}$, are also shown.

We can from the color plots Figure 5.5a, 5.10a and 5.13a, see a gradual increase in $\mathcal{R}$-factor values when $\frac{\Delta Z}{Z}$ approach the limit. The contour plots of vertical displacement are illustrating the corresponding geomechanical setting of the overburden, providing a better understanding of where these

limits are drawn. We can see that towards the end of the lateral extent of the reservoir, at reservoir level, the vertical displacement contours a closer drawn, see Figure 5.5b, 5.10b and 5.13b. From the introduction of the method, we saw how the radial displacement increased towards the edge of the reservoir in agreement with the expected arching effect above a depleting reservoir, see Figure 2.5-2.7.

Due to the shape of these contour lines, it becomes apparent that the relative thickness value will become small and ultimately negative quickly as we move outside the reservoir zone. The contour lines are here almost vertical, resulting in nearly no contrast in displacement between base and top of the layer. The shape of the contours can also lead to a larger displacement at the top of the layer than at the base. To be able to detect a difference in displacement between top and base layer implies that the thickness of the layer also plays an important part when calculating these relative thickness changes. The layers can not be too thin, in order to detect a change in displacement, but if we are in an area with almost vertical contour lines, the thickness will not be meaningful. The inversion processes presented in this project was also run on a three layered overburden, adapting layer 3 to be part of either layer 2 (excluding first Horizon 5) or layer 4 (excluding first Horizon 7). The results were not significantly different than what was presented in Ch. 5 and have therefore been left out. Landrø and Stammeijer (2004) formulated Eq.1.2 based on horizontal layers with constant thickness. The correction term formulated for dipping layers can be neglected for subtle dips as present at Ekofisk ($\approx 5^o$) (Landrø and Stammeijer, 2004). When the thickness variation results in a difference above 100 m, as we see for layer 4 in Figure 4.32, the difference might point towards a more influential factor and may result in instabilities in the calculated relative thickness change.

Figure 5.4, 5.9 and 5.12 illustrates the calculated $\mathcal{R}$-factor values together with the corresponding $\frac{\Delta Z}{Z}$ and $\frac{\Delta T}{T}$ for the particular layer. The only two layers with fairly constant calculated $\mathcal{R}$-factor is layer 2 and 3 from Figure 5.4, with $\mathcal{R} \approx 5$. This only holds for about 500 m until the position is larger than the calculated reservoir radius, and the $\mathcal{R}$-factor values increases drastically due to the low value of $\frac{\Delta Z}{Z}$. Where the calculated $\mathcal{R}$-factor values are constant, implies that the ratio between relative thickness changes and relative time shifts are constant with increasing position. For most of the other layers, this is not the case. The resulting calculated $\mathcal{R}$-factor through this model is highly

dependent on the choice of model parameters. The selection of for instance low best radius R is causing the values to become very large, when performing the calculation with position larger than the reservoir radius. Particularly for the deeper layers, where the displacement contours are closer spaced and $\frac{\Delta Z}{Z}$ approach zero faster. Due to the SOA, the initiation of most of the data collected, is in the area of the modeled best radius. At the position of the modeled reservoir radius, is where we expect the $\frac{\Delta Z}{Z}$ quickly to approach zero, and the resulting $\mathcal{R}$-factor values will not be particularly trustworthy.

An attempt to improve the calculated $\mathcal{R}$-factor values were performed, by moving the initiation point of the inversion process to where most of the seismic data start. The new adapted center of subsidence was at $r = 1968$ m relative to $r = 0$ as the previous results refer to as the center of subsidence. The new initiation point was outside the extent of the shadowing effect by the SOA. The best model parameters after running the inversion process with three- and afterward two model parameters are summarized in Table 6.2. The inversion process with lowest error value was also here associated with best-modeled depth at $D = 2500$ m. So an attempt to locking the reservoir depth was performed, but with increasing error as a result.

Inversion Process	Model Parameter	Value [m]
4: KRD	Best K	-1
	Best R	1000
	Best D	2500
5: KR	Best K	-1.5
	Best R	1000

Table 6.2: Best model parameter values after inversion processes with moved initiation point to $r = 1968$ m

The resulting errors associated with the two adapted procedures increased, compared to the inversion processes constrained by displacement and relative time shifts from $r = 0$. The calculated $\mathcal{R}$-factors were although much more stable due to the increasing amount of data above the modeled reservoir radius extent. Most stable with increasing position for Layer 2 showing $\mathcal{R}$-factor values

around $\mathcal{R} \approx 1$ and $\mathcal{R} \approx 3$, when locking the reservoir depth at $D = 3300$ m. The same effects of unstable $\mathcal{R}$-factor calculations appear for increasing position greater than the extent of the reservoir radius R. Pointing towards the importance of collecting data from right above the center of the subsidence bowl, where we expect the 4D effects to be largest, both from seismic data and from geomechanical modeling.

Since the $\mathcal{R}$-factor is a biased model parameter; it will be dependent on the accuracy of the other model parameters. The resulting best model parameters for R, D and K provide an indicator of the trustworthiness of the corresponding dilation factor $\mathcal{R}$ for the overburden. Each set of model parameters will represent a modified geomechanical setting for the overburden. They are bound by the same displacement at the seafloor and relative time shifts within the overburden, but when the inversion processes come up with such different best model parameters, it becomes hard to compare the resulting $\mathcal{R}$-factor values.

Because the lowest value of the error function corresponds with such different model parameters than expected, there have to be factors not taken into consideration within the geomechanical model. The inversion process corresponding with the lowest error value and best definition of the error function is the one including all three model parameters K, R and D. The expected model parameters for the inversion process including all available data, presented in Table 4.4, are rough estimates. But we know that the depth of the reservoir should lie between $2900 - 3300$ m. So when both the adapted- and the inversion process including all the data from $r = 0$, calculate the best reservoir depth at $D = 2500$ m, and the resulting error increases after locking the depth at $D = 3300$ m. It becomes apparent that the geomechanical model with the available input parameters is not able to describe the displacement at the seafloor. It is hard, based on the constrains of the geomechanical model, to define the underlying "real" R and K parameter, since they will not reflect the complexity of the Ekofisk reservoir.

In this inversion process, there are several factors that all affect the credibility of the results. As mentioned in Ch. 1, the geomechanical model by Geertsma (1973), is based on a disk-shaped reservoir experiencing constant pressure depletion, situated within a linear-elastic, homogeneous and isotropic half space. The assumption of homogeneity will require both the reservoir and the overburden to have the same elastic properties, implying constant mean stress above the reservoir

($\gamma_V + 2\gamma_h = 0$). From Ch. 4 we know the Ekofisk dataset does not meet these requirements. With a clay-rich shaley overburden section with different elastic properties than the highly porous chalk reservoir rock, will cause alterations in the stress fields and move away from pure shear loading associated with $\gamma_V + 2\gamma_h = 0$, and potentially rather have an increasing stress arching coefficient γ_V. A study done by Holt et al. (2016) found that stress arching ($\gamma_V > 0$) is increasing with increasing elastic contrast and with increasing tilt. The same study done by Holt et al. (2016) presented lab measurements from ultrasonic core measurements on shales, concluding a definite increase in stress sensitivity and hence $\mathcal{R}$-factor values with increasing stress path κ, defined in Ch. 2. The increasing trend is due to the increasing stiffness $\frac{\Delta\sigma_z}{\epsilon_{zz}}$ of the rock with increasing stress path κ. Where ϵ_{zz} is the resulting axial strain to the change in axial stress $\Delta\sigma_z$ (Holt et al., 2016). This dependence indicates that the $\mathcal{R}$-factor values will vary with depth, as Bathija et al. (2009) also concluded. Bathija et al. (2009) found that absolute values of $\mathcal{R}$ increased for sandstones and decreased for shales with decreasing confining pressure. So operating with one constant value of $\mathcal{R}$ from the surface, where we have unconfined stress state, to the reservoir where we have higher confined stress state, should be avoided.

The overburden consists mostly of clay-rich shales with minor lithological changes (Nagel, 1998). Intrinsic anisotropy is typical for the laminated shale lithology, where clay minerals tend to be aligned. Due to production related change in stress regime, extrinsic anisotropy has also been reported as a significant effect (Hawkins, 2008). Extrinsic anisotropy is superimposed on the intrinsic lithological anisotropy of the shale. Extrinsic anisotropy refers to the stress induced anisotropy resulting from alteration of grain contact, cracks, and fractures. Holt et al. (2005) concluded that porosity was the main factor representing how stress dependent the velocities were within shales. When the overburden is stretched, the grain contact will be altered and hence the shape of the pores. Secondary porosity from cracks/fractures may also be generated, and all these factors influence the velocities. The result of the study by Røste et al. (2006) indicated that time-lapse changes in anisotropic parameters as low as 1%, would cause severe errors in estimated overburden thickness change and velocity changes. This is a factor in which the geomechanical model used in this project does not take into account.

A disk-shaped reservoir will not be fully applicable for the shape of the Ekofisk reservoir, inferred from the pressure map 4.6. The analytic solution of the resulting subsidence used in this project is based on symmetry, where one representative vertical section is used to represent the displacement above the disk-shaped reservoir in a three-dimensional space. From the average pressure change and time shifts shown in Figure 4.13, we see that the seismic line chosen can not be considered representative for the whole reservoir. To incorporate the complexity of the reservoir, we would have to shift from the analytic solution represented by the homogeneous depleting disk-shaped reservoir and rather compartmentalize the reservoir with different depletion schemes. Which in turn can be used to model the time shifts and displacements of the overburden. Numerical techniques based on the discrete element method is a common technique in more sophisticated geomechanical models.

From the pressure map in Figure 4.6 we see a complex picture of pressure increase and decrease. As a result of the full-scale water flooding of the reservoir. The injection of water has reduced the subsidence rate as a response to the average reservoir pressure increase, see Figure 2.3. As stated in Section 2.1, the continuing reservoir compaction and subsidence today is associated with the balance between the ongoing repressurization of the reservoir and the water weakening of chalk. Depending on the particular stress state within the reservoir, we will expect fractures to form and grow in various direction due to water injection (Alassi et al., 2010). The complex fault network shown in Figure 4.3, will most likely be altered during water injection, due to the induced alteration of the stress regimes. Reactivation of faults in the surrounding rock mass has been reported as an effect of depletion and increasing effective stress within the reservoir (Segall and Fitzgerald, 1998). The more faulted section within the Hordaland Gp. is hence most likely to experience these effects.

Induced fractures and fault reactivation are all heterogeneities which will affect the seismic velocities above and within the reservoir. As Kenter et al. (2004) pointed out in their geomechanical model; many reservoir variations in for instance thickness, pore pressure or rock compressibility show up in the overburden as time shifts. The underlying reason they proposed, was that the effects are inducing stress arching. When comparing the time shift map from the top reservoir with the average change in pore pressure, we saw how most of the negative time shifts coincide with an increase in mean pressure. And the area of positive time shifts was associated with the area of

average pressure decrease. These trends propagated up into the overburden with decreasing magnitude for areas of both positive and negative time shifts, as we saw from Figure 4.27 and 4.28. It is more difficult to reason why we should see a continuation of negative time shifts for the overburden compared to the main effect of positive time shifts for depletion, a pressure increase in the reservoir would decrease the effective stress and result in negative relative velocity change within the reservoir. The top reservoir horizon will at most remain still and not further compact; it is not considered to be possible to lift the top reservoir horizon due to water injection. These areas of pressure increase nearby areas of pressure decrease could rather be such stress attractors which Kenter et al. (2004) reported in their study. The study looked at reservoir compartments with different pore pressure, which showed up as sharp transitions from positive to negative time shifts, causing increasing stresses and velocities, resulting in negative time shifts. The increasing pore pressure within the reservoir might cause the compaction to occur at an other level in the overburden rather than in the reservoir, resulting in negative overburden time shifts.

The reactivation of faults and the change in stress state in the overburden, may also cause pore pressure changes within the overburden. Since overburden shales have such low permeabilities the resulting stress changes as a result of pressure alteration within the reservoir, occur without draining the rock on a short term. Ongoing research by Holt (2017) on pore pressure change in overburden indicates that the resulting velocity changes within the overburden are affected by three main factors, together with the driving mechanism of the reservoir pore pressure change; the in situ stress path κ, the stress sensitivity of the rock and the Skempton parameters (Skempton, 1954), which quantify the pore pressure changes. The laboratory experiments by Holt (2017) indicate that the pore pressure evolution associated with the in situ stress path have a significant impact on the seismic traveltimes, and hence changes in these stress paths with time will cause detectable effects on the seismic time shifts.

Throughout this project, the time shifts used has been extracted from full-offset stacked data. Since we are operating with displacements in the vertical direction, ideally we should use zero-offset time shifts. The full stack is used to improve the signal-to-noise ratio. The non-vertical ray paths in the full stack will influence the time shifts depending on anisotropy in the penetrated layers. A large difference in vertical and lateral velocities will cause the corresponding far offset time shifts

to be influenced by different velocities than the zero incidence angle time shifts. These non-vertical ray paths may hence detect different 4D responses than the zero offset time shifts due to the large incidence angles (Røste and Ke, 2017).

Chapter 7

Conclusions

The global inversion process presented in this master's thesis provide the $\mathcal{R}$-factor values for the overburden as a biased model parameter. The resulting $\mathcal{R}$-factor values will hence be affected by the accuracy of the other reservoir parameters in which the model define. These reservoir properties determine the resulting displacements within the overburden through the geomechanical model used. The displacement at the seafloor, together with the recorded relative time shifts, constrained the inversion process. The corresponding model parameters associated with the best fit seafloor displacement, and relative time shifts, do not reflect the underlying Ekofisk reservoir in which it tries to represent. The lowest error function value and best definition of the minimum were achieved when including all three model parameters K, R and D, with best model parameter values $K = -0.5$, $R = 2250$ and $D = 2500$ m.

Since the geomechanical model is based on a uniformly depleted disk-shaped reservoir, situated within a linear-elastic, homogeneous and isotropic half space, it was difficult to define the underlying "real" R and K parameter since they will not reflect the complexity of the Ekofisk reservoir. Still, we know that the reservoir depth D lie between 2900-3300 m, so a modeled best $D = 2500$ m indicates that the calculated $\mathcal{R}$-factor values will be associated with errors. An attempt to lock D at the known reservoir depth only increased the error function value, decreased the sensitivity of the error function and decreased the definition of the error function minimum. The calculated $\mathcal{R}$-factor values associated with the lowest error function value were at $\mathcal{R} \approx 5$ for layer 2 and 3 until the

calculation turned unstable at the edge of the underlying modeled reservoir radius R.

The data presented from the Ekofisk Field show large areas of negative time shifts from the overburden. The full field water injection is believed to have altered the stress paths of the overburden, and from Ch. 5, we got indications that the real geomechanical setting from the Ekofisk Field is not the constant mean stress associated with the Geertsma model for a uniformly depleted reservoir. So even though the study was performed on a representative 2D seismic line with increasing positive mean time shift with depth, as presented in Ch. 4, it seems like the constraining displacement together with the relative time shifts do not reflect the simplified stress paths calculated from Geertsma's geomechanical model. The model will calculate smooth displacement curves, and will not be able to describe the complexities of the real geomechanical setting. The calculated $\mathcal{R}$-factor values will, hence, also be smoothed and we will not be able to describe the potential depth- and lateral variations.

Despite the resulting $\mathcal{R}$-factor values are inaccurate, the study illustrates the interaction between $\frac{\Delta Z}{Z}$ and $\frac{\Delta T}{T}$ factors incorporated within the equation of $\mathcal{R}$. The study shows how the most stable calculations were obtained using data collected right above the center of the subsidence bowl, where we expect the 4D effects to be largest, both from seismic data and from geomechanical modeling. Due to the SOA, we do not have seismic data in this area. Most of the seismic data in this study were available at position $r \approx 2000$ m from the center of the subsidence bowl, which resulted in unstable calculated $\mathcal{R}$-factor values, since the extent of the modeled underlying reservoir radius was in the same area.

The improvement of utilizing data right above the center of the subsidence bowl was shown for the adapted inversion process. Where the center, or the initiation point, of the inversion process, was moved to where most of the seismic data start. And using the corresponding displacement points, and relative time shifts, from the new center as constraining data. The adapted inversion process resulted in relatively stable calculated $\mathcal{R}$-factor values in the overburden, above the extent of the reservoir. Most stable with increasing position for Layer 2 showing $\mathcal{R}$-factor values around $\mathcal{R} \approx 1$ and $\mathcal{R} \approx 3$, when locking the reservoir depth at $D = 3300$ m. Increasing position larger than the underlying modeled reservoir radius, lead to $\frac{\Delta Z}{Z}$ approaching zero, and instabilities in the calculation of $\mathcal{R}$. The instabilities are shown to be dependent on depth, and the effect occurs at a

larger position for shallow- compared to deeper layers due to stress arching.

The calculated $\mathcal{R}$ will depend on the stress path represented by the geomechanical model. Depending on the interaction with the seismic response, $\mathcal{R}$ can be different both laterally and with increasing depth. For a layer where the calculated $\mathcal{R}$-factor values are constant, it implies that the ratio between relative thickness change and relative time shifts are constant with increasing position. The study illustrates the importance of a geomechanical model which account for heterogeneities in the reservoir and overburden, together with non-elastic effects such as water weakening effects of chalk, fault reactivation, and anisotropy. These factors all affect the resulting seismic signal and should be taken into account when building a geomechanical model. The method still provides a good understanding of the processes involved, and the scientific approach can potentially be utilized with more sophisticated geomechanical models.

References

Alassi, H., Holt, R., and Landrø, M. (2010). Relating 4d seismics to reservoir geomechanical changes using a discrete element approach. *Geophysical prospecting*, 58(4):657–668.

Bathija, A. P., Batzle, M. L., and Prasad, M. (2009). An experimental study of the dilation factor. *Geophysics*, 74(4):E181–E191.

Bertrand, A., Folstad, P., Lyngnes, B., Buizard, S., Hoeber, H., Pham, N., De Pierrepont, S., Schultzen, J., and Grandi, A. (2014). Ekofisk life-of-field seismic: Operations and 4d processing. *The Leading Edge*, 33(2):142–148.

Bjorlykke, K. (2010). *Petroleum Geoscience: From Sedimentary Environments to Rock Physics*. Springer Berlin Heidelberg.

Chilingarian, G.V., D. E. Y. T. (1995). *Subsidence Due to Fluid Withdrawal*. Elsevier.

CoP (2010). Ekofisk Overburden Structural and Stratigraphic Interpretation. Internal Report by ConocoPhillips. [Recived by Sirikarn Narongsirikul September 2016].

Doornhof, D., Kristiansen, T. G., Nagel, N. B., Pattillo, P. D., and Sayers, C. (2006). Compaction and subsidence. *Oilfield Review*, 18(3):50–68.

Fjær, E., Holt, R. M., Raaen, A., Risnes, R., and Horsrud, P. (2008). *Petroleum related rock mechanics*, volume 53. Elsevier.

Folstad, P. (2010). Monitoring of the ekofisk field. *GEOExPro*, 7(3):72–74.

Geertsma, J. (1973). A basic theory of subsidence due to reservoir compaction: the homogeneous case. *Verhandelingen Kon. Ned. Geol. Mijnbouwk. Gen*, 28:43–62.

Guilbot, J. and Smith, B. (2002). 4-d constrained depth conversion for reservoir compaction esti- mation: Application to ekofisk field. *The Leading Edge*, 21(3):302–308.

Hatchell, P. and Bourne, S. (2005). Rocks under strain: Strain-induced time-lapse time shifts are observed for depleting reservoirs. *The Leading Edge*, 24(12):1222–1225.

Havmøller, O. Foged, N. (1996). Review of rock mechanics data for chalk. *Proc. 5th Joint Chalk Research Symposium*, Reims(France):7–9 October.

Hawkins, K. (2008). Defining the extent of the compacting elgin reservoir by measuring stress- induced anisotropy. *First Break*, 26(10).

Hermansen, H., Landa, G., Sylte, J., and Thomas, L. (2000). Experiences after 10 years of water- flooding the ekofisk field, norway. *Journal of Petroleum Science and Engineering*, 26(1):11–18.

Holt, R., Bauer, A., Bakk, A., and Szewczyk, D. (2016). Stress-path dependence of ultrasonic and seismic velocities in shale. In *SEG Technical Program Expanded Abstracts 2016*, pages 3159–3163. Society of Exploration Geophysicists.

Holt, R. M. (2017). [Private conversation related to ongoing research].

Holt, R. M., Nes, O.-M., and Fjaer, E. (2005). In-situ stress dependence of wave velocities in reservoir and overburden rocks. *The Leading Edge*, 24(12):1268–1274.

Kenter, C., Van den Beukel, A., Hatchell, A., Maron, P., Molenaar, K., Molenaar, M., Stammeijer, J., et al. (2004). Geomechanics and 4d: Evaluation of reservoir characteristics from timeshifts in the overburden. In *Gulf Rocks 2004, the 6th North America Rock Mechanics Symposium (NARMS)*. American Rock Mechanics Association.

Kvilhaug, A. (2016). Global inversion method for determining the dilation factor. *TPG4570*, Petroleumsgeofag, fordypningsprosjekt.

Landrø, M., Digranes, P., and Strønen, L. (2001). Mapping reservoir pressure and saturation changes using seismic methods-possibilities and limitations. *First break*, 19(12):671–684.

Landrø, M. and Stammeijer, J. (2004). Quantitative estimation of compaction and velocity changes using 4d impedance and traveltime changes. *Geophysics*, 69(4):949–957.

Luke, Y. (1962). Integrals of bessel functions. *McGraw-Hill*, page 314.

Mindlin, R. D. and Cheng, D. H. (1950a). Nuclei of strain in the semi-infinite solid. *Journal of Applied Physics*, 21(9):926–930.

Mindlin, R. D. and Cheng, D. H. (1950b). Thermoelastic stress in the semi-infinite solid. *Journal of Applied Physics*, 21(9):931–933.

Nagel, N. (1998). Ekofisk field overburden modelling. *Conference Paper*.

Narongsirikul, Sirikarn (2017). Lab data for Uniaxial compaction moduluds and Poissons ratio. Internal Data by ConocoPhillips. [Recived by Sirikarn Narongsirikul January 2017].

Nes, O.-M., Holt, R., Fjær, E., et al. (2000). The reliability of core data as input to seismic reservoir monitoring studies. In *SPE European Petroleum Conference*. Society of Petroleum Engineers.

NPD (2017). Ekofisk Field. http://factpages.npd.no/factpages/Default.aspx?culture=nb-no&nav1=field&nav2=PageView|All&nav3=43506. [Online; accessed 24-Mach-2017].

Ottemöller, L., Nielsen, H., Atakan, K., Braunmiller, J., and Havskov, J. (2005). The 7 may 2001 induced seismic event in the ekofisk oil field, north sea. *Journal of Geophysical Research: Solid Earth*, 110(B10).

Rickett, J., Duranti, L., Hudson, T., Regel, B., and Hodgson, N. (2007). 4d time strain and the seismic signature of geomechanical compaction at genesis. *The Leading Edge*, 26(5):644–647.

Røste, T. and Ke, G. (2017). Overburden 4d time shifts—indicating undrained areas and fault transmissibility in the reservoir. *The Leading Edge*, 36(5):423–430.

Røste, T., Stovas, A., and Landrø, M. (2006). Estimation of layer thickness and velocity changes using 4d prestack seismic data. *Geophysics*, 71(6):S219–S234.

Segall, P. and Fitzgerald, S. D. (1998). A note on induced stress changes in hydrocarbon and geothermal reservoirs. *Tectonophysics*, 289(1):117–128.

Sen, M. K. and Stoffa, P. L. (2013). *Global Optimization Methods in Geophysical Inversion:*. Cambridge University Press, Cambridge.

Skempton, A. (1954). The pore pressure coefficients a and bgeotechnique 4 (4) 143–7.

Smith, L. C., Smith, M., and Ashcroft, P. (2011). Analysis of environmental and economic damages from british petroleum's deepwater horizon oil spill. *Albany Law Review*, 74(1):563–585.

Sylte, J., Thomas, L., Rhett, D., Bruning, D., Nagel, N., et al. (1999). Water induced compaction in the ekofisk field. In *SPE Annual Technical Conference and Exhibition*. Society of Petroleum Engineers.

Tarantola, A. (2005). *Inverse problem theory and methods for model parameter estimation*. siam.

Appendix A

Nomenclature

Symbols

t	=	Seismic traveltime
Δt	=	Time-lapse time shift
T	=	Layered seismic traveltime
V_p	=	Seismic P-wave velocity
V_s	=	Seismic S-wave velocity
Z	=	Layer thickness
$\frac{\Delta T}{T}$	=	Relative time shift (Time strain)
$\frac{\Delta Z}{Z}$	=	Relative thickness change
$\frac{\Delta V_p}{V_p}$	=	Relative P-wave velocity change
$\mathcal{R}$	=	Dilation factor
$\Delta\sigma_{ij}$	=	stress component change
ϵ_{ij}	=	Strain component
$\Delta\sigma'_{ij}$	=	Effective stress component
Δp_f	=	Pore pressure change
α	=	Biot coefficient

K_{fr}	=	Framework Bulk modulus
K_s	=	Solids/grain Bulk modulus
K_f	=	Fluid Bulk modulus
ϕ	=	Porosity
$\bar{\phi}$	=	Average porosity
ϵ_{vol}	=	Volumetric strain
σ_p	=	External hydrostatic stress
σ_h	=	Minimum horizontal stress
σ_H	=	Maximum horizontal stress
σ_V	=	Vertical stress
G	=	Shear Modulus
E	=	Young's modulus
ν	=	Poisson's ratio
h	=	Reservoir height
R	=	Reservoir radius
C_m	=	Compaction coefficient
λ	=	Lamé's parameter
H	=	Plane wave modulus
δ_{ij}	=	Kronecker delta
β	=	Ratio between the rock matrix compressibility and the rock bulk compressibility
R_0	=	Initial radius
u_0	=	Radial displacement at surface
r	=	Radial position from center of depleting sphere/reservoir
$\vec{u}$	=	Displacement
$F(\alpha|m)$	=	Incomplete elliptic integral of first kind
$K(m)$	=	Complete elliptic integral of first kind
$E(\beta|m)$	=	Incomplete elliptic integral of second kind
$E(m)$	=	Complete elliptic integral of second kind
U	=	Unit step function

V	=	Element volume
$\hat{z}$	=	Unit vector in z-direction
D	=	Depth from surface to center of depleting sphere/reservoir
ρ	=	Density
ρ_w	=	Water density
ρ_o	=	Oil density
ρ_g	=	Gas density
ρ_s	=	Grain density
z	=	Vertical position from surface
z_{base}	=	Vertical position from surface down to base of the layer
z_{top}	=	Vertical position from surface down to top of the layer
I_i	=	Geertsma integrals
e	=	Aspect ratio
γ	=	Arching coefficient
κ	=	Stress path
S_i	=	Fraction of saturation, fluid component
m	=	Model parameters
d	=	Resulting parameters
g	=	Forward operator
χ	=	Relative error function component
Φ	=	Objective function
ϵ	=	Relative error matrix
N	=	number of indices
c	=	Weighting term
H_i	=	Horizon number
L_i	=	Layer number

Subscripts

g	=	Gas
o	=	Oil
w	=	Water
y	=	Y direction
x	=	X direction
z	=	Vertical direction
V	=	Vertical direction
r	=	Radial direction
fr	=	Framework
s	=	Solids/grains
f	=	Fluid

Acronyms

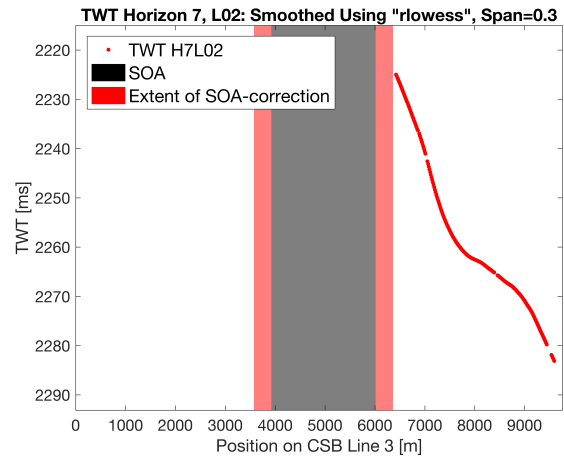|		
HSE	=	Health, safety and environmental
TWT	=	Two way traveltime
SOA	=	Seismic obscured area
NoE	=	Number of elements
NPD	=	Norwegian Petroleum Directorate
LoFS	=	Life of Field Seismic
CoP	=	ConocoPhillips
BP	=	British Petroleum
CSB	=	Center of Subsidence Bowl

Appendix B
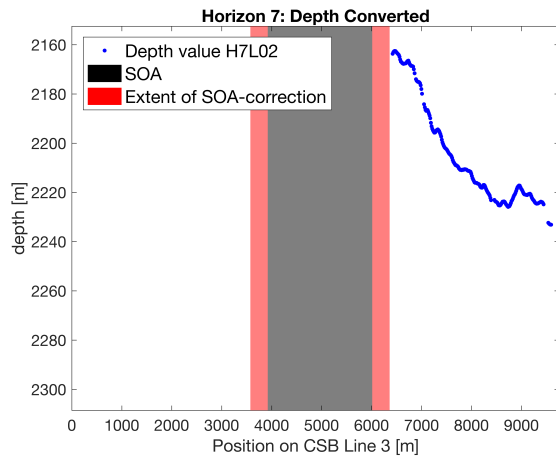
Data Preparation

B.1   Base TWT Measurement
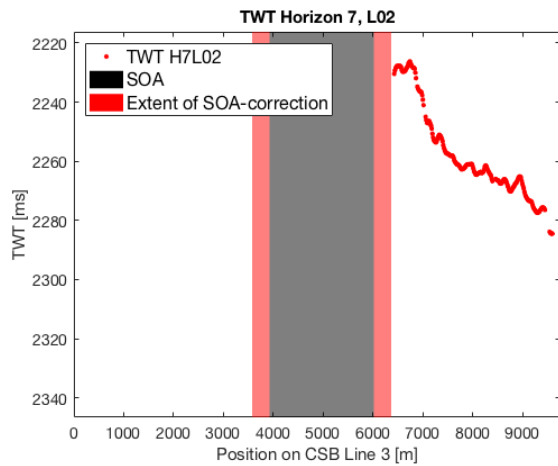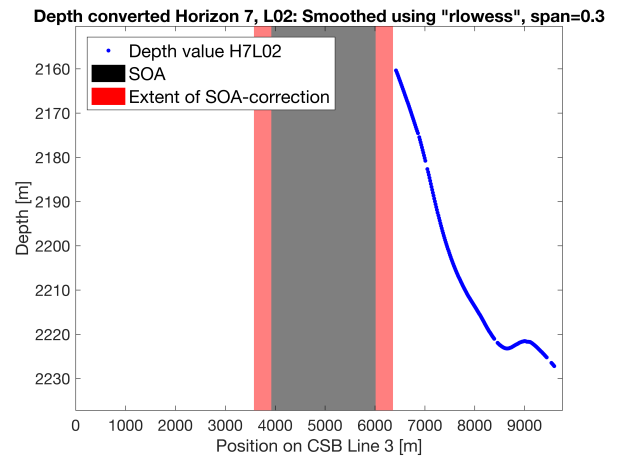

(a) Input time pick of H7 on base survey L02

(b) Smoothed time pick of H7 on base survey L02 used in iversion process

Figure B.1: Example of data preparation for base TWT measurements used to calculated $\frac{dT}{T}$

B.2   Initial Depth

(a) Input depth measurements
from depth conversion

(b) Smoothed depth measurements
used in inversion process

Figure B.2: Example of data preparation for initial depth measurements used to calculated $\frac{dZ}{Z}$
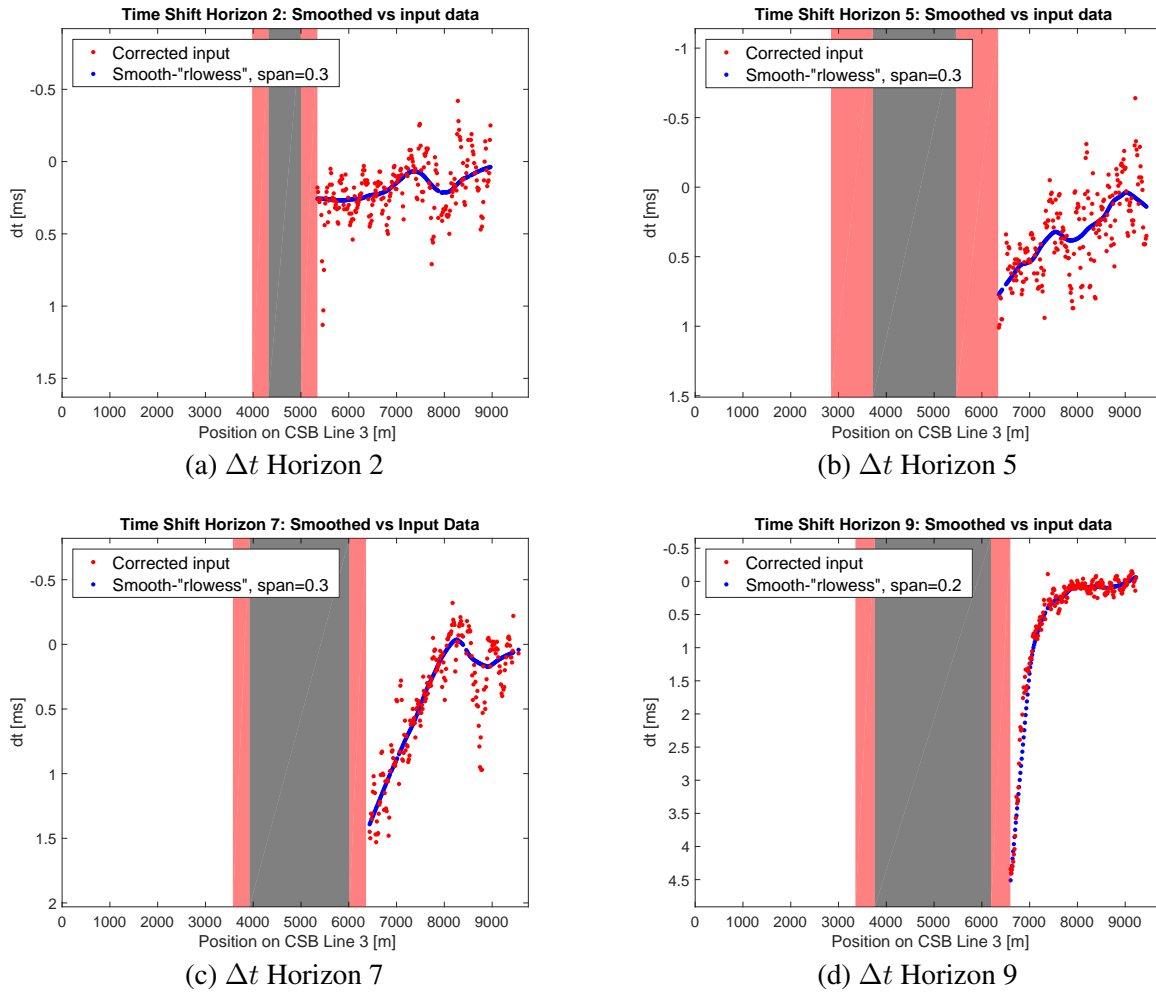
B.3 Time Shift Measurements and Smoothing

Figure B.3: Input measurements and resulting smoothed time shifts for horizons used in inversion

Appendix C

Geomechanics

C.1 Subsidence

$$I_1(q) = \frac{2}{\pi\sqrt{mrR}}\left[\left(1 - \frac{m}{2}\right)K(m) - E(m)\right] \tag{C.1}$$

$$I_2(q) = \frac{q\sqrt{m}}{2\pi(rR)^{3/2}}\left[\frac{1 - \frac{m}{2}}{1 - m}E(m) - K(m)\right] \tag{C.2}$$

$$I_3(q) = -\frac{q\sqrt{m}K(m)}{2\pi R\sqrt{rR}} + \left(U(r - R) - U(R - r)\right)\frac{\Lambda_0(\beta|m)}{2R} + \frac{1}{R}U(R - r) \tag{C.3}$$

$$I_4(q) = \frac{m^{3/2}(R^2 - r^2 - q^2)E(m)}{8\pi(rR)^{3/2}R(1 - m)} + \frac{\sqrt{m}K(m)}{2\pi R\sqrt{rR}} \tag{C.4}$$

Where U in Eq. C.3 is the unit step function. $U(x = 0) = 0.5$, $U(x > 0) = 1$ and $U(x < 0) = 0$. The factor q vary depending on what is in the parenthesis of the Geertsma integrals in Eq.2.23 and Eq.2.24. Λ_0 is defined by Eq.C.5.

$$\Lambda_0(\beta|m) = \frac{2}{\pi}\left[E(m)F(\beta|1 - m) + K(m)E(\beta|1 - m) - K(m)F(\beta|1 - m)\right] \tag{C.5}$$

$$m = \frac{4Rr}{q^2 + (r + R)^2} \tag{C.6}$$

$$\sin\beta = \frac{q}{\sqrt{q^2 + (R - r)^2}} \tag{C.7}$$

$$F(\beta|m) = \int_0^\beta \frac{1}{\sqrt{1 + m\sin^2\theta}}d\theta \tag{C.8}$$

Eq. C.8 is the incomplete elliptic integrals of first kind. The complete elliptic integral of first kind is given by Eq. C.9.

$$K(m) = F(\frac{\pi}{2}|m) \tag{C.9}$$

$$E(\beta|m) = \int_0^\beta \sqrt{1 + m\sin^2\theta}d\theta \tag{C.10}$$

Eq. C.10 is the incomplete elliptic integrals of second kind. The complete elliptic integral of second kind is given by Eq. C.11

$$E(m) = E(\frac{\pi}{2}|m) \tag{C.11}$$

C.2 Vertical Displacement at r=0

$$u_z = -\frac{C_m\alpha h\Delta p_f}{2}\Big(3 - 4\nu + \frac{D - z}{|D - Z|} - \frac{D - z}{\sqrt{R^2 + (D - z)^2}} - \frac{(D + z)(3 - 4\nu)}{\sqrt{R^2 + (D + z)^2}}$$
$$+ \frac{2R^2z}{(R^2 + (D + z)^2)^{3/2}}\Big) \tag{C.12}$$

The range for the elastic moduli in Table C.1 have been calculated using a study done by Havmøller (1996), where they investigated a large number of chalk samples to come up with a set of empirical equations for the geomechanical properties for the reservoir rock, see Chapter 2 in (Kvilhaug, 2016)

Parameters	Range	Average Values/ Values Used in Calculation
Porosity, ϕ [%]	[0.3-0.45]	0.375
Uniaxial Compaction Modulus, C_m [10^{-9}Pa^{-1}]	[1.193-4.808]	2.621
Young's Modulus, E [GPa]	[0.781-0.145]	(used to calculate ν)
Poisson's Ration, ν [Fraction]	[0.167-0.319]	0.257
Poroelasticity Coefficient, α [Fraction]		1
Reservoir Depth,D [m]		3000
Reservoir Radius, R [m]		4000
Reservoir Height, h [m]		200
Change in Pore Pressure, Δp [MPa]		-25
$\mathcal{R}$-factor		6
$K = \frac{C_m \alpha h \Delta p_f}{2}$		-6.55

Table C.1: Values used to calculate the resulting displacement with the Geertsma equations

Appendix D

Geophysics

D.1 Relative Time Shifts

Time shift ΔT capture the combined effect of change in thickness ΔZ and velocity ΔV_p within a given layer.

$$T = \frac{2Z}{V_p} \tag{D.1}$$

Change in TWT in a repeated survey is given by

$$\Delta T = \frac{\partial T}{\partial Z}\Delta Z + \frac{\partial T}{\partial V_p}\Delta V_p \tag{D.2}$$

Using $\frac{\partial T}{\partial Z} = \frac{2}{V_p}$ and $\frac{\partial T}{\partial V_p} = -\frac{2Z}{V_p^2}$

$$\Delta T = \frac{2}{V_p}\Delta Z - \frac{2Z}{V_p^2}\Delta V_p \tag{D.3}$$

$$\Delta T = \frac{2}{V_p}\Delta Z\frac{Z}{Z} - \frac{2Z}{V_p}\frac{\Delta V_p}{V_p} \tag{D.4}$$

$$\frac{\Delta T}{T} = \frac{\frac{2Z}{V_p}}{T}\frac{\Delta Z}{Z} - \frac{\frac{2Z}{V_p}}{T}\frac{\Delta V_p}{V_p} \tag{D.5}$$

$$\frac{\Delta T}{T} = \frac{\Delta Z}{Z} - \frac{\Delta V_p}{V_p} \tag{D.6}$$

Assuming $\frac{\Delta Z}{Z} << 1$ and $\frac{\Delta V_p}{V_p} << 1$